FATIGUE MODELING OF U720 – *A MULTI-SCALE APPROACH IN UNDERSTANDING GRAIN BOUNDARY EFFECTS ON CRACK INITIATION*

BY

MICHAEL D. SANGID

DISSERTATION

Submitted in partial fulfillment of the requirements
for the degree of Doctor of Philosophy in Mechanical Engineering
in the Graduate College of the
University of Illinois at Urbana-Champaign, 2010

Doctoral Committee:

Professor Huseyin Sehitoglu, Chair and Director of Research
Professor Armand J. Beaudoin
Professor Duane D. Johnson
Professor Darrell F. Socie
Professor Petros Sofronis

Abstract

Excessive scatter is observed in the fatigue response of a nickel-based superalloy, Udimet 720. This scatter can be partly attributed to the variability in the microstructure of this material. Hence, there is great interest in linking the microstructure to fatigue properties using a multi-scale approach that focuses on integrating the results of atomic simulations to the continuum level in the form of a micro-mechanical model. Thus, to capture the physics at the grain boundary (GB) interface, it is necessary to investigate this problem at a smaller scale. Molecular Dynamics (MD) simulations are used to obtain the energy barriers for slip nucleation and transmission across various GB characters, which are used to service our fatigue model.

In this study, we construct a model for prediction of fatigue crack initiation based on the material's microstructure. Our approach is to model the energy of a persistent slip band (PSB) structure and use its stability with respect to dislocation motion as our failure criterion for crack initiation. The components that contribute to the energy of the PSB are identified, namely, the stress field resulting from the applied external forces, dislocation pile-ups, and work-hardening of the material is calculated at the continuum scale. Further, energies for dislocations creating slip in the matrix/precipitates, interacting with the GBs, and nucleating/agglomerating within the PSB are computed via MD. The predicted fatigue life is driven by the microstructure such as grain orientations, widely distributed grain sizes, precipitates, PSB-GB interactions, as well as the effect of neighboring grains. The results predict that cracks initiate near twin boundaries from PSBs spanning a single large grain with a favorable orientation or multiple grains connected by low-angle GBs. Additionally, by varying the neighboring grains, we can account for scatter in the fatigue life. The uniqueness of our approach is that it avoids the large number

of parameters prevalent in previous fatigue models and provides deterministic results. Excellent agreement is shown between the model predictions and experimental data.

Acknowledgements

I would like to express my appreciation to my advisor Professor Huseyin Sehitoglu for his guidance, advice, and support. His eagerness in research and brute-force, results-oriented approach has helped me to produce results that are worthy of international recognition. Professor Sehitoglu piqued my interest about atomic simulations, energy balances, and persistent slip bands and allowed me to run with it. Over the course of the last three years, I have spent more time communicating with him then anyone else. In particular, during one instance, his kind words helped me personally through a tough time, and for that, I will always be grateful. Also, I would like to thank Professor Hans J. Maier of the University of Paderborn for his collaboration in this project, specifically for his TEM/EBSD analysis and our discussions on persistent slip bands.

Next, I would like to acknowledge the financial support provided by Rolls-Royce Corporation. I would specifically like to thank David U. Furrer and Jeffrey D. Stillinger for their technical assistance and encouragement throughout the course of this research; this work would not be possible without their efforts. I would also like to extend my gratitude towards Michael G. Glavicic, Mary Lee Gambone, Robert Goetz, and Don L. Vaccari.

I would like to express my sincere appreciation to my committee. Each of whom increased my knowledge in aspects of this project: Professor Armand J. Beaudoin for sharing his enthusiasm and knowledge of crystal plasticity, Professor Duane D. Johnson for his assistance in atomic simulations, Professor Darrell F. Socie for his insights into fatigue and applied problem solving, and Professor Petros Sofronis for his infectious passion of research and solid mechanics.

Also, Professor Harley T. Johnson was always willing to share his vast knowledge of nanoscale material's behavior.

I would like to thank Professor Placid Ferreira, Professor Charles L. Tucker, Professor Armand J. Beaudoin, and Jeffrey A. Sickmeier. These gentlemen each gave me great advice that led me down the path where I find myself today. The help provided by the entire MechSE staff was much appreciated. The countless favors that I received from the staff were always greatly appreciated and never taken for granted. Through their tireless efforts, day to day operations ran smoothly. I want to thank my HTML officemates. I want to especially thank Tawhid Ezaz for his invaluable and continuous help. He always went out of his way to lend a helping hand; it was very much appreciated.

The authors would like to acknowledge Professor David Olmsted of Northeastern University for supplementing our MD study with his database of grain boundary energies, Dr. Stephen M. Foiles of Sandia National Laboratory for sharing his nickel EAM potential, and Dr. Steven Plimpton of Sandia National Laboratory for creating and helping with LAMMPs. In addition, I want to thank Professor Anthony D. Rollett of Carnegie Mellon University, Professor David L. McDowell of Georgia Technology University, and Professor Hael Mughrabi of University Erlangen-Nuernberg Germany, whom visited as seminar speakers and each allowed me to 'pick their brains' and provided valuable insights which aided in the current research.

Finally, I want to thank my mother and father, Susan and David, for their continuous warmth and encouragement throughout my education. Similarly, I would like to thank my sister and brother, Shari and Mark, for their many phone calls to take my mind off of work.

Table of Contents

Chapter 1. Introduction

1.1. Fatigue Lifing Overview

One measure of a component's worth is based on how long it will last in service. Fatigue is one of the primary failure mechanisms of engineering components. As most components are designed well enough to withstand initial loadings, but after repeated, subsequent cycles, elastic or elastic-plastic stresses can cause failures within the materials due to fatigue damage. Thus, there exists great interest in characterizing the fatigue life of a material, in order to prevent catastrophic failures.

Fatigue life of a component can be expressed as the sum of two segments of life: (a) the number of loading cycles required to initiate a crack and (b) the number of cycles it takes that crack to propagate to failure. In the aerospace industry, there are two schools of thought to predict the fatigue life of a part: safe life and damage tolerant design.

Damage tolerant design assumes that cracks are initially present in all components inherently as a result of fabrication. Thus, the structure is able to retain its integrity in the presence of damage. This methodology focuses on controlling the cracks as they propagate through the material, thus managing the fatigue life of the component. Therefore, fracture mechanics play an important role in this design process as steady state crack growth allows for safe operation of the component until damage can be detected or repaired. This methodology is primarily used for military defense purposes, due to the inherent risk of aircraft damage. Also, as a result of impromptu maneuvering, it is nearly impossible to predict the loading cycle during any given flight, thus increasing the uncertainty in predicting the fatigue life. Perhaps in the next generation of fighter jets, the aircraft will be equipped with onboard diagnostic systems. These

systems will use micro-sensors on critical components to measure the loading cycles, which will feed into a rain-flow analysis to calculate the accumulated damage on the part. Thus providing warning to the pilot and maintenance staff in the case of excessive damage.

On the other hand, safe life design measures the life of a part until a crack initiates, which is the primary methodology in commercial aircrafts, specifically recommended by the Federal Aviation Administration (FAA). In the simplest form of this design methodology, fatigue tests are run on the material, and the scatter (standard deviation, σ) is calculated. The -3σ minimum from the average fatigue response of the material is used to design the component. The component is then tested assuming the worst case scenario at the -3σ minimum strength of the material, in order to clear a much lower operating stress that the component experiences during service. Thus a redundant safety factor is built into the design methodology of the component. But as a consequence, the components have low life, heavy weights, and high costs. Therefore, the safe life design is acceptable in certain applications but has limitations in others. This begs the question, is there a better way to predict crack initiation.

1.2. Problem Description

In this thesis, the primary research emphasis is predicting the fatigue crack initiation of microstructurally complex and 'misbehaving' materials. For instance, the safe life methodology breaks down in materials in which excessive fatigue scatter is observed. Thus new methods are required to predict the crack initiation and fatigue life of these components. For example, Figure 1.1 shows a material's strain-life fatigue curve in which, at a given value of strain, the material exhibits three orders of magnitude of scatter. This is a worst case scenario, but it has been observed in certain aerospace components. Thus, when applying the safe life design

methodology to this material, the results indicate that the material can only hold trivial loads or the material will only last a few cycles before failure. These results are unacceptable and non-realistic of the material behavior.

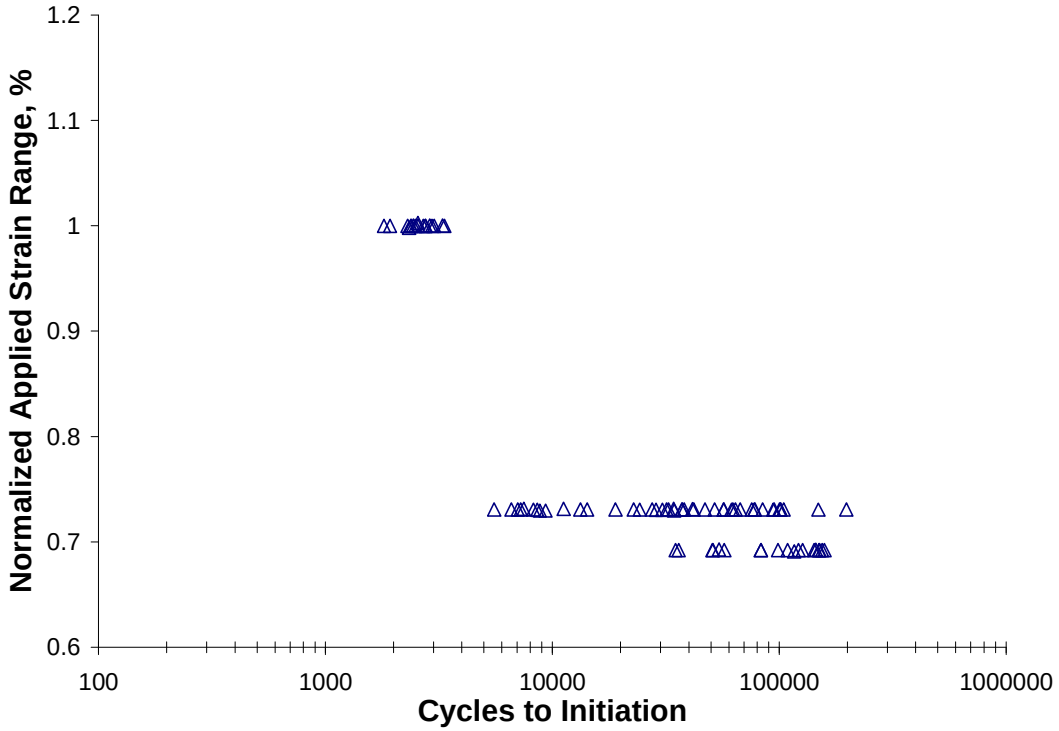

Figure 1.1. Strain-life plot displaying excessive scatter, which occurs in certain aerospace materials. Please note the applied strain ranges are shown as normalized values.

The next step, in the engineering analysis, is to view the material's microstructure. As seen in Figure 1.2, the microstructure is non-uniform and shows marked banding (unusually striated). We believe the variability in the microstructure leads to the excessive fatigue scatter. In this nickel-based superalloy, Udimet 720 (U720), gamma-prime (γ') particles are responsible for the material's characteristically high-strength at extremely high temperature. During heat treatment, these particles precipitate out of solution; afterwards the grains grow and are pinned by the γ' particles. Thus, in areas of dense γ', the grains are fine and evenly spaced. On the other hand, in denuded areas of γ', the grains are coarse, as shown in Figure 1.3. Hence, the

microstructure has areas of fine grains adjacent to coarse grains. Further, many of the grains are mis-orientated.

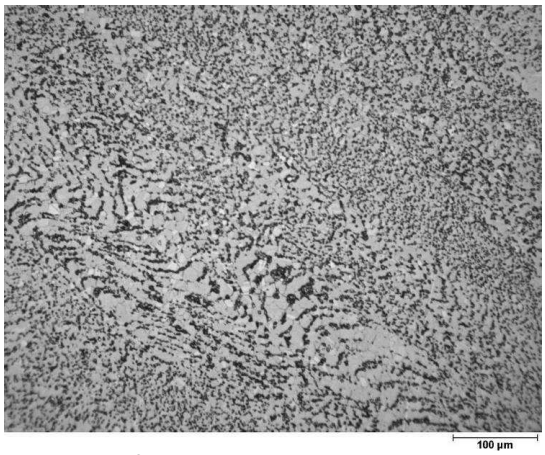

Figure 1.2. Optical view of the microstructure of a nickel-based superalloy, U720. In the figure, striated regions of γ' can be viewed (black particles), which restrict grain growth resulting in areas of fine and coarse grains adjacent to one another.

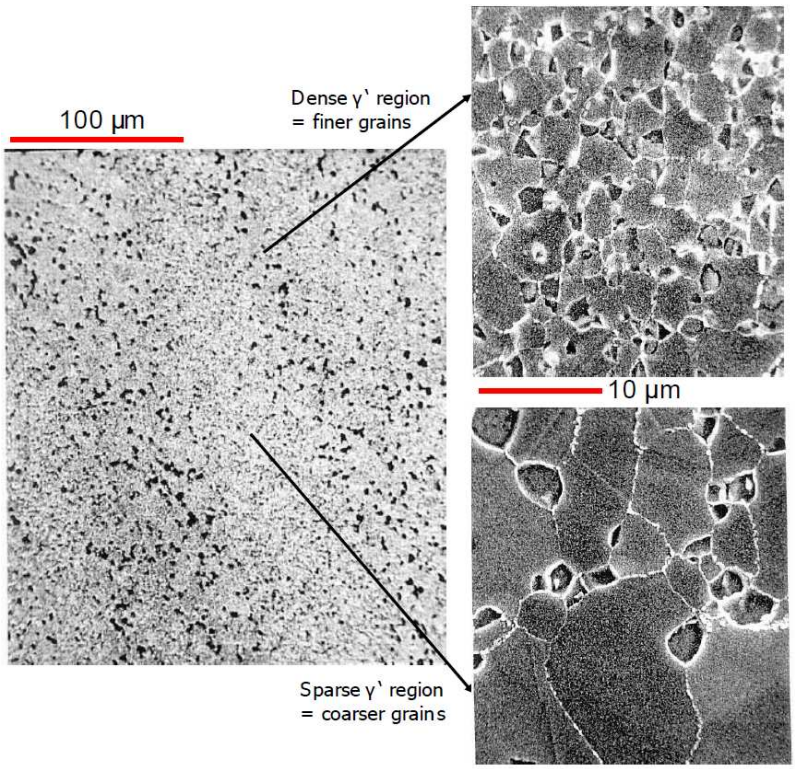

Figure 1.3. Microstructure of U720, displaying bands of γ' precipitates (left). These precipitates determine the grain size. In areas of densely populated γ', the grain size is fine, while in areas denuded of γ', the grain size is coarse.

The observed fatigue scatter can be partly attributed to differences in billet suppliers, heats/lots within a given supplier, forging vendors, or processing conditions. For the time being, we want to focus on variability in the microstructure and explain fatigue scatter based on the microstructure of the material. Hence, in the project, we attempt to model fatigue scatter based primarily on the microstructure, i.e. distributions of grain sizes, grain orientations, grain boundaries (GBs), and γ' precipitates. Namely, there exists a wide distribution of grain sizes and orientations, such that small grains are adjacent to large grains in this material. Hence, the fatigue response is significantly harder to predict than uniform coarse or fine grain material. This solidifies the need for a fundamental understanding of how GBs affect the fatigue behavior of the material. In order to do so, we must first rationalize the failure mechanisms observed within this material.

As shown in Figure 1.1, many low cycle fatigue (characterized by plastic deformation of the specimen during each loading cycle) were carried out on U720. The data exhibited unusual scatter, which prompted more testing and only increased the value of fatigue scatter. The fracture surfaces of these problematic specimens were analyzed using an SEM to locate the mechanism for crack initiation, as shown in Figure 1.4a. Two mechanisms were observed – inclusions (Figure 1.4b) and facets (Figure 1.4c). A correlation could not be established between failure mechanism and life, in other words one mechanism did not produce a lower fatigue life than the other. Typically, the inclusions were near the specimen's surface and composed of Ti-carbide in a $M_{23}C_6$ structure. It is believed that on a component, shot peening negates the risk of failure via inclusions by imparting a compressive residual stress which impedes crack initiation near the surface. In addition, suppliers have an increasing control of the material's cleanliness over the years, which results in less detrimental inclusions. Due to these factors, crack initiation

from inclusions is not of primary concern in this study. On the other hand, fatigue scatter due to crack initiation from a facet is still an unexplored subject from a mechanics of microstructure perspective. It is known that considerable plasticity is involved in creating these facets, which form near grain boundaries. Although the conditions which are more likely to initiate cracks and form facets are not properly defined, hence it is our goal to do so in this study.

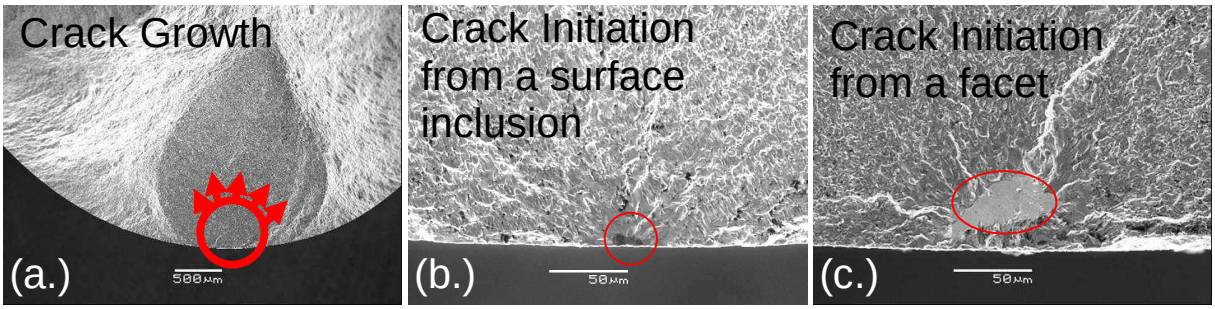

Figure 1.4. (a.) Fracture surface of a failed fatigue specimen. (b.) Crack initiation from a surface connected Ti-carbide inclusion. (c.) Crack initiation from a transgranular facet, although considerable plasticity is involved in forming this feature.

The following provides a framework for characterizing the nucleation of cracks in Udimet 720, a nickel-based superalloy, during cyclic loading. This alloy experiences an unusually wide range of fatigue scatter. It is believed that this scatter is attributed to the variability of the materials microstructure. The following study lays a groundwork, in which one can gain further understanding of the role of grain boundaries on fatigue. The purpose of this study is to determine the following:

- Can we determine a criterion for crack initiation in U720?
- How do mis-oriented grains affect the fatigue properties?
- How does grain size distribution and adjacent small/large grains within a polycrystalline material affect fatigue life?
- Can we account for fatigue scatter?

1.3. Modeling Approaches

There are many tools and modeling approaches one can take for such a problem; we discuss three broad strategies – continuum fatigue modeling, crystal plasticity, and atomistic/dislocation modeling. Historical fatigue modeling relies on regression of experimental data. This involves many expensive, time-consuming tests. In the case of excessive scatter, typically more tests are run to characterize the scatter. For this type of modeling, the material is treated as a continuous solid. Hence the microstructure is not considered.

Crystal plasticity is another powerful tool for determining plastic deformations based on the microstructure. Since this modeling is at the grain level, it is able to take into account grain orientations to determine stress-strain behavior and predict texture evolution. In a classical sense, crystal plasticity cannot account for grain size perturbations or the kinetics of GBs. Further, crystal plasticity is too computationally intensive to account for cyclic loading. Additionally, it cannot handle minimum energy dislocation structures, which are unique to the fatigue process. Crystal plasticity is at its best for predicting large strain monotonic loading behavior. It was not designed to account for the necessary back-stress or slip irrversibilities associated with cyclic loading. Moreover, many fitting constants are required to handle complex microstructures.

Atomistic and dislocation dynamics simulations model the mechanical response of atoms/dislocations due to interaction forces with other atoms/dislocations. This type of modeling is at too small of scale. For instance, there is a problem applying a simulation on the order of 10^{-7} m to a component on the order of 10^{1} m. To rectify this problem, the simulations are growing in system size and run-time resulting in increasing computational intensity. The

result typically cannot be used for quantifiable predictive purposes, due to inherent simulation problems such as unrealistically high strain rates and stresses.

The standard tools that one typically applies to these problems cannot address the complexities of the microstructure. A model which utilizes continuum mechanics cannot differentiate between fine and coarse grains and crystal plasticity is not suited to predict the fatigue response of a material. For these reasons, we have pursued an approach that would better be described as a physically-based mechanistic model. In this model, atomic simulations are used to gain insights of the mechanical behavior of GBs. Utilizing the comprehensive knowledge of the unique dislocation structures associated with fatigue and an experimental characterization of the grain size and orientation distribution, we can examine each of these length scales, as shown in Figure 1.5. This bottom-up technique offers a nice compliment to the current methodology, which experimentally examines fatigue samples from turbine discs and optically views the microstructure of each specimen, if necessary.

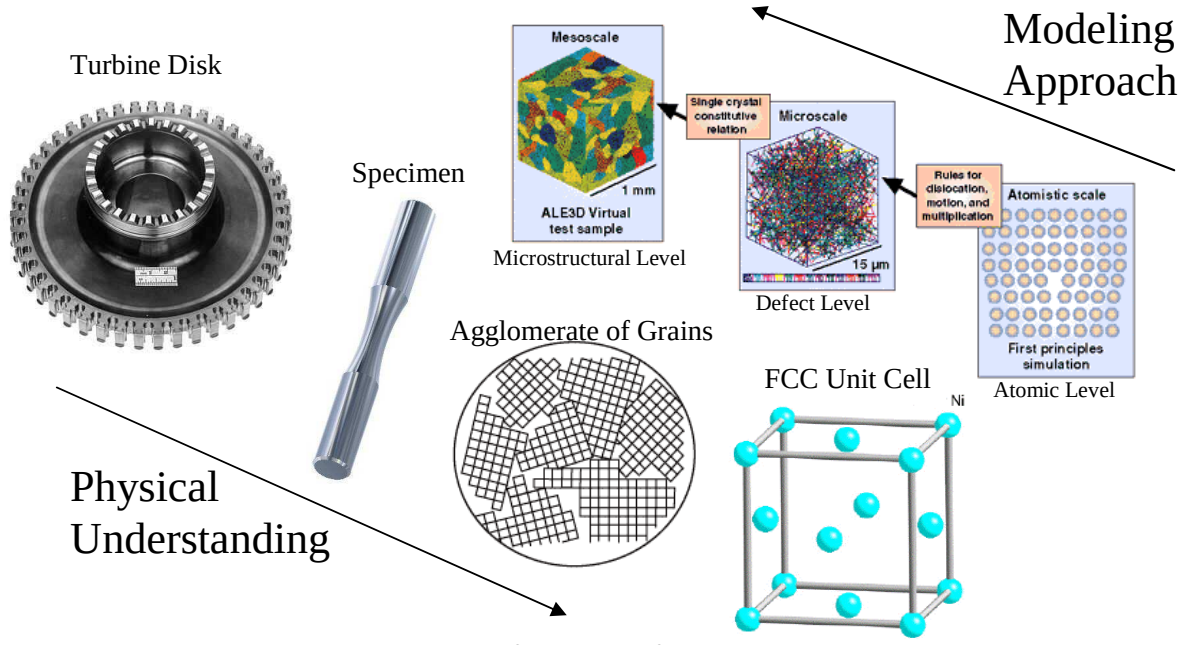

Figure 1.5. Modeling approach used in the formulation of our micro-mechanical model compared to the experimental analysis and the methodology behind our physical understanding of the material behavior.

Our modeling strategy focuses on favorable aspects of each of the aforementioned approach: crystal plasticity (accounts for grain orientation in polycrystals), an energy balance (physics-based, inherently account for microstructure), and atomistic simulations (insights into the response of GBs and precipitates). Hence, a multi-scale approach is utilized to account for the microstructure of the material, which can explain differences between fine/coarse grains, their corresponding lattice orientations, and grain boundary types. The resulting energy barriers for each GB are determined through atomistic simulations. This information is inserted into a model to create a physical fatigue simulation for crack initiation based upon an energy balance, as shown in Figure 1.6.

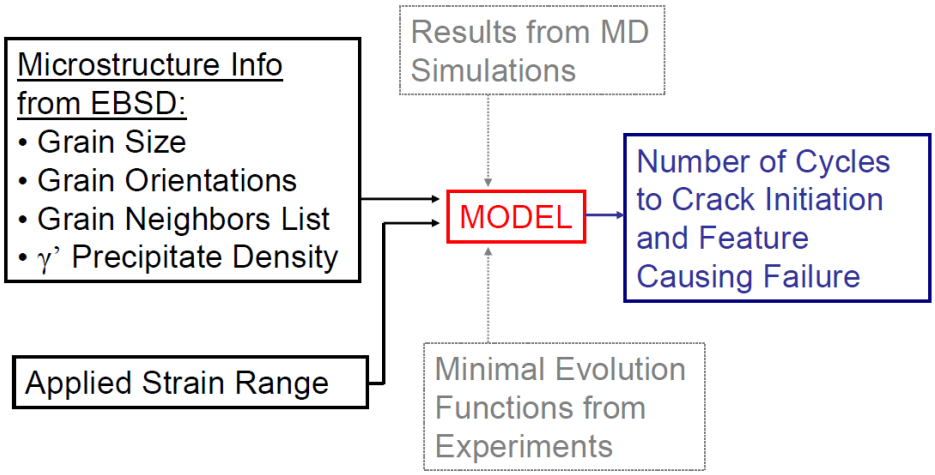

Figure 1.6. Modeling hierarchy used in this study. The inputs are the microstructure of the material and applied strain. The model relies on internal databases consisting of atomistic simulations and minimal experimentally determined functions. The result of the model is a prediction of number of cycles to crack initiation and the weakest link within the microstructure.

1.4. Research Contribution

In this research, the main contributions are threefold. Employ molecular dynamics to study the mechanical behavior of grain boundaries, but more importantly obtain quantifiable values for their role as a strengthening mechanism. This is accomplished by measuring the energy barriers to dislocation penetration through a GB and also dislocation nucleation from a

GB, in a technique that is unique to this study. Secondly, we establish a physically-based fatigue model that incorporates the microstructure and the unique nature of fatigue dislocation structures, i.e. persistent slip bands (PSBs). The goal of this model is to predict crack initiation from the weakest link of the materials microstructure (grain size, grain orientation, GB character (CSL Σ value), and γ' distribution). In doing so, we determine the effect of GBs on fatigue and clarify the role of twins in fatigue crack initiation. Finally, we quantify fatigue scatter in a deterministic approach based on the microstructure of the material. Most scatter models rely on many fitting constants and probabilistics. We simply show that we can accurately account for scatter in fatigue life by varying the neighboring grains within a microstructure.

1.5. Thesis Outline

This thesis is partitioned into nine chapters. For easy navigation through this body of work, each chapter is summarized below.

Chapter 1 examines the philosophy of fatigue lifing. A need is determined to mechanistically link the microstructure of a material to its fatigue properties. Modeling approaches are briefly discussed.

Chapter 2 presents a review of the current literature pertinent to this study. GBs are introduced as a mechanism to strengthen solids by impedance of dislocation motion. From this analysis, characterization of GBs, their corresponding energy barriers, and their effect on fatigue life are reviewed. Since the main emphasis of this project is predicting fatigue life, we investigate strain localization which is a precursor to crack initiation in the form of experimental studies and modeling of persistent slip bands.

Chapter 3 includes the experimental characterization of the material of interest, U720. This includes fatigue testing, EBSD measurements, and TEM analysis, which presents a foundation for our modeling efforts.

Chapter 4 presents characterization of the grain boundaries. Hence, the EBSD measurements of U720 are examined according to a CSL framework. Once this information is known, the energy of each GB is determined by atomistic simulations, in order to create a spatial map of the GB energy of the material

Chapter 5 presents a detailed analysis of the energy barriers for slip nucleation from and transmission through each GB. These quantities are calculated through atomic simulations.

Chapter 6 introduces the framework of our physically-based fatigue model for prediction of crack initiation. We focus on an energy balance of a PSB with respect to plastic deformation and define crack initiation based on the stability of the PSB. This model relies on contributions from the continuum and atomistic scales (Chapter 5), as well as the microstructure of the material (Chapter 4).

Chapter 7 discusses extending the fatigue model to predict cycles to crack initiation for polycrystals. The life is forecasted for EBSD scans of real specimens and compared to experimental data. Through this analysis, we are able to establish conclusions regarding the role of GBs on fatigue properties.

Chapter 8 establishes a Monte Carlo algorithm for predicting fatigue scatter based on the microstructure of the material. From the measured EBSD scans, we produce distributions of the microstructural variables, which are used to randomly populate the microstructure of a simulated specimen. The fatigue life is predicted of each simulated specimen to produce the fatigue scatter associated for this material.

Chapter 9 summarizes the goals and the important results of our research. We presented a physically-based fatigue model, which can accurately predict fatigue scatter based on the microstructure of the material. In doing so, we tried to address and unify many outstanding questions within the fatigue community. These conclusions are followed by a list of suggestions recommended for future research.

Chapter 2. Literature Review

In this chapter, we present a literature review of the effects of grain boundaries (GBs) on fatigue. In order to do so, we must first characterize GBs to understand their associated energy barriers to slip. Afterwards, we perform a detailed review of fatigue, specifically experimental studies and modeling of persistent slip bands (PSBs) as the mechanism for crack initiation in single and poly- crystals. This allows us to gain a deeper understanding of PSB-GB interactions and the role of twin boundaries (TBs) on crack initiation. Finally, we review modeling of fatigue scatter.

2.1. GBs as a Strengthening Mechanism

It is well established that GBs have a significant effect on mechanical behavior [1]. GBs offer a strengthening mechanism, since GBs impede dislocation motion resulting in pile-ups at the GB. As a result, finer grains are analogous to a stronger material due to a greater number of GBs per volume. Historically, three explanations of the GB strengthening mechanism were published. Hall and Petch stated that smaller grains lead to more dislocation pile-ups resulting in stress concentration that activates dislocation sources in neighboring grains [2, 3]. Ashby's dislocation interaction model contended, for a given deformation, there exists a discrete number of dislocations. As the grain size decreases, the dislocation density increases and the mean free path of the dislocations decreases, resulting in work-hardening within the grain [4]. Li and Chou argued that GBs can act as sources for dislocations thus further contributing to hardening behavior [5].

As a result, finer grain materials exhibit greater yield [1-3], fracture [1, 6, 7], and fatigue [8-14] strength than coarse grain material. These grain size relations are based on a homogeneous microstructure, although in real materials, there exists a grain size distribution. Hence, one needs to analyze a distribution of grain sizes to understand their effect on engineering materials. In one such study, using a self consistent, elastic-viscoplastic model, Berbenni has shown that the yield strength decreases with increasing deviation from a nominal grain size [15]. In this study, we analyze grain boundaries from a wide distribution of grain sizes and investigate their potential role as a strengthening mechanism.

2.1.1. Characterizing GBs

To gain a deeper understanding of the role of GBs, their structure must be characterized. A grain boundary involves two adjacent grains connected by an interface, as shown in Figure 2.1a. By including the nature of the grain boundary, one can model GBs as lattice rotations of type: twist (axis of rotation is parallel to the normal of the GB, Figure 2.1b), tilt (axis of rotation is perpendicular to the GB normal, Figure 2.1c), or mixed. It should be expected that a certain number of the atoms in each lattice have coincidental locations from one grain to the next. This is known as a coincidental site lattice, CSL. Further, special grain boundaries come as a consequence of the CSL, by taking the reciprocal of the fraction of coincidental sites; one can obtain the CSL Σ value. Figure 2.2 shows the atomic configuration of a grain boundary, in this case, a twin, where the lattices are tilted 109.47° about the <110> axis. Layer 0 represents the GB, where the atoms are mirrored about this twin plane. The stacking sequence moving away from the GB is C (red), B (silver), A (blue) in both grains. By looking normal to the GB, we see the top grain and bottom grain (Figure 2.2, right) both display the same A, C, B stacking,

although the B and C atoms have inverted locations. Hence, now one out of the three atoms are in coincidental sites across the GB, since only the A atoms align from one grain to the next. By taking the reciprocal of the number of coincidental site atoms, we obtain the CSL Σ value, which in this case is denoted as a Σ3 GB (all twins are Σ3 GBs). Further special grain boundaries come as a consequence of the CSL. Figure 2.3 shows the same GB from a different perspective. We see a group of atoms (bottom) that are in perfect agreement with the supercell background, the (111) plane. By taking a 60° twist rotation about the (111) plane, the ordering of the atoms are deviated such that once again the red and silver atoms do not align with the background lattice, thus one out of three atoms are in coincidental lattice locations denoting the Σ3 GB.

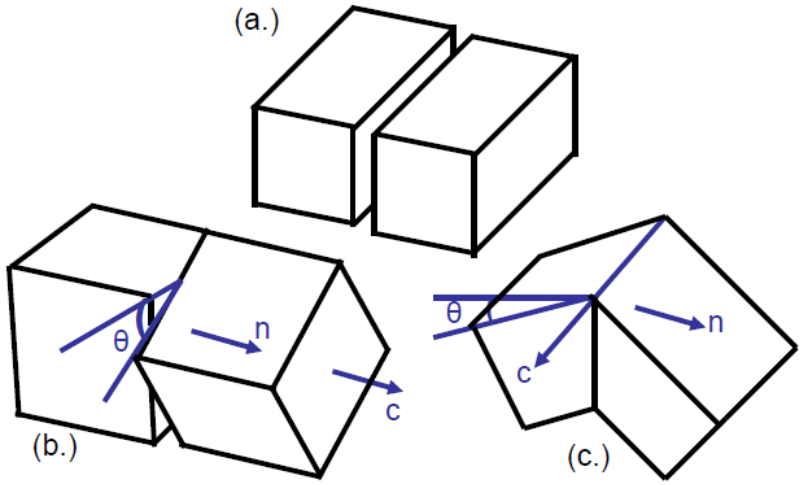

Figure 2.1. (a.) Schematic of two adjacent lattices, where the interface is known as a grain boundary (GB), (b.) A twist GB as the axis of rotation corresponds to the normal plane of the GB, (c.) A tilt GB as the axis of rotation is perpendicular to the GB normal.

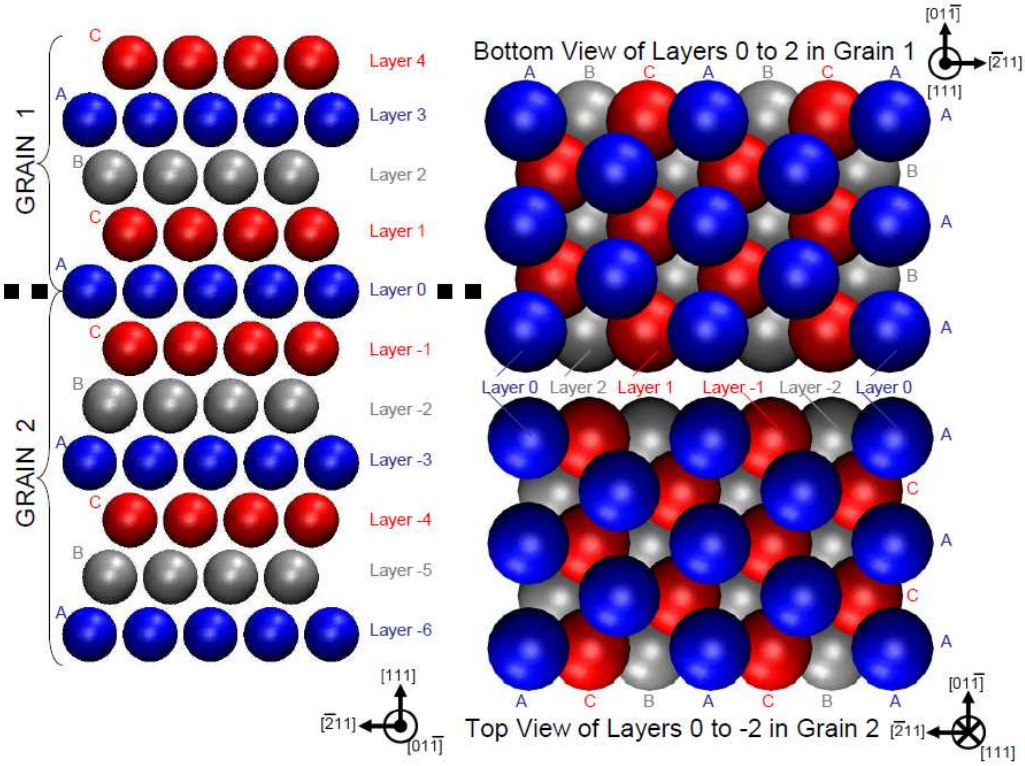

Figure 2.2. Schematic of a twin also known as a Σ3 GB, as the grains are tilted 109.47° about the <110> axis. The dashed line, layer 0, (left) represents the GB and the stacking sequence is mirrored about this plane. By looking along the (111) plane, we see grain 1 (top right) and grain 2 (bottom right) have the same stacking sequence, although the location of the red and silver atoms are misplaced. Hence, one out of every three atoms are in coincidence from one grain to the next, thus denoting the Σ3 GB in the coincidental site lattice (CSL).

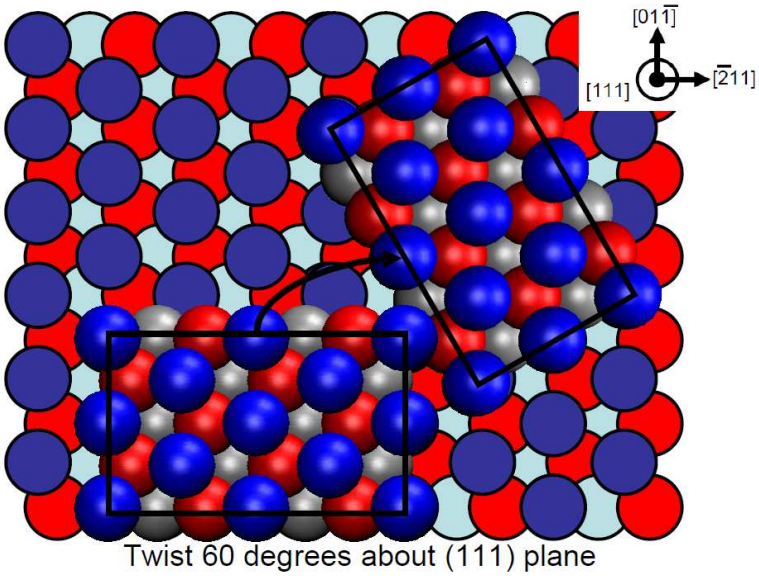

Figure 2.3. Schematic of a 60° twist about the <111> axis representing a (twin) Σ3 GB. By looking at each lattice relative to the supercell background, we can see that the (bottom left) lattice is in perfect agreement but after undergoing the rotation (top right), the blue atoms correspond to the background meanwhile the red and silver atoms are interchanged.

In other words, the CSL value is calculated by taking the ratio of the total number of atoms at the interface to those atoms that are in coincidental sites from each lattice, as shown in Figure 2.4. In each schematic, grains are differentiated by solid circle exteriors and shaded interiors with the colors designating the stacking sequence about their respective planes for an FCC material. Figure 2.4a displays a coherent twin boundary also known as a Σ3 GB, in which 3 out of 9 atoms match the spatial location and stacking sequence (similar colors). Similarly, schematics for the Σ5 (2 out of 10 atoms) and Σ7 (1 out of 7 atoms) GBs are shown in Figures 2.4b and 2.4c, respectively.

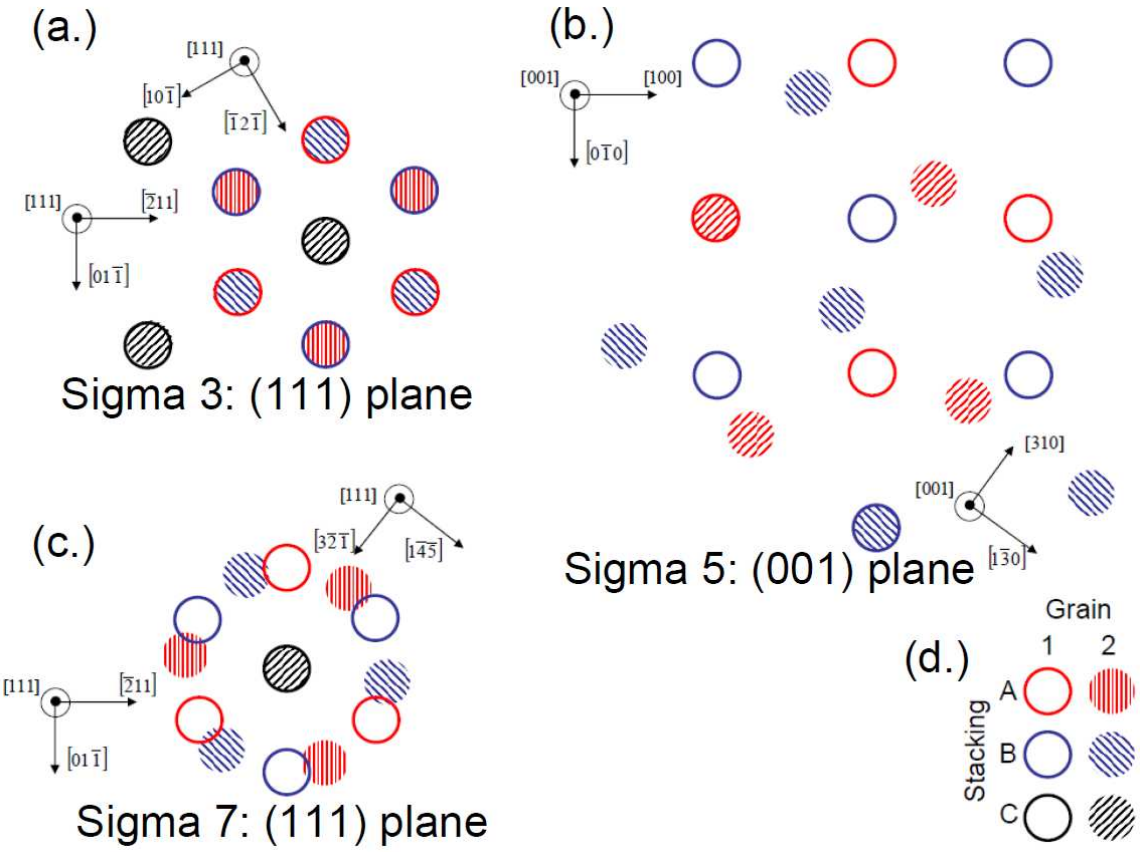

Figure 2.4. Schematic of CSL GBs – (a.) Σ3 GB, coherent twin boundary (3 out of 9 atoms are in coincidence), (b.) Σ5 GB (2 out of 10 atoms are in coincidence), and (c.) Σ7 GB (1 out of 7 atoms are in coincidence). (d.) In each schematic, grain 1 is represented with solid circle exteriors, grain 2 is represented with shaded interiors, and the stacking sequence is indicated by the various colors (ABC stacking (red, blue, black) for the (111) planes as shown in (a.) and (c.) and AB stacking (red, blue) for the (001) plane as shown in (b.). When the symbols spatially align with similar colors, the atoms are in coincidental lattice positions as indicated by for (a.), & for (b.), and for (c.).

In 1949, Kronberg and Wilson [16] were the first to point out the importance of the CSL to mechanical properties. They observed coincidence patterns in the boundary planes, which in the present CSL theory corresponds to Σ7 and Σ13 GBs. Kronberg and Wilson noted the significance of low Σ values for nucleation and growth during secondary recrystallization of copper as they found less segregation existing in these low Σ boundaries. More recently, experimental studies have shown that CSL boundaries of high CSL density / low Σ value do not crack during fatigue of Ni [17], stress corrosion of a nickel-based superalloy [18], and cavitation of Cu [19]. This is partly attributed to the low Σ value GBs containing a lower distribution of fatigue detrimental intergranular oxides [20]. GBs with an angle less than 15° are referred to as low-angle grain boundaries (LAGBs) or Σ1 GBs. These GB have been shown to offer less resistance to dislocation motion, less plastic strain incompatibility, and as a result do not exhibit intergranular fatigue cracking [21]. Read and Shockley modeled LAGBs as a series of dislocations with an associated energy [22]. Li calculated the stress field associated with LAGBs as a series of full [23] and partial [24] dislocations, and amended this calculation for high-angle GBs (HAGBs) [25], although a significant achievement, the latter model could not capture the complexities of the CSL.

For high-angle GBs, Brandon created a criterion, which allowed each GB to have a discrete deviation from a special Σ GB that is proportional to $\Sigma^{-1/2}$ [26]. This has been experimentally confirmed as intergranular fatigue cracking was non-existent for GBs within 3° of a Σ3 coherent twin; the ratio of failure by this mechanism increased for deviations from 3°-5° and dominated for GBs with deviations greater than 9° [27]. Modifications to the Brandon condition have been proposed by Palumbo and Aust [28], as they modified the exponent, -5/6, to impose a more restrictive upper bound deviation from a CSL and Schuh [29], whose deviation

limit rule requires the angular deviation of one boundary at a triple junction is at most equal to the sum of the other two deviation angles. However, the Brandon condition is still the most widely accepted expression to calculate deviations from a CSL Σ value, and is utilized to characterize what GB can still be denoted as a 'special' boundary.

To leverage the desirable properties of these special CSL GBs, the field of grain boundary engineering emerged. Watanabe was the first to coin the idea of engineering GBs specifically to increase the strength and ductility properties of polycrystals [30] and to control intergranular fracture [31]. Aust, Erb, and Palumbo expounded the idea of GB engineering to include geometric, energetic, and crystallographic constraints to show that a microstructure composed entirely of low Σ GBs is attainable [32]. External or hydrostatic pressure on the GBs has a significant impact on the GB character, and Gottstein addressed this issue as it effects GB free volume, segregation, and junction drag [33].

As the importance of the CSL became more widely recognized, the mathematics of GBs were developed to handle their configuration [34-41]. In 1964, Brandon et al. developed the CSL theory to relate two grains by particular misorientations about specific axes and tabulated these relationships [34]. This inspection method was generalized [35], which enabled 22 CSL values to be categorized up to Σ31 [36]. CSLs were later calculated using matrix theory, which is readily adaptable to computer calculations [37]. One of the most influential CSL papers were produced by Grimmer, Bollmann, and Warrington in 1974 [38], which explained how to obtain a Σ value from a pair of lattices from the rotation matrix, $\boldsymbol{\Delta g}$. The CSL Σ value is found as the least common denominator for each scalar value in $\boldsymbol{\Delta g}$, which they used to tabulate up to Σ49. Since the rotation, $\boldsymbol{\Delta g}$, is not unique, Grimmer described a definition of the disorientation (similar meaning to what we refer to as misorientation) [39], whereas (1) all the components in

the tensor $\boldsymbol{\Delta g}$ must be rational values and (2) there must exist a least common multiple, Σ, that makes $\Sigma \cdot \boldsymbol{\Delta g}$ and $\Sigma \cdot \det(\boldsymbol{\Delta g}) \cdot \boldsymbol{\Delta g}^{-1}$ integral matrices [40]. This theory was generalized to establish a function for determining CSL Σ values [41]. The mathematics necessary to distinguish CSL GBs from these studies are used extensively in this investigation.

A further level of understanding GBs is obtained by identifying the dislocation arrangement that composes the GB. Sutton and Vitek showed that the atomistic view of the GB can be constructed as a linear combination of dislocations known as the structural unit model (SUM) [42-45]. Each structural unit is associated with a preferred boundary for a given misorientation axis. From this relationship, they deduced that there is a link between the dislocation arrangement at the GB, series of structural units, and GB energy [46, 47]. This model has not been widely adopted due to the difficulty in determining the structural units for a given GB, especially for GBs that contain mixed character (3D), high misorientations, or disorientated structures.

The CSL field is tremendously aided by electron back scattering diffraction (EBSD) techniques, which allows an investigator to determine the orientation of each grain in an aggregate. There has been a great deal of work developing EBSD techniques and applying them to CSL configurations, including standard practices [48, 49]. The most influential study on the usefulness of CSL structures in polycrystals has been performed by Randle, in which she found that the Σ value of the CSL is a necessary but not sufficient criterion for 'special' properties [50], since each Σ value does not correspond to a unique type of GB. Hence it is necessary to analyze the GB plane and choose an appropriate criterion for deviations from this reference plane [51]. Randle also populated the statistics of various types of boundaries in polycrystals. From this analysis, she found that annealed copper and nickel are composed mostly of tilt GBs rotated

about the <110> axis [50]. If the interface plane in each grain is the same, the tilt boundary is symmetric, if not it is asymmetric. In annealed nickel, 21% of the GBs corresponded to $5 \leq \Sigma \leq 33$, while 46% of the GBs by number fraction were $\Sigma 3$ types [52], although the latter percentage is higher according to length fraction, i.e. the ratio of the $\Sigma 3$ boundary length to the total length of the GBs within the 2D EBSD scan [53]. As discussed, there are different types of $\Sigma 3$ GBs, and it has been shown that after extensive heat treatment, the entire population of the $\Sigma 3$ GBs are close to the lowest energy configuration in FCC materials, due to reorientation of the GB plane [54]. It has also been observed that GBs dissociate into $\Sigma 3^n$ ($\Sigma 1$, 3, 9, 81, 243) type to introduce lower energy segments of boundaries [50, 51]. These observations about the boundary plane as well as the statistics of GBs within a polycrystal are imperative to our characterization and understanding of GBs.

To fully characterize a grain boundary, one needs to resolve information across five degrees of freedom (DOF) – three to characterize the three unique rotations from one lattice to the next and two more to distinguish the plane separating the two grains. Standard EBSD techniques are two dimensional scans. Hence, to adequately characterize the GB, Rohrer et al. performed an EBSD scan and then serial sectioned a specimen by removing 7μm via polishing and repeated this process [55]. This procedure collected a 5 DOF GB description through reconstruction of the serial scans, although it is extremely labor intensive. This facilitated a new method to collect the same data based on the probability of line traces [56]. This stereological procedure analyzed the intersection between GB and the specimen surface plane. From the line trace, cubic symmetry properties, grain orientation, and lattice misorientation, a probability is determined for the additional DOFs (i.e. the GB plane). The results of the GB character from this method were similar to the serial sectioning data. This method views peaks within the

stereological circle corresponding to the dominant GB planes within the aggregate, but does not resolve the exact plane for a specific GB. From this 5 DOF analysis of GBs in Al and ceramics of low Σ type, the GB plane is most frequently oriented in a low index plane with low surface energy [57]. Further, they observed individual segments containing larger boundary areas had lower relative GB energies in Ni [58]. Using a more deterministic and less laborious method, Ghosh et al. implemented an automated focused-ion beam (FIB) technique to serial section the test specimen inside the same SEM apparatus as the EBSD. This allowed a full 3-D computer based reconstruction of the microstructure by aligning and interpolating between the triple points within the microstructure [59, 60].

To investigate the grain boundary at a smaller length scale, many researchers have employed atomic simulations. The CSL configuration is well-suited for this investigation, since it can be fully described mathematically, is periodic, and, as a result, easily computationally implemented. In a series of papers, Wolf investigated the [100], [111], [110], [113], and [112] tilt and twist GBs as well as asymmetric twist GBs [61-64]. From this work, Rittner and Seidman clearly described a technique for generating the GB energies for symmetrical tilts along the [110] axis and associated this energy with the atomic structure of the GBs and the resulting dislocations arrangement [65]. The most thorough atomistic analysis of GBs to date was performed by Olmsted, Foiles, and Holm, which created a database for the energies and mobilities of symmetrical and asymmetrical (388 total) boundaries in Ni and Al [66, 67]. Out of all the GBs surveyed, the coherent twin (of type Σ3) had the lowest energy and mobility. Many of the procedures used in these studies aid the current work.

It has been established that both the grain size and grain boundary character plays an important role in the mechanical behavior of the material. Although in the literature, these two

microstructural aspects have been treated separately. In this study, we correlate the role of GB character, specifically GB energy to the grain size. Further, we analyze the GB character for a range of material processes and deformations from billet to forging to experiments (tensile, compression, and fatigue), in order to characterize the evolution of the GB and as a consequence its effect on mechanical behavior.

2.1.2. Energy Barriers Associated with GBs

At the atomic level, the physics of the energy barriers produced by GBs is still an unresolved issue, including the individual strengthening benefit of various types of GBs. These energy barriers are essential to plastic deformation and have tremendous implications especially for failure mechanisms such as fatigue, fracture, and creep.

The role that individual interfaces play on the mechanical behavior of a material is a very hard phenomenon to observe. To simplify this analysis, many experiments have been conducted on a bicrystal, which allows researchers to study deformation and incompatibilities across a single grain boundary [1, 68]. In 1957, the pioneering study of bicrystal deformation was conducted by Livingston and Chalmers [69]. Their research created a criterion for slip across a grain boundary that was governed by purely the geometry of the system. The geometrical criteria presented by Livingston and Chalmers, presented a sound picture of slip across a grain boundary, although it had shortcomings, which prompted the work of Shen, Wagoner and Clark in 1986 [70]. Their study established a modified geometrical condition and required that the resolved shear stress be maximized. In 1989, Lee, Robertson, and Birnbaum proposed that a third criterion was necessary for the prediction of slip transfer mechanisms across grain boundaries [71]. The first two conditions (geometrical and resolved shear stress conditions)

agreed with Shen, Wagoner, and Clark, although a third condition required the residual dislocation in the grain boundary be minimized. The strain transfer across a grain boundary can also be viewed as a function of dislocation density though the use of EBSD measurements of the elastic strain gradient [72]. The result of which shows there is a large discrepancy in the geometrically necessary dislocation density across grain boundaries due to dislocation pile-up. The work above outlines strain incompatibility at the grain boundary, although this does not address the stress or energy barriers that dislocations must overcome to penetrate the grain boundary.

In order for a dislocation to penetrate a GB, there must exist sufficient applied stress to drive the pile-up of incident dislocations past the stress field of the GB [73]. The slip-GB interaction is governed by the degree to which the system can relax local stress concentration, which govern the possible cases as outlined by Sutton and Balluffi [74]: i) direct transmission, ii) direct transmission including residual dislocations in the GB, iii) indirect transmission including residual dislocations in the GB where the incident and outgoing slip systems do not intersect, and iv) no transmission – the dislocation is incorporated in the GB.

The activation energy in a material represents a barrier to slip and plastic flow. This parameter is dependent on the stress, temperature, and strain rate as discussed by Seeger, which leads to a spectrum of activation energies [75, 76] due to the microstructural features and the statistical distribution of local strength. To better represent this concept, the activation energy has been separated into thermal and athermal components. Conrad has shown the importance of the long-range internal stress field on the athermal component of flow stress and outlined a methodology to calculate this parameter from experiments [77]. Meanwhile Kocks proposed that the thermal component of the activation energy can be back-calculated in a

phenomenological method presented by fitting a functional form of the Arrhenius law to experimental data of single or polycrystalline material [78-80]. This methodology has served the materials community well, although it does not shed light into the activation energy for individual grain boundaries within an aggregate, as is the focus of this study; to do so, we must characterize individual grain boundary types.

As previously mentioned in Section 2.1.1, atomistic simulations have been used to calculate the relaxed GB energy of CSL configurations. By adding forces to the atomic simulations, the mechanical behavior of grain boundaries can also be analyzed using molecular dynamics (MD) [81]. Spearot et al. investigated the stress-strain behavior of <100> and <110> symmetric tilt GBs and correlated the plastic behavior with the dislocation structures at the interface [82]. Many of the procedures used in these studies aid the current work.

Building on these investigations, many researchers have used MD to model dislocation nucleation from grain boundaries of nanocrystalline material as means of explaining the transition in deformation mechanisms at smaller length scales [83-88]. In the present work, we are concerned with the deformation of grain boundaries in larger scales, representing bulk material. Recently, there has been series of papers by McDowell et al. that investigate nucleation of dislocations from a GB in a bicrystal in <100> and <110> symmetric tilt GB [82, 89], although the stresses necessary to nucleate the dislocation from these pristine GBs were calculated correctly for ideal cases, they are much too high. This analysis was extended to include asymmetric Σ3 GBs [90] and GBs containing dissocatiated structures [91] and ledges [92], hence the nucleation stress decreases from these initial defects, although it is still higher than that measured in nature; the excessive value of the simulation stress is indicative of MD.

Hence, in order to contribute quantifiable modeling of the dislocation nucleation from a GB, one must not use stress as a state variable.

Over the years, there have been a handful of researchers that have simulated dislocation – GB interactions. Bulatov et al. used (2D and 3D) MD to view dislocation-GB interactions which resulted in slip transmission, absorption, and blockage depending on the local GB structure [93-95]. Interestingly, transmission did not always occur on the plane with the highest resolved shear stress. They attempted to consolidate these simulations with a line tension model to predict the interaction, although this model did not take into account the GB structure. Similarly, DeWald and Curtin created a 2D coupled atomistic/discrete-dislocation (CADD) model for dislocation interaction with symmetric tilt Σ3, Σ9, and Σ11 boundaries [96, 97]. The multi-scale modeling resulted in a build up of stress on the leading dislocation within the pile-up and an overall lower required external stress to penetrate the GB. Similarly, their simulation showed both Schmid and non-Schmid transmission. From the results, they proposed additional requirements to the Lee, Robertson, and Birnbaum criterion [71]: normal compressive stress on the boundary should be small, the resolved shear stress on the leading pile-up dislocation should be high, the GB resolved shear stress should be small, and the residual step or ledge height at the boundary should be minimized. In this study, we build on these simulations of slip-GB interactions, in order to model additional GB characters and link this information to GB strengthening mechanisms, namely through energy barriers to slip penetrating a GB.

Gumbsch et al. simulated a perfect screw or 60˚ mixed dislocations interactions with coherent twin boundary in FCC metals using molecular statics. Perfect screw dislocations transmitted through the boundary or dissociated into partials in the boundary plane [98]. Incident mixed dislocations dissociated into more complex reactions resulting in partials gliding

in the twin plane [99]. These studies were extended to model symmetric Σ3 and Σ9 tilt GBs in tungsten (BCC structure). In their study, dislocations absorbed into the GB led to stress concentrations and preferred sites for crack nucleation [100]. This process is strongly dependent on the GB structure, geometry of the slip systems in adjacent grains, and location (structural unit) of the interaction at the GB [101]. The simulations of dislocation-GB interactions have also been applied to explain the increased strength in metallic composites and nanopillars. Hoagland et al. used MD to study the strengthening effects of interfaces in multilayer FCC metallic composites (Cu with either Ni, Nb, or Ag) [102-106]. The incoherent interfaces were found to be a strong barrier to slip. This mechanism was attributed to the following sequence – attracting glide dislocations to the interface, absorbing the dislocation resulting in spreading of the core in the interface, and forcing nucleation in order to transfer slip to the adjacent grain. Sansoz viewed the effects of twins impeding slip penetration in nanopillars by the formation of Lomer-Cottrell locks, thus providing a substantial strengthening mechanism [107, 108]. The aforementioned slip-GB interaction simulations offer a qualitative understanding of the role of GBs in strengthening the material. Although these studies do not address the kinetics of slip in the vicinity of grain boundaries, hence in our MD analysis, the focus is on obtaining energy barriers of slip-GB interactions.

There have been a number of studies that have measured the activation energy of slip from MD simulations. Van Swygenhoven et al. simulated two nanocrystalline aggregates containing a larger distribution of 1.) low-angle GBs and 2.) high-angle GBs [109]. From this analysis, the activation energy was calculated from the Arrhenius plot as described by Kocks [78-80]. The simulation containing low-angle GBs exhibits higher activation energy for

deformation. Their work is significant, although this analysis is based on the distribution of GBs within the sample and does not focus on the activation energy of individual GBs.

In a material, the ductile to brittle transition has been modeled by Rice-Thomson [110] based on the criterion of dislocation emission from a crack tip. This model has provided a tremendous contribution to the field. Cheung, Argon, and Yip combined the output of an MD simulation to the Rice-Thomson model to obtain the activation energy for dislocation nucleation from a crack tip [111]. Similarly, Rice and Beltz calculated the activation energy from an MD simulation within the Peierls framework [112]. Extending this study, Warner and Curtin used their CADD method to measure dislocation nucleation from a crack tip using the Peierls concept [113]. Their findings showed that the activation energy is temperature dependent thus affecting the elastic constants and stacking fault energies. Further, upon nucleation of a partial dislocation, there is a competition between twinning and full dislocation emission. Each of these investigations offers significant contributions, although they do not take into account the role of GBs. Also, their methodology includes simulations coupled to continuum, in which many assumptions are made.

Recently, these simulations have been aided by the nudged elastic band (NEB) approach. The NEB method calculates a potential energy landscape along the reaction coordinate for a given load and calculates the potential energy based on the maximum energy along the minimum path. This methodology has been applied to calculate the activation energy of a dislocation nucleating from a crack tip [114, 115]. Similarly, the NEB method has been applied to obtain the activation energy for other types of slip deformation. Zhu et al. measured the activation energy and its strain rate dependence of nano-twinned material, which addresses its unusually high combination of strength and ductility [116]. Building on this study, Zhu et al. created a

closed form equation for the temperature and strain rate dependence of activation energy for dislocation nucleation from surfaces in a nano-wire/pillar [117]. Gao et al. used a combination of MD and the NEB to study interactions between screw dislocations and coherent twin boundaries (CTB) [118]. At large distances, there are repulsive forces between the screw dislocation and CTB, while at short distances, attractive forces led to absorption of the screw dislocation within the CTB.

In this study, we apply the theory of the activation energy to the problem of slip-GB interactions. In order to do so, we produce a new methodology for the energy barriers that dislocations must overcome to penetrate GBs. These energy barriers are shown to depend on the characteristic of the individual GB.

2.2. Fatigue

From experimental results, finer grain material generally experiences a longer fatigue life [8-14], since PSBs are prone to form in larger grains [119-121]. Although these studies were performed on materials with uniform grain size and cannot address the response of adjacent small/large grains as we account for in this model. Similarly, there have been a number of studies that examine the GB character in terms of the CSL theory [17-19]. Hence, it is important to account for the GB character as this contributes to the formation and stability of a PSB. As a consequence, the affect of individual CSL Σ values on the fatigue behavior of a material as well as grain size and orientation are addressed in this model.

2.2.1. PSBs in Single Crystals

During the fatigue process, defects multiply and accumulate within the material. This behavior results in an increase in the dislocation density [122-124], which form unique structures in an attempt to minimize the total energy of the system [125]. As a consequence, in many materials strain is localized in the form of slip bands, which are precursors for crack initiation, as first pointed out by Ewing & Humfrey [126], Seeger et al. [127], and Friedel [128]. Persistent slip bands were initially observed in single crystal FCC pure metals, specifically copper, although the concept has been generalized as a function of temperature, stacking fault energy, slip character, and applied strain amplitude (cycles to failure) [125, 129-131].

Due to slip irreversibilities, vacancies are generated creating a flux within the PSB resulting in surface intrusions and extrusions. Meanwhile, dislocations agglomerate into the walls of a PSB, which act as strong barriers to slip, resulting in a hardening response of the material. Both the hardening behavior and dislocation density are seen to saturate as the fatigue cycling continues [132-134]. Thus, PSBs represent significant localization of plastic deformation, slip, and dislocations, therefore hardened (PSB) regions are adjacent to the relatively soft matrix material. The interface between the PSB and matrix is a plane of discontinuity across which there are abrupt strain gradients, resulting in a preferred site for crack initiation [135-140].

Many of the physical insights into the mechanisms that form a persistent slip band were theorized by Mughrabi and Essmann in the late 1970s and 1980s, specifically on the generation and annihilation of point and line defects within a PSB [141]. Cyclic loading produces positive and negative edge dislocations, which attract each other, forming dislocation dipoles agglomerating in the walls of the PSB resulting in a nearly zero Burgers vector [142-145]. Only

edge dislocations are retained, because positive and negative screw dislocations annihilate [141, 146, 147], as shown in Figure 2.5a. Very narrow edge dislocations can annihilate, thus generating vacancies.

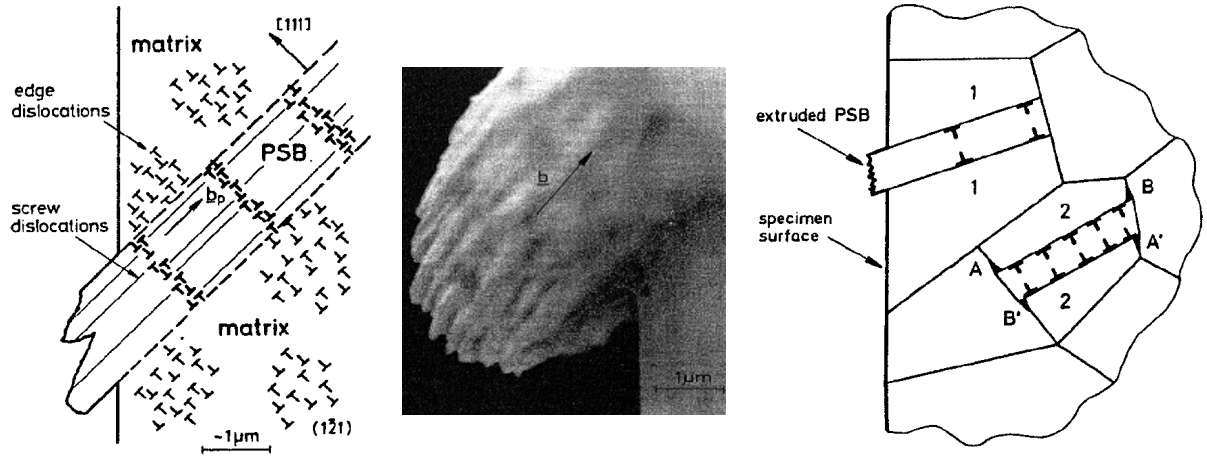

Figure 2.5. (a) Schematic of the dislocation structure within a PSB, (b) TEM micrograph of a series of extrusions resulting from a PSB, and (c) an extruded PSB in a polycrystal [148, 149].

Within the PSB, dislocation glide even at low temperatures and as aforementioned there is a flux of vacancies resulting in intrusions/extrusions at the surface (Figure 2.5b). During the surface roughening process, the average dislocation distance in the fatigued matrix approaches the annihilation distance for dislocations, which Essmann and Mughrabi calculated for edge and screw dislocations in copper [141]. The annihilation distance provides an upper limit for dislocation density and vacancy concentration in the walls of the PSB, whose values are much greater compared to the fatigued matrix domains [141, 150, 151].

Mughrabi and Essmann et al. created a model for extrusions and intrusions resulting from a PSB, focusing on randomly distributed irreversible slip processes, as a product of a dynamic equilibrium between dislocation multiplication and annihilation in a PSB [141]. The result of which leads to elongation of the PSB, extrusions/intrusions at the surface of the single crystal,

and an increase in surface roughness. In their model, they estimated the surface roughness, *Ra*, which displays a square root dependency on the number of loading cycles, *N*:

$$R_a = 2F\sqrt{Nb\gamma_{PSB}p_{PSB}h_p}\ , \tag{2.1}$$

where p_{PSB} is the ratio of irreversible strain to total strain, γ_{PSB} is the plastic strain amplitude in the PSB, h_p is the thickness of PSB, $\boldsymbol{b}$ is the Burgers vector, and F is a proportionality constant [148, 149]. Many parameters are used that cannot be simulated or measured prior to failure. Hence, only logical quantitative estimates can be given for the model's variables. This model is physically-based and well thought-out. Hence this model serves as an important starting point to us; by including energy barriers, stress fields, and an overall energy foundation, we establish a PSB model for crack initiation by integrating perspectives from the atomistic and continuum scales.

Many PSB models build on the insights and techniques of Essmann and Mughrabi for single crystals [129, 152-154], including Ortiz and Repetto who created a finite element model for the development of a PSB in an initially defect-free single crystal FCC material. The result leads to an outward flux of vacancies and the formation of surface roughness and stress concentration as a precursor to a sharp surface crack resulting in failure [154]. This model relies on fitting a constitutive model to the diffusion of vacancies in a single-crystal and delivers insightful results, but it cannot account for variability in a material's microstructure.

To truly understand PSBs, we must analyze fatigue dislocation arrangements. As previously mentioned, during cyclic loading, dislocations arrange themselves into preferred defect structures to minimize the total elastic strain energy of the system. In 1977, Kuhlmann-Wilsdorf and Laird discussed, in detail, the theory of low energy dislocation arrangements [155, 156]. Through a simple force balance of the stresses exerted by an edge dislocation on a Taylor

lattice, Neumann showed that several specific configurations result in stable structures, including ladder (series of walls, as seen within PSBs, Figure 2.5a) and vein (diamond multipole) configurations [157, 158]. This work represents the foundation for a field that has later been coined discrete dislocation dynamics modeling. From this approach, Fivel et al. used 3D dislocation dynamics under fatigue loading to simulate the associated surface topography and roughness profile resulting from a PSB [159-161], although the aim of this model was on surface characterization, we focus on predicting failure based on microstructural parameters in this study.

There have been a few attempts to develop a closed-form solution to the stress field developed by the dislocation arrangement of a PSB. Brown used the Airy's stress function to develop an expression for the stress field by the dislocations of a PSB [140, 162, 163]. Van der Giessen and Needleman developed a dislocation dynamics model to verify that the stress field from a series of planar edge dislocations can be modeled as a series of hyperbolic terms [164]. Brinckmann extended this model to account for two opposing series of edge dislocations, which provided a good approximation for the dislocation arrangement in a PSB and the resulting stress field [165]. These models represent the stress field of dislocations in a PSB from 2D dislocation dynamics; hence there is still a need for incorporation of the unique dislocation arrangements within PSBs into a polycrystalline fatigue model, which is addressed in our model.

2.2.2. PSBs in Polycrystalline Materials

To this point, we have only discussed PSB formation in single crystals, although dislocation walls and PSBs can form in the most favorably oriented grains within a polycrystalline material (Figure 2.5c) [120, 151, 166-168]. Blochwitz et al. studied PSB

interactions with GBs during fatigue of polycrystalline material. Their results showed that PSBs affect the local stress at the GB, further the process is influenced by the misorientation between grains [119, 169-171] or the presence of a twin [172]. Zhang et al. observed that PSBs are able to transmit through low-angle GBs, although high-angle GBs impede PSBs resulting in cracks initiating at the boundary and intergranular fracture [151, 173-179].

Lin and Ito developed a model for plastic shear strain accumulation from a PSB in a polycrystal [180]; however their shear stress field was non-equilibrating. Building on their concepts, in 1981, Mura and Tanaka created a powerful micro-mechanical model for crack initiation at a PSB in a polycrystalline material [181-183]. Their approach created an energy balance of the dislocation structure along the PSB in the most favorably oriented grain, as shown in Figure 2.6a. The PSB consists of two series of dislocations on opposing layers, which account for deformation as a result of forward and reverse loading. In order to incorporate slip irreversibility in the Mura and Tanaka model, it is postulated that the irreversibility of dislocation motion in the two adjoining layers arises from the different levels of back stress during slip in the forward direction on layer I and in the reversed direction of layer II.

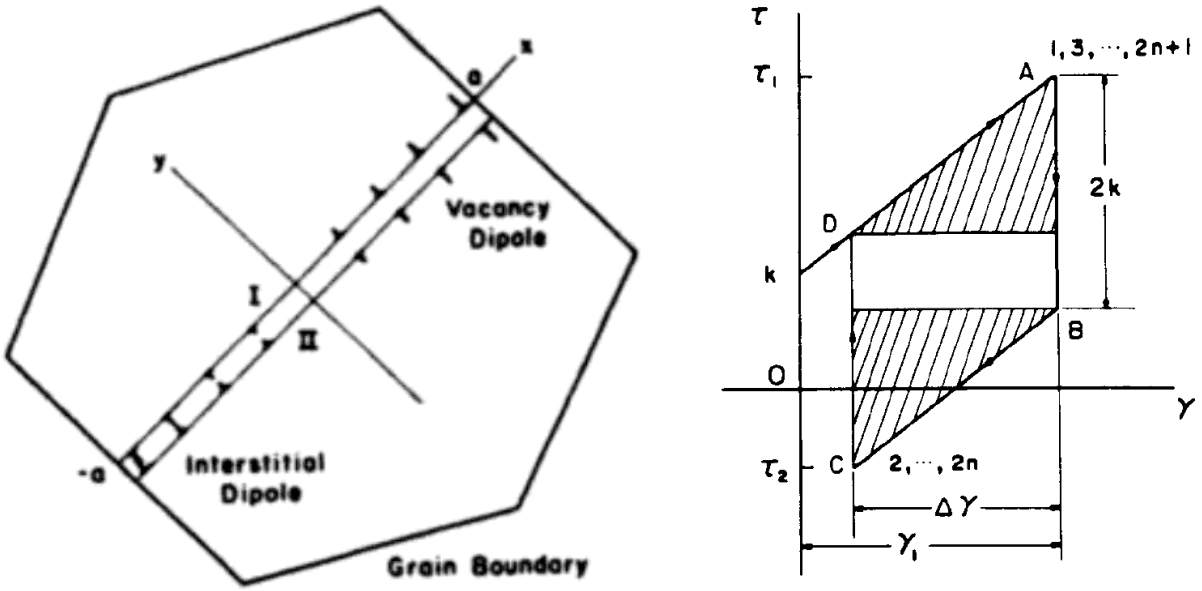

Figure 2.6. (a) Model of dislocations in a PSB of the most favorably oriented grain in a polycrystal. (b) Hysteresis loop, which accounts for the energy during fatigue loading, although a frictional stress must be overcame to move dislocations [181-183].

The change in energy, ΔU, from forward to reverse loading is given by:

$$\Delta U = \frac{1}{2}\Delta\gamma(\Delta\tau - 2k), \tag{2.2}$$

where $\Delta\tau$ is the alternating applied stress and k is the frictional stress of the matrix, which must be exceeded for dislocation motion (in this model it is assumed that $\Delta\tau > 2k$). The plastic strain, γ, is given by integrating the distribution of continuous dislocation within the PSB, D.

$$\gamma = \int_L \vec{b} D(x) x dx \tag{2.3}$$

Thus, the alternating plastic strain, $\Delta\gamma$, can be given as follows:

$$\Delta\gamma = \frac{(\Delta\tau - 2k)a^2\pi(1-\upsilon)}{\mu}, \tag{2.4}$$

where $2a$ is the grain size, υ is the Poisson ratio, μ is the shear modulus, and $\boldsymbol{b}$ is the Burgers vector of the material. The total energy of the PSB, U, is the sum of the energy on the two layers of opposing dislocations, which can be equated to the alternating energy, ΔU, during reverse

loading by the number of cycles, n. Failure is reached when the total energy of the PSB reaches the specific fracture energy of the material, W_s.

$$U = U_I + U_{II} = 2n_c \Delta U = 4aW_s \tag{2.5}$$

By rearranging this, the number of cycles to failure, n_c, can be written as:

$$n_c = \frac{4\pi(1-\upsilon)W_s a^3}{\mu \Delta \gamma^2}. \tag{2.6}$$

Substituting Equation 2.4 into 2.6 and rearranging, we can express this failure criterion into a Coffin-Manson type expression

$$\Delta\tau = 2k + 2\sqrt{\frac{\mu W_s}{\pi(1-\upsilon)n_c a}}. \tag{2.7}$$

Notice that the stress has an inverse square relationship with the grain size, a, hence this model is still reminiscent of the Hall-Petch model of grain size dependence on fatigue strength. This model was extended to account for notches, as dislocations pile-up in the presence of a notch, which acts as a stress concentrator.

Mura's and Tanaka's model was revisited in the 1990s, as the Gibbs free-energy evolution was calculated with increasing number of loading cycles. The change in the Gibbs free-energy, ΔG, is seen to increase, hit a maximum value, and sharply decrease during fatigue loading, as shown in Figure 2.7a [184, 185]. The change in the Gibbs free energy was used as their criterion for instability of dislocations within a PSB during fatigue and ultimately crack initiation. The free-energy considerations correctly predicted easier crack initiation in air as opposed to a vacuum, at higher temperatures, and closer to the material's surface. This model works well and is comparable to experiments by adding an additional variable for degree of irreversibility, f, as shown in Figure 2.7b [186].

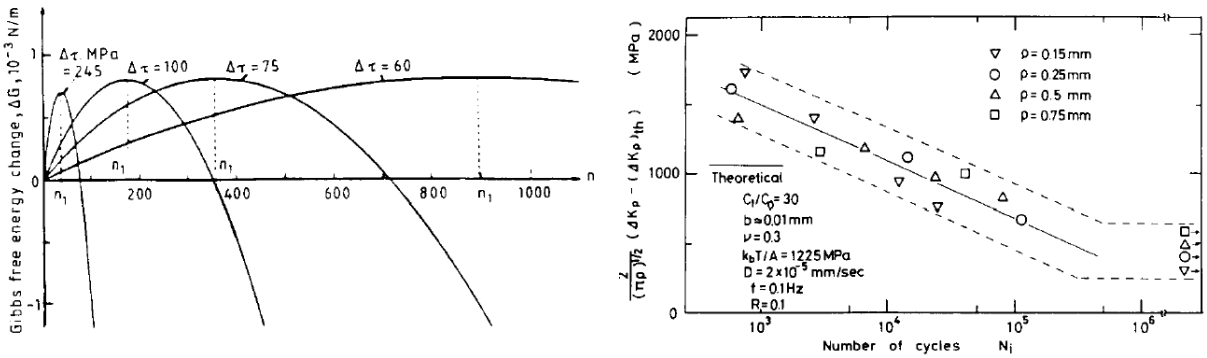

Figure 2.7. (a) Evolution of the change in free-energy with increasing loading cycles. (b) Mura and Tanaka model results in terms of range of apparent stress intensity factor and number of cycles to crack initiation compared with experimental results [186].

There are some concerns and limitations with this model. For instance, this model consists of a simple energy balance and does not take into account the complicated geometry and dislocation structure of a PSB and several energy terms need to be incorporated for a complete description of the PSB, including the energetics of the GBs. Nor does it account for the normal stress, which is critical in fatigue. One layer of dislocations does not effect the other during reverse loading, which is an over simplification. Also, there is an energy discrepancy, as shown in Figure 2.6b, as their model takes into account only the portion of the hysteresis loop above yielding; i.e. the energy does not account for the total area within the hysteresis loop. There is the idea that the frictional stress parameter, *k*, must be overcame for the dislocations to move.

Historically, the majority of the studies on PSBs have been on pure FCC materials, although PSBs have been observed in alloys [187, 188] and superalloys [189-193]. Typically, superalloys are strengthened by an ordered γ' precipitate. Petrenec et al. studied the dislocation arrangements in nickel-based superalloys (IN713 and IN792) at room and elevated temperatures [194-196]. They concluded that persistent slip bands were evident and contained a high density of dislocations, as shown in Figure 2.8. PSBs form as dislocations cut through the matrix and γ' precipitate in a planar slip manner at both temperatures and were the main source of crack

initiation [194-196]. Therefore, the PSB structure in precipitate-hardened superalloys (i.e. multiple parallel thin bands and a planar concentration of plastic strain from shearing the precipitates) is noticeably different compared to the ladder-like structures observed in single-phase materials.

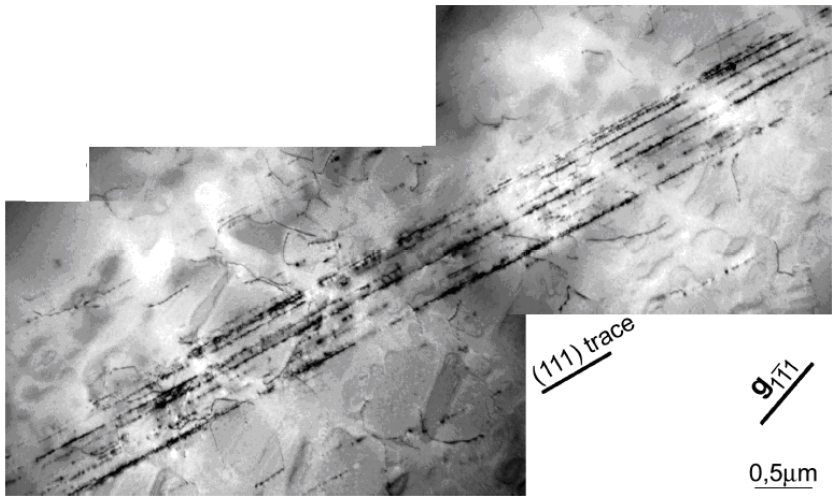

Figure 2.8. TEM micrograph of the dislocation arrangement within a PSB of IN792 [194-196].

As previously mentioned, PSB formation manifests in surface roughness by means of intrusions and extrusions. This phenomenon is also seen across the grain boundaries in the bulk of a polycrystalline material [151]. Recently, inclusions and extrusions have been measured and quantified using atomic force microscopy (AFM) [119, 197-199], which can be related to the irreversibility of slip/displacements in the material [200, 201]. Risbet et al. measured the evolution of extrusions on the surface of cyclically loaded Waspaloy, a nickel-based superalloy [202-204]. The height of a PSB is seen to be nearly zero until a threshold number of cycles is reached, increase rapidly, and nearly saturate. As expected, this behavior is highly dependent on the applied strain range.

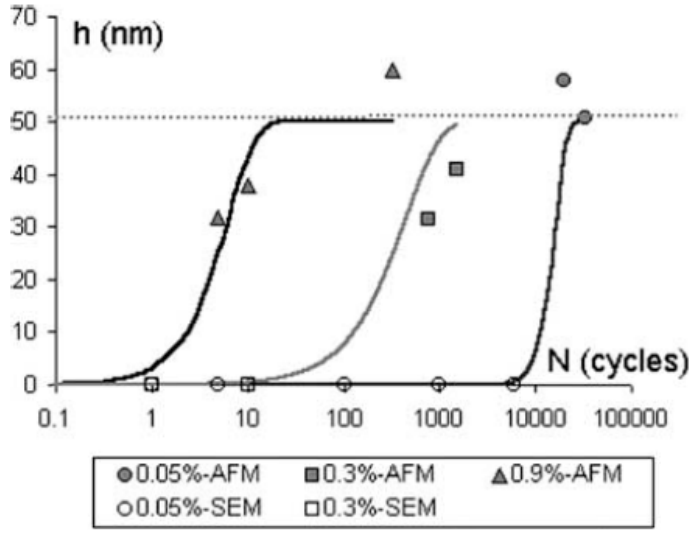

Figure 2.9. Average height of a PSB evolving with increasing number of cycles for various applied strains in Waspaloy [202-204].

In an extremely intensive experimental study, Huang et al. [205] used in-situ neutron diffraction to measure the dislocation density in monotonic and cyclically loaded Hastelloy C-22HS, a nickel-based superalloy. Figure 2.10 shows the dislocation density increases during cyclic loading and saturates, as a consequence the mean dislocation spacing decreases as PSBs are formed. The aforementioned work represents an extensive effort in capturing the slip behavior, dislocation density, wall spacing, and extrusion length evolution with number of cycles during fatigue of nickel-based superalloys; these quantitative values and trends are extremely valuable for use in this study.

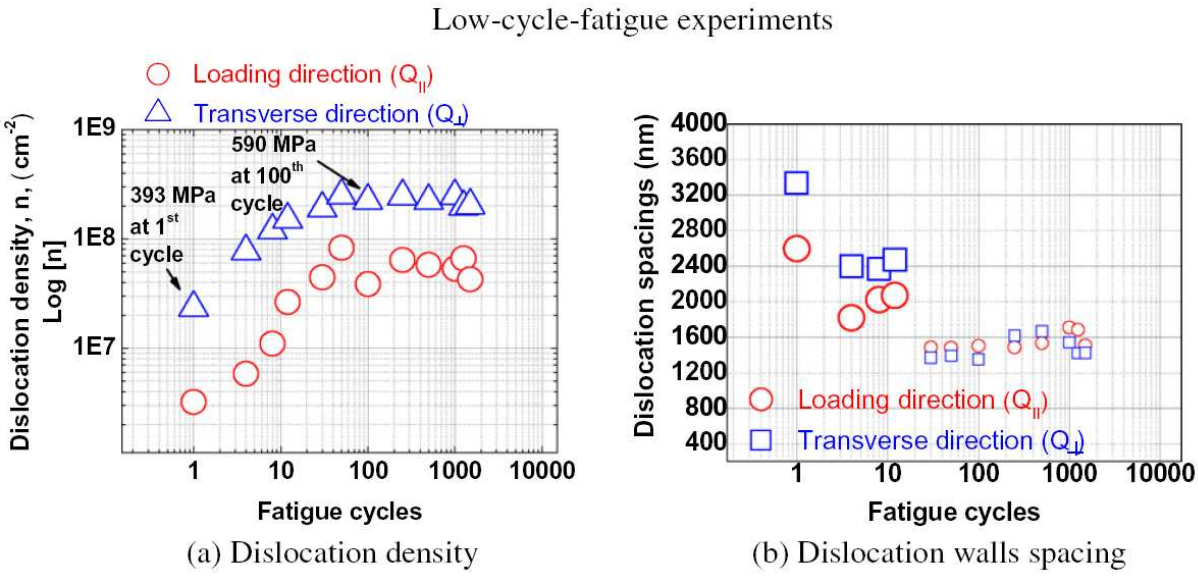

Figure 2.10. (a) Dislocation density and (b) dislocation wall spacing as a function of number of cycles in 1% strain fatigue loading of Hastelloy C-22HS [205].

Persistent slip bands have been examined in detail over the last 30 years, but a model capturing its complexities has yet to emerge. In this study, we formulate a model for predicting fatigue crack initiation in a wrought nickel-based superalloy, although this methodology could be used to characterize fatigue in a variety of metals and alloys. This material was chosen due to the complexities and wide-distributions of microstructural features, further validating our model. Hence, we establish a physically-based fatigue model that incorporates the microstructure (grain size, grain orientation, GB character, and γ' distribution) and the unique nature of fatigue dislocation structures, i.e. PSBs. The model encompasses continuum and atomistic contributions in a unified energy expression. In the subsequent sections each component contributing to the overall energy of the PSB section are identified and quantified. These components are the heart of our fatigue model, which establishes an energy balance for a PSB.

2.2.3. PSB-GB Interactions

Fatigue crack initiation in pure FCC metals is most commonly a result of persistent slip bands (PSBs) at mid-to-low strain amplitudes [141, 148, 149]. Initial studies of the PSB mechanisms focused on copper single crystals, although similar dislocation arrangements have been observed in polycrystalline material [120, 167, 168, 206]. In these materials, PSBs form in large grains with high Schmid factors [119, 170, 207].

Over the years, several models have emerged to explain PSB mechanisms in polycrystalline material and their role in crack initiation. The dislocation arrangements in polycrystals are similar to those in single crystals, except that the dislocations are impeded by the GB resulting in pile-up and stress concentration [148]. The resulting stress is relieved by formation of a static extrusion at the GB; expressions are formulated for the resulting slip and static extrusion height at the GB [151]. Over an increasing number of cycles, the stress concentration and extrusion height increases assisting in crack nucleation at the PSB-GB interface.

GBs have been described as impenetrable obstacles to PSBs that cause stress concentration resulting in cracking or PSB formation in adjacent grains [169]. Since that time, the misorientation and Schmid factor of adjacent grains have been recognized as important parameters in determining PSB-GB interaction and crack initiation [171]. Based on experimental observation by Zhang et al., PSBs can transmit through low-angle GBs (LAGBs), hence cracking does not occur in these boundaries [173, 178, 208]. LAGBs are defined as a misorientation between grains of less than 15˚, also referred to, in literature, as a Σ1 GB according to the coincidental site lattice (CSL) [16, 38] theory using the Brandon condition [26]. Interestingly, PSBs cannot transfer through general (random) high-angle GBs (HAGBs),

resulting in impedance of dislocation motion, dislocation pile-ups, stress concentration, and intergranular fracture [176]. Further, the mechanism of HAGB cracking is independent of the angle between the applied stress axis and the GB plane [177]. From this analysis, the PSB-GB interaction can result in dislocations behaving by one of the following scenarios: passing through, piling-up, or partially passing through (resulting in a residual dislocation within the GB) [175, 209]. For the latter case, the GB orientation and character plays an important role [210]. The GB character can be quantified by the CSL notation, as an outcome special CSL boundaries do not experience intergranular cracking [17, 211], especially the Σ3 boundaries also known as twins, which are discussed later in this section. These experimental observations are leveraged in our model to predict fatigue crack initiation via PSBs.

The stress necessary to cause cracking at a PSB-GB interface was first calculated by Essman, Gosele, and Mughrabi [148], in which the slip vector is directly related to the grain diameter. This analytical expression for stress was amended by Christ [212] and Liu et al. [213] to include the number of dislocations within the pile-up (from the Eshelby, Frank, Nabarro solution [214]) and the angle between the pile-up and GB (Stroh's equation [215]). Their analyses showed that coarser grains and high energy GBs were preferred sites for cracking, although their models over predicted the shear stress necessary for crack initiation. Based on the assumption that the PSB forms over a quarter of the grain diameter, the concept was extended to provide more accurate theoretical stresses [216]. The amount of slip that penetrates the GB was calculated, which reduces rapidly with increasing misorientation [217]. Each of these models provide a valuable contribution to the field, although they cannot predict failure, since most of the variables in their analysis do not evolve with increasing loading cycles, nor do they account for the effect of neighboring grains as is the focus in our model.

2.2.4. The Role of TBs in Fatigue

Experimentally, twin boundaries (TBs) have been observed as preferred sites for crack initiation [207, 218, 219], although there is still debate on the TB's fatigue response in FCC material. In other words, do TBs harden the material or degrade the fatigue life by acting as crack nucleation sites? Initially, in 1964, Bottner, McEvily, Liu observed the formation of fatigue cracks at TBs [220]. In many cases, the PSBs form parallel to the TB's normal, resulting in PSB-TB interaction. They note coherent TBs as low energy interfaces within the material, but as PSBs intersect the TBs, non-coherent ledges, steps, or static extrusions form on the TBs. The resulting steps are non-coherent, facilitators of secondary slip, dislocation sources, stress concentrators, and preferred crack initiation sites, as shown in Figures 2.11a-c. The same phenomenon was observed by Thompson [221]. He concluded larger grains and lower stacking fault energies (SFE) result in greater dislocation pile-ups (Figure 2.11d) and more secondary slip, respectively; as a consequence both factors result in more stress concentration and are more prone to cracking. In other words, TBs are inherently stronger against intergranular cracking in materials with high SFE, while in low SFE materials, TBs accommodate much of the plastic deformation leading to stress concentration and crack nucleation at the TB [222]. Interestingly, in nanocrystalline material, thinner twins (<1 μm) play an important role in strengthening the fatigue response of the material by affecting the type of PSB-TB interaction [223].

Many models are available to explain TBs as preferred sites for crack nucleation [171]. Kim and Laird argued that plastic incompatibilities caused by surface steps at the TB lead to irreversibilities (Figure 2.11e) and cracking [224]. Lim and Raj presented a dislocation model as shown in Figure 2.11f, in which they measured the residual or sessile dislocations at the

boundary and from this quantity coined a continuity factor dependent on the slip transfer [225]. Neumann created a traction model to calculate the local stress concentration at TBs promoting crack initiation at low plastic strain amplitudes (HCF), as shown in Figure 2.11g [226]. Peralta et al. modeled the elastic incompatibilities near a TB (Figure 2.11h); from this analysis, they calculated the stress concentration, which is a maximum value when the tensile axis is a <111> direction, i.e. the loading axis is parallel to the TB [227]. In this model, the TBs promote early primary slip and secondary slip. Peralta's elastic incompatibility results were reconstructed using the finite element method [228, 229]; the results are in agreement and show that coherent TBs have the highest elastic stress concentrations. Building on these concepts, Neumann's model was modified by Blochwitz and Tirschler to account for medium plastic strain amplitudes, thus representing an elastic-plastic solution (considering surface tractions caused by elastic anisotropy as well as the related slip processes), as shown in Figure 2.11i [172, 230]. Each of the aforementioned models demonstrates the role of TBs as preferred sites for fatigue crack initiation in polycrystalline material.

These experimental results and analytical models provide a solid foundation for our model, which overwhelmingly illustrate that cracks preferentially nucleate near TBs as a consequence of dislocation pile-up and stress concentration. This is illustrated through atomistic-based calculation of the energy barrier for slip-GB interaction in this study, in which TBs have the largest value. Also, in our analysis, we describe an approach to model the energy of a PSB structure and use its stability with respect to dislocation motion as our failure criterion for fatigue crack initiation. From this analysis, we are able to predict the fatigue life of polycrystalline specimens, which rely heavily on PSB-GB interactions. It is our purpose to rationalize the long standing observation of the role of TBs in fatigue by modeling at the atomic

and continuum scales, thus we provide a unified framework for clear understanding of TBs in fatigue.

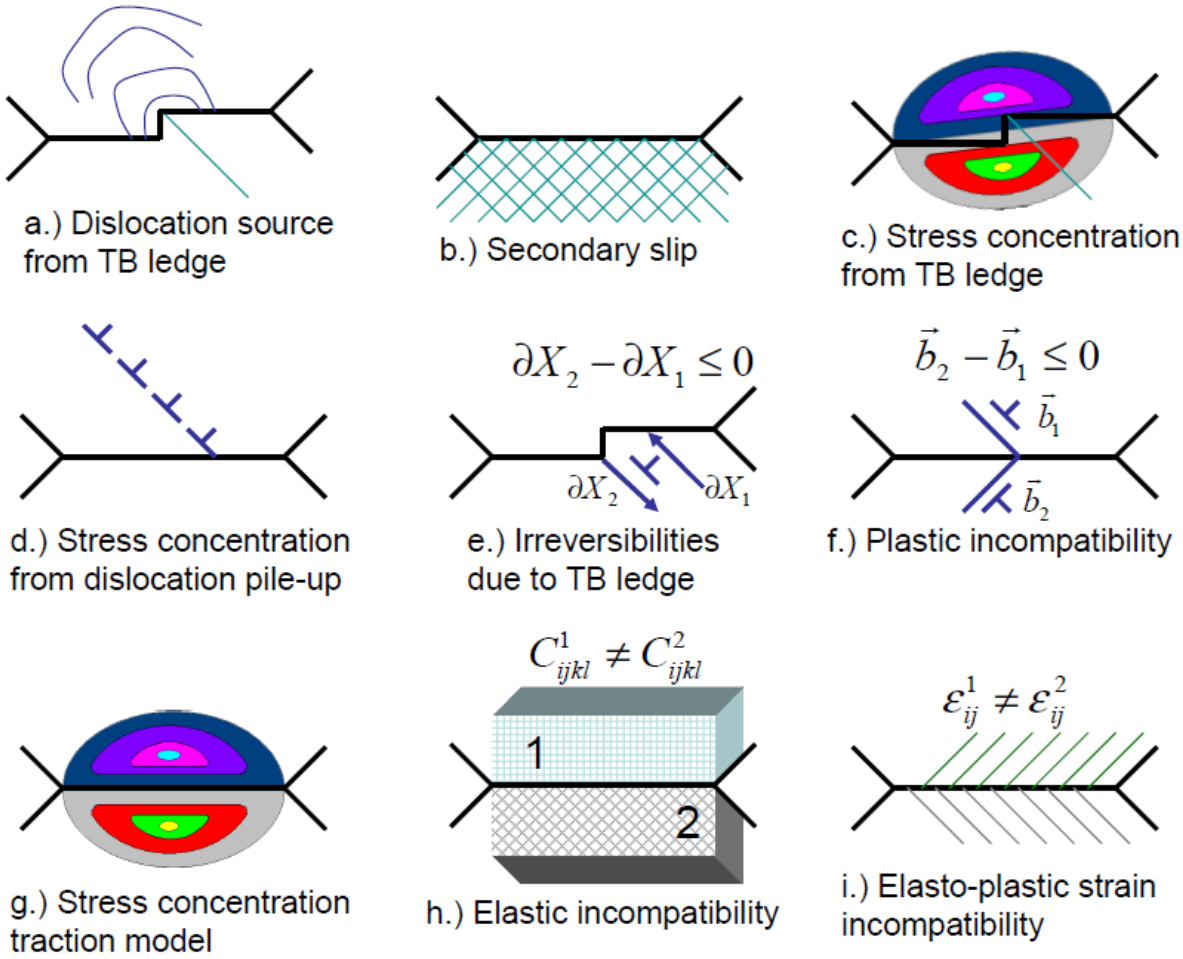

Figure 2.11. Theories describing crack initiation at twin boundaries (TBs). (a.) Ledges/steps at the TB are noncoherant and effective sources for dislocation nucleation [220]. (b.) Due to the stress concentration at the TB, secondary slip is activated [220]; which is more prevalent in low SFE materials [221]. (c.) Ledges/steps result in stress concentration [220]. (d.) Dislocations pile-up at the TBs resulting in stress concentration, which is more dominant in larger grains [221]. (e.) Ledges/steps at the TB results in irreversible slip [224]. (f.) Plastic incompatibility as a result of incoming and outgoing glissile dislocations interaction with the GB [225]. (g.) Stress concentration is due to traction at the surface and TBs [226]. (h.) Elastic incompatibility is highest at the TB [227]. (i.) Extension of (h.) to include plastic strain incompatibility [172, 230].

2.2.5. Modeling Fatigue Scatter

There exists inherent variability in every material property due to the following: inhomogeneity in the material at the microstructure level, differences between heats and vendors, allowable ranges in the chemical compositions, the response of various impurities, stochastic mechanical behavior, testing differences, et cetera. This material variability is even more pronounced when viewing the fatigue response of a material. In the high cycle regime (the material undergoes primarily elastic loading), the fatigue life is dominated by the initiation and growth of a single crack, thus deviation in the probability of failure is a function of applied stress/strain [231]. As opposed to the low cycle regime (loads are sufficient to yield the material during each cycle) where multiple cracks initiate and interact with one another, the fatigue scatter is a function of applied cycles. There have been many attempts made over the years to characterize the material variability through probabilistic models including statistical based and damage accumulation methods.

By use of statistical based methods, the log-normal fatigue and Weibull distributions are the most general and widely used model to fit fatigue scatter. For each applied stress or strain range, a distribution of failure is calculated [232]. Further, Socie argued that the standard empirically-based Coffin-Manson model should be generalized to account for the probabilistic response of the curve fit parameters [233] to capture the material variability in different life regimes. Using the response of a statistical model to simulate crack initiation, Provan and Ghonem account for variability in strength characteristics of a polycrystalline material to applied load, residual stresses, work hardening, and the accumulation of damage [234]; although this model does not account for variability in the microstructure such as grain size, orientation, or misorientation. It is known that the grain size has a first order affect on fatigue lives, although

there are no current models that predict its role especially when a wide distribution of sizes can be present in the microstructure.

A subset of these statistical models is defect-based models, for materials whose primary failure mechanism are voids, inclusions, or second phase particles. Thus, finding the probability of cracks initiating from inclusions within a material has received a substantial amount of attention over the years [231, 235, 236]. For these types of models, the information generated is valuable for forecasting failure, especially for materials which exhibit unimodal failure. Although, the predicted values are only as useful as the accuracy of the input; thus, the size and spatial distribution of defects must be known a priori. In general, the difficulty in these statistical based models is that they require many tests to get a decent statistical representation of the material behavior. In these tests, the samples are treated as being identical to one-another, thus these results are indifferent towards the failure mode or microstructural deviations within the material. In the case of excessive scatter, these models offer little as far as predictive capabilities go. Furthermore, with improvements in processing routes the source of crack initiation is not solely linked to distinct defects such as voids or inclusions, especially in superalloys.

Fatigue lives are dominated by damage formation, which is primarily driven by irreversible dislocation slip. Many damage accumulation models have been established, specifically in the form of stochastic crack propagation [237-240]. By accounting for grain boundaries (GBs), the results show that GBs resist slip and crack advancement resulting in damage preferentially accumulating along GBs [241, 242]. Kato and Mori have made modifications to the well known Coffin-Manson and Palmgren-Miner empirical models to account for statistics based on the accumulation of completely irreversible damage. Their study show that the predicted fatigue lives become much longer when accounting for random

stochastic damage [243]. These types of analyses assume that microcracks are present in the material and are distributed according to a Poisson point process. This assumption has yet to be validated through experimental evidence. Further, the coalescence of these microcracks into a macrocrack in the case of multiple site damage is a stochastic process. It requires knowledge of the cracks spatial and size distributions in addition to knowledge about mechanisms in which they coalesce. This type of problem is very difficult and must be simplified by neglecting the local perturbations in the stress field induced by the cracks and the crack geometry [231]. Another potential problem in these models is the application and break-down of linear elastic fracture mechanics to analyze short cracks with relatively large plastic zones ahead of the crack tips in comparison to the crack lengths.

The collection of probabilistic models used to account for fatigue scatter, as a whole, is missing certain aspects of the material behavior. In addition to this, the aforementioned models are not deterministic, since they do not clearly define a cause and effect rationale to predict failure, nor can they trace this failure back to the microstructural level. For instance, individual models have stated the important influence of GB effects, but these and other microstructural details need to be accounted for in each model. It is well known that the microstructure plays an essential role in fatigue crack initiation, such as grain size, grain orientation, and GB character (not only of a local grain but of its neighboring grains). This type of information must be incorporated in these models to create a robust simulation for crack initiation. One type of model that addresses the effect of microstructure on the early fatigue response is presented by Pryzbyla and McDowell [244], in which they apply a statistical framework to a cyclic crystal plasticity model. In doing so, they are able to determine a fatigue indicator parameter, which establishes the effect of microstructure on the fatigue response of the polycrystalline aggregate.

By use of a cyclic crystal plasticity approach, this method offers a physical understanding of failure, although it is extremely computationally intensive, thus, in its present form, it cannot be used to predict number of cycles to failure.

In this study, we describe an approach to model the energy of a PSB structure and use its stability with respect to dislocation motion as our failure criterion for fatigue crack initiation. From this analysis, we are able to predict the fatigue life of polycrystalline specimens, which rely heavily on the microstructure of the material, namely grain orientations, widely distributed grain sizes, precipitates, GB characters, and the influence of neighboring grains. Once the microstructure characterization is established, we determine the distribution of individual crystallographic properties (such as grain size, Schmid factor, misorientation, and number of neighbors); this allows us to simulate a microstructure for this material by randomly assigning microstructural attributes from these distributions, via a Monte Carlo approach. Hence the scatter and probability of failure are predicted from a deterministic approach, which is driven by the microstructure.

Chapter 3. Material and Experimental Methods

3.1. Material Description

The material utilized in this study is a nickel-based superalloy, Udimet 720 (U720). The nominal chemical composition for U720 is listed in Table 3.1. The primary strengthening mechanism in this material is in the form of ordered Ni_3Al precipitates ($L1_2$ structure), which occurs in this material at three length scales (primary, secondary, and tertiary). The coherency of these γ' precipitate with respect to the γ matrix offers stability along with enhanced strengthening at elevated temperatures. The material underwent a solution process at 1100˚C for 2 hours followed by oil quenching, in order to prepare the matrix for uniform precipitation of γ'. Afterwards, it was aged at 760˚C for 8 hours with air-cooling, in order to precipitate the coarser γ', which offers creep resistance. A second aging process at 650˚C for 24 hours with air-cooling produced fine γ' for strengthening the microstructure for tensile and fatigue loads and stabilizing the γ' precipitates.

Table 3.1. Chemical Composition of U720

Chromium	15.5-16.5
Cobalt	14.0-15.5
Molybdenum	2.75-3.25
Tungsten	1.00-1.50
Titanium	4.75-5.25
Aluminum	2.25-2.75
Carbon	0.01-0.02
Zirconium	0.025-0.05
Boron	0.01-0.02
Nickel	Balance*

Also, during the heat treatment process the γ' acts to pin the grain boundaries, thus determining the grain size in the γ matrix. In this material, there are areas of densely populated γ' along side areas denuded of γ', as shown in Figure 1.3. As a result, a wide distribution of

grain sizes exists, as fine grains form in regions of heavily populated γ' and coarse grains form in regions where γ' is sparse.

The subsequent sections describe our materials testing and characterization. The basic elastic, yield, and lattice structure properties are listed in Table 3.2 for U720 at elevated temperatures, which are of primary concern in this investigation. The testing is predominately low cycle fatigue (LCF) experiments. The characterization is composed of electron back scattering diffraction (EBSD) and transmission electron microscopy (TEM) analysis for the various stages of U720 processing and deformation histories. The eight specimens characterized are listed in Table 3.3. EBSD provides quantitative description of the microstructure, whereas TEM provides a qualitative view of the dislocation and defect structure to fully understand the strengthening and plastic mechanisms present in this material for the various stages of processing and deformation histories.

Table 3.2. Elastic, yield, and lattice parameter properties for U720 at elevated temperature.

Properties	Values	Units
Elastic Modulus	182.2	GPa
Poisson Ratio	0.33	
Yield Strength	1154.7	MPa
Lattice Parameter	3.52	Å
Burgers Magnitude	1.44	Å

Table 3.3. List of specimens characterized through EBSD and TEM analysis in this study.

Specimen	*Description*
Billet	Homogenized, but not heat treated
Forging	As received specimen grip
Low Δε Fatigue	Elevated Temperature ($R_\varepsilon = 0$)
High Δε Fatigue	Elevated Temperature ($R_\varepsilon = 0$)
Tension	Elevated Temperature (failed at 19.1% ductility)
Tension	Room Temperature (failed at 20% ductility)
Compression	Room Temperature (tested to 15.4%)
Compression	Same specimen (with higher resolution scan)

3.2. EBSD Analysis

The EBSD results provide crystallographic texture, grain orientation, misorientation between grains, and grain size, which are crucial in determining the mechanical behavior of the material. Figure 3.1 shows a schematic of grain orientations (including unit normals and angles) and an EBSD scan of typical U720 material. Prior to EBSD, the samples were electropolished utilizing a solution composed of 60 vol.% methanol, 34 vol.% butanol, and 6 vol.% perchloric acid at -20 °C. The raw data obtained were first analyzed using TSL OIM commercial software [245] to obtain grain orientations.

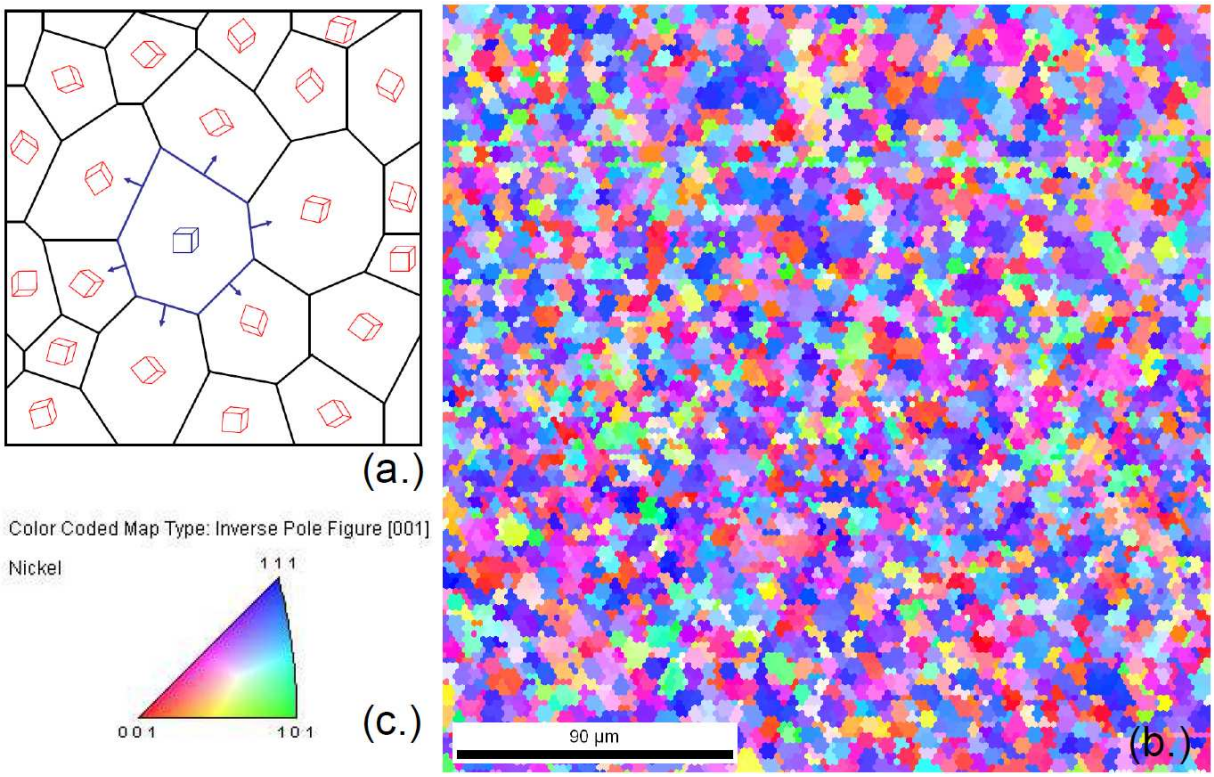

Figure 3.1. (a) Schematic of the orientations of grains in a polycrystal. (b) EBSD scan of U720, where the different colors represent orientations of individual grains. (c) Each color can be mapped to its projection on the stereographic triangle.

The EBSD results showed that the billet, forged, and fatigue specimens were not textured, i.e. the orientations of the grains within the aggregate displayed nearly a random

distribution, as shown by the pole (Figure 3.2) and inverse pole figures (Figure 3.3). Therefore, the fatigue loading of the specimens did not result in grain rotation or texturing of the material at low and high strain ranges. Meanwhile, the monotonic tensile and compression specimens displayed a <111> and <110> texture, respectively. As expected, due to the large deformations each specimen experienced during testing, the grains in the polycrystalline material rotated and aligned to the loading axis. For each case, the primary slip caused the tensile and compression axes to rotate towards the [101] and $[11\bar{1}]$ slip directions, respectively, as shown in Figure 3.4.

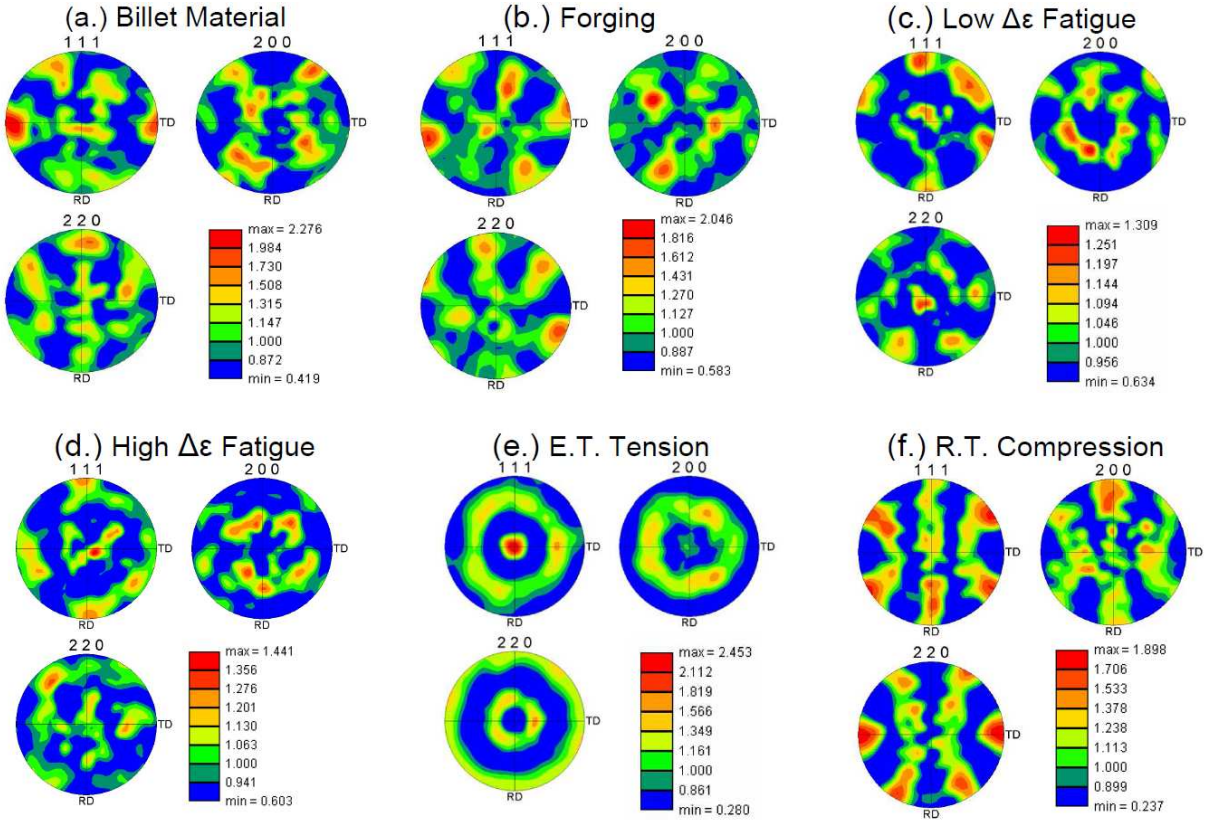

Figure 3.2. Pole figure displaying the texture of the scanned specimens. The samples did not display a strong texture with the exceptions of the tensile (<111> texture) and compression (<110> texture) specimens.

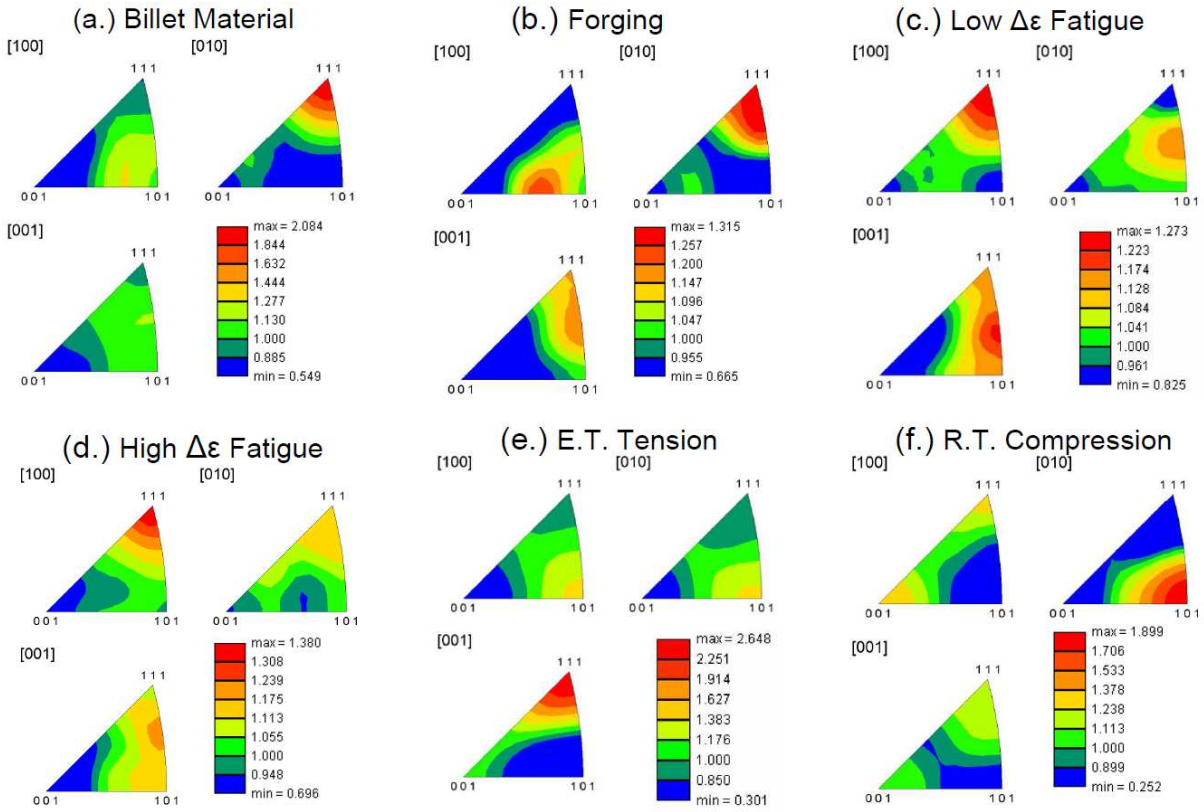

Figure 3.3. Inverse pole figure displaying the texture of the scanned specimens.

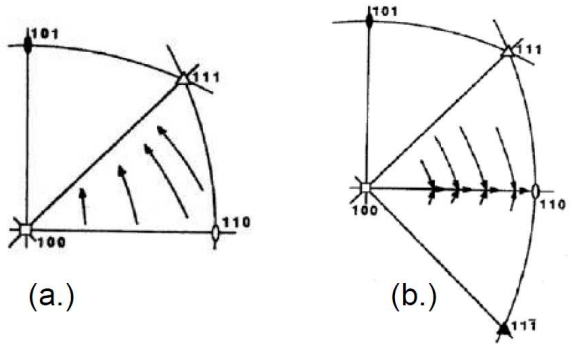

Figure 3.4. In FCC metals, primary slip in the $[101]$ direction causes the tensile and compression axis to rotate toward $[101]$ and $[11\bar{1}]$, respectively. Schematic taken from [246].

From the EBSD scans of these seven specimens, a total of 29,035 grains were analyzed. The grain area was measured during each EBSD scan. From this data, the grain size was calculated assuming a circular cross-section and the results are shown in Figure 3.5 and the statistics of shown in Table 3.4. On average the billet material displayed the smallest grain size,

as expected since this material underwent a homogenization process but did not experience the standard heat treatment aforementioned. Hence, the grains were not able to grow during heat treatment. Further, the grain sizes of the forging and compression sample were much finer compared with the other specimens. All of the samples (except the billet material) were taken from specimens radially cut from a forging. The forging (as-received) and compression samples were cut from the grips of these specimens; hence they were taken from the rim of the forging, which is known to display a finer grain structure.

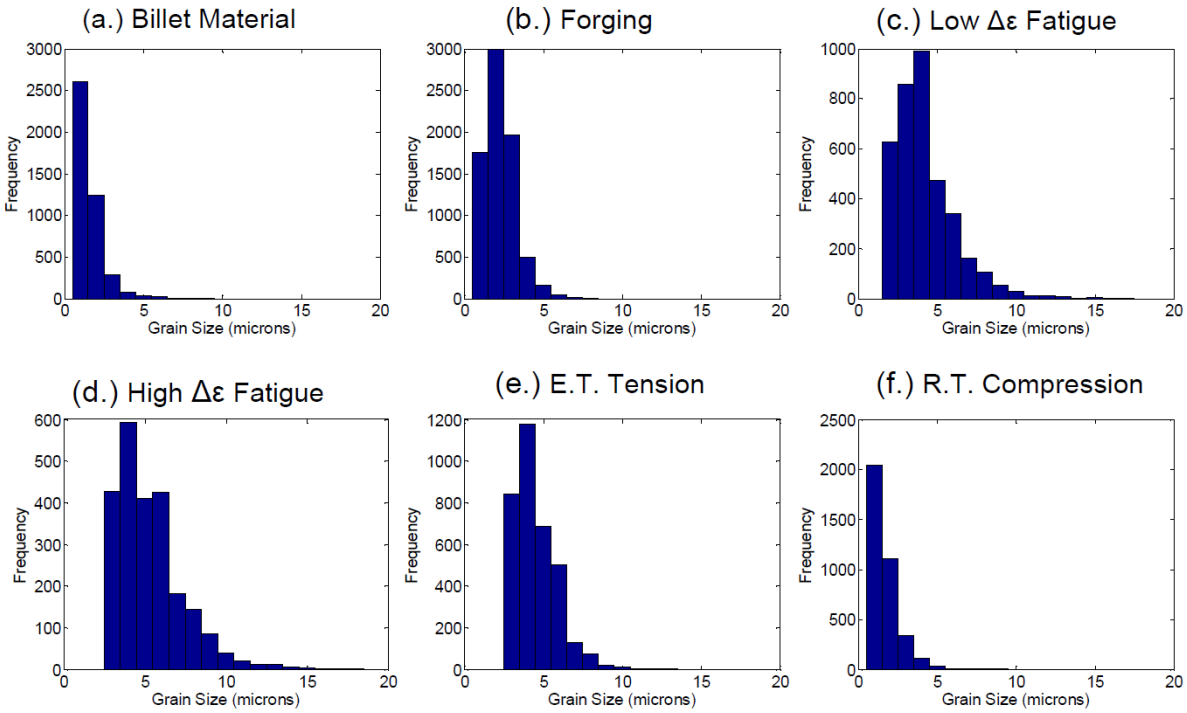

Figure 3.5. Grain size distributions of each specimen analyzed.

The mean grain size is 3.3 μm (averaged across all specimens cut from the forging) although grains can reach as large as 18.4 μm (Figure 3.5d). Thus, a small step size in the EBSD scans had to be used to accurately cover the small grains. At the same time, the bigger grains required large area scans for statistically meaningful data. Thus, in a typical scan, a few thousand grains were analyzed, as shown in Table 3.4. However, the good signal to noise ratio

of the EBSD patterns obtained from the electropolished samples allowed for relatively fast data acquisition for a single pattern, resulting in acceptable total measurements times. The long tail of each grain size distribution shown in Figure 3.5 suggests a bi-modal like distribution of grain sizes with large variations.

Table 3.4. Statistics from each EBSD scan, where the Taylor factor is determined for uniaxial loading.

	Billet	Forging	Fatigue-Low Δε	Fatigue-High Δε	Tensile-ET	Compress-RT
Number of Grains Scanned	4,265	7,424	3,664	2,373	3,457	3,662
Total Area of Grains Scanned	9,948	37,310	60,542	60,254	57,198	9,963
Average Grain Size (μm)	1.5	2.4	5.3	4.2	4.4	1.6
Standard Deviation - Grain Size (μm)	0.86	0.89	2.18	1.87	1.33	0.93
Maximum Grain Size (μm)	9.0	8.3	18.4	16.7	13.4	8.7
Number of Interfaces Detected	28,623	47,370	24,018	15,546	21,118	24,703
Average GBs per Grain	5.7	5.4	6.6	6.6	6.1	5.7
Taylor Factor	3.089	3.070	3.074	3.065	3.103	3.075

Further, due to the variation in grain sizes and neighboring grains, each grain can have a wide distribution of associated GBs. Given a sufficiently large sample size, a 2D EBSD measurement of the grain area is capable of producing accurate representation of the grain size compared to 3D data [247]. A histogram of the number of GBs belonging to each grain is shown in Figure 3.6. A typical 2D scan showed that each grain has a mean value of ~6 interfaces, but some grains had more than 25 GBs.

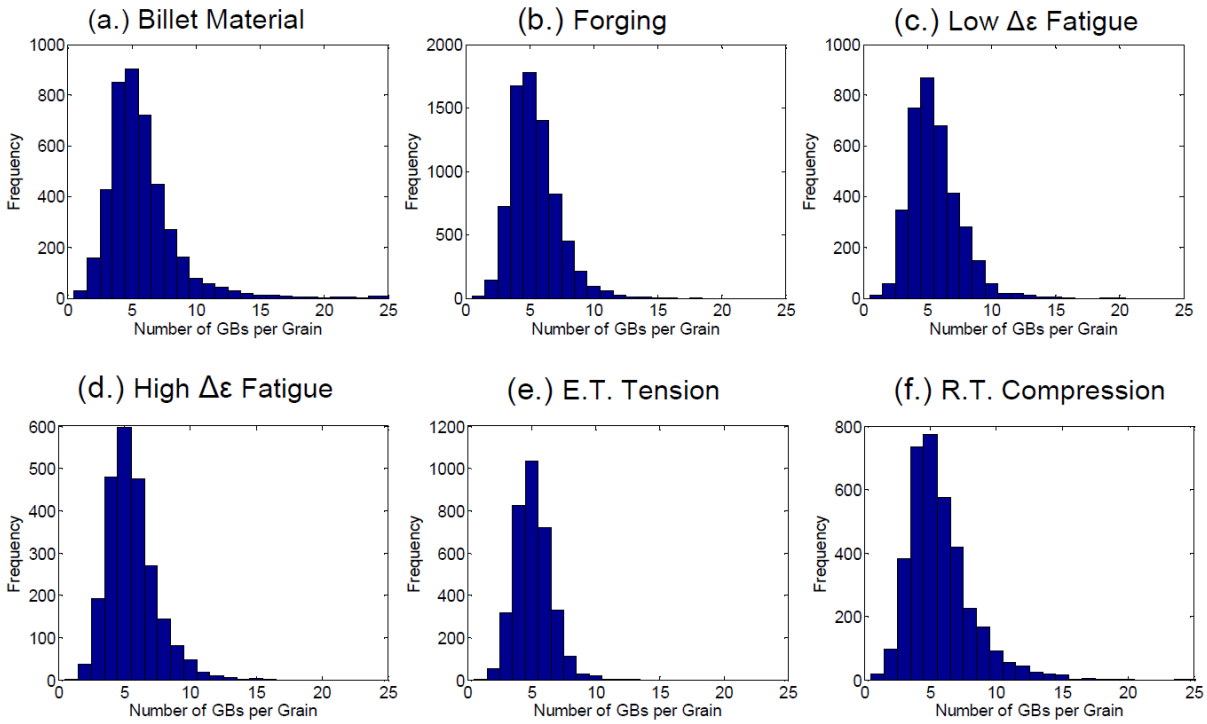

Figure 3.6. Histogram of the number of GBs (adjacent grains) per grain for each EBSD scan.

Given the adjacent grain information, we can define the misorientation between grains and establish its distribution for each EBSD scan, as shown in Figure 3.7. From these distributions, we see large number of ~60˚ misorientation, which is indicative of twin boundaries (TBs), as depicted in Figure 2.3. There are two types of twins, annealing and deformation twins. We see that the twin density is high due to heat treatment (Figure 3.7b) and does not increase in the subsequent testing (deformation due to tensile, compressive, or fatigue loading). Thus, the twin density in this material is composed of annealing twins, which is typical of a nickel-based superalloy. The misorientation distibutions did not substantially change from forging to fatigue testing regardless of the applied strain amplitude. Hence, during fatigue deformation, the interfaces stayed intact. By contrast, tensile testing resulted in unidirectional deformation to the specimen and a change in the misorientation distribution, as shown in Figure 3.7e. As previously mentioned, the primary slip rotated the tensile axis to the [101] direction resulting in <111>

texture. In doing so (for the tension specimen and similarly the compression specimen), the misorientations were redistributed into mostly low-angle, thus annihilating many of the twins.

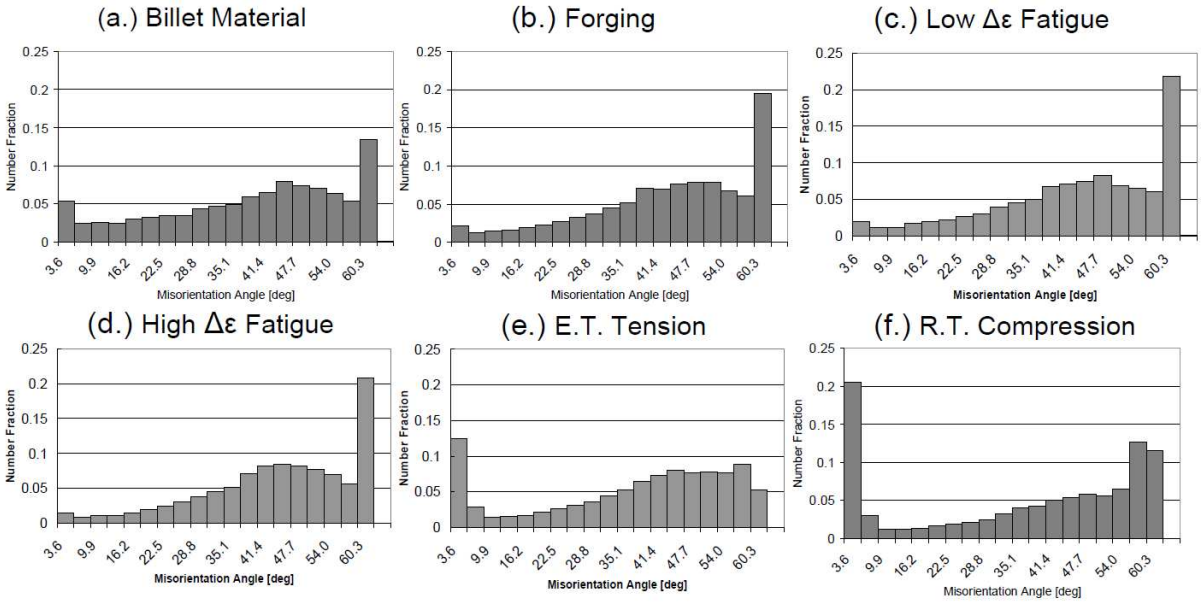

Figure 3.7. Misorientation distributions of each specimen analyzed.

3.3. Fatigue Experiments

In this study, a total of 84 strain-controlled low cycle fatigue experiments were conducted on U720 specimens at three strain ranges (normalized values of 1.00% (18 specimens), 0.73% (47 specimens), and 0.69% (19 specimens), whereas each strain range is divided by the maximum tested strain range) at elevated temperatures and $R_\varepsilon = 0$. The results are shown in Figure 1.1. During reverse cycling, the specimens experience considerable compressive plasticity, thus we believe the PSB behavior in our strain-controlled experiments (strain ratio R = 0) is comparable to fully-reversed studies (R = -1) in literature. Crack initiation was defined as the measured load dropping to a level of 90% of the saturated value. The fracture surface of the failed fatigue specimens were analyzed to study the mechanism for crack initiation, as shown in Figure 3.8. Transgranular failure is observed and is of primary interest in this study. From Figures 3.8b,c, twinning is observed near the facet features, thus indicating that cracks initiate

near the twin boundaries, as reported in literature [207, 218-223]. From the 89 fatigue experiments displaying transgranular facets, the facet size was measured, as shown by the histogram in Figure 3.9.

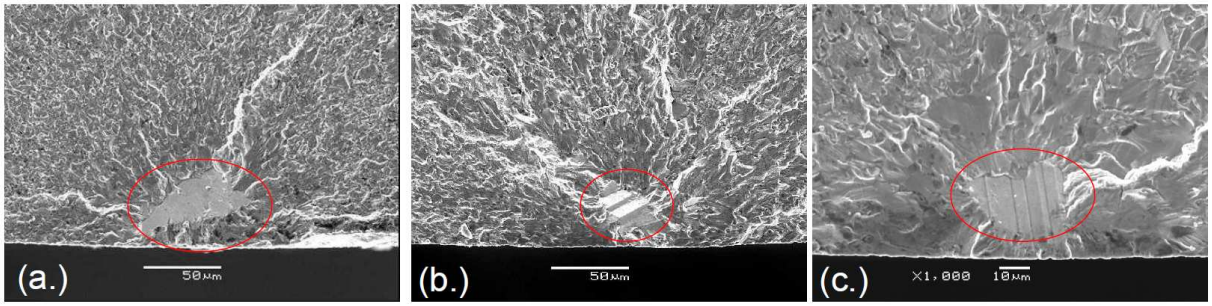

Figure 3.8. Fracture surface of failed fatigue specimens, cracks initiate from facets, although considerable plasticity is involved in forming this feature. From (b.) and (c.), we can see evidence of twinning near the facets.

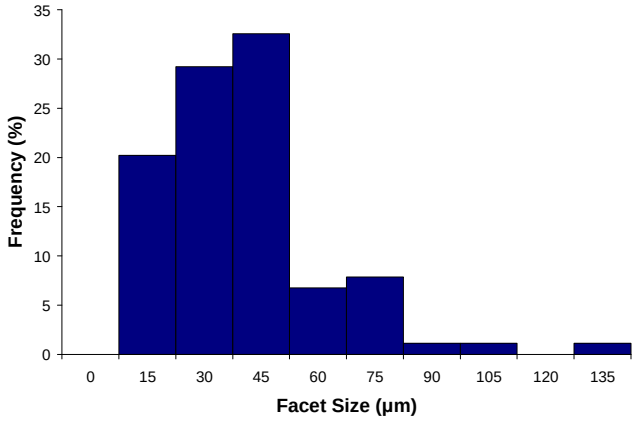

Figure 3.9. Histogram of the facet features measured from 89 failed fatigue specimens. The measured statistics from this facet analysis produced: average - 39.9 μm, standard deviation - 20.7 μm, minimum – 15 μm, and maximum – 130 μm.

3.4. TEM Analysis

Material characterization in the form of TEM analysis was performed, which provided a qualitative indication of the material behavior, thus providing key insights that can be used to model the microstructure and resulting dislocation arrangements. From this TEM analysis, we draw many insights into the strain localization that ultimately leads to failure within U720. In

the fatigued samples, slip and plastic strain are localized into banded regions. Figure 3.10a shows a low-magnification TEM image of persistent slip bands in U720, and a more detailed view of two bands in this structure is shown in Figure 3.10b. Similarly, the observation of persistent slip band formation has been observed in literature for U720 [248-250] and is the precursor to crack initiation and material failure.

The formation of the persistent slip bands occurs in preferentially oriented grains. Slip interacts with the grain boundary causing pile-up of dislocations and stress concentration, which results in slip penetrating into the second grain. By viewing the high magnification image (Figure 3.10b), we see that the slip band forms by dislocations shearing the γ' precipitates. This effectively weakens the precipitate as an obstacle for future dislocations to penetrate (cutting reduces the effective size of the precipitate and the ordering of the Ni_3Al intermetallic structure) and concentrates plastic deformation into a small volume. This results in slip being confined to a single glide plane (a 2D planar feature). Initially one slip band forms as the precipitates are cut at the weakest spot, since this alloy has a statistical distribution of local strength (i.e. interparticle distances). However, the increase in dislocation density hardens the slip band, and thus cutting sets in at the next weakest plane. Consequently, we get an increasing number of slip bands with cycle number, but not much change within the bands, which macroscopically results in cyclic saturation.

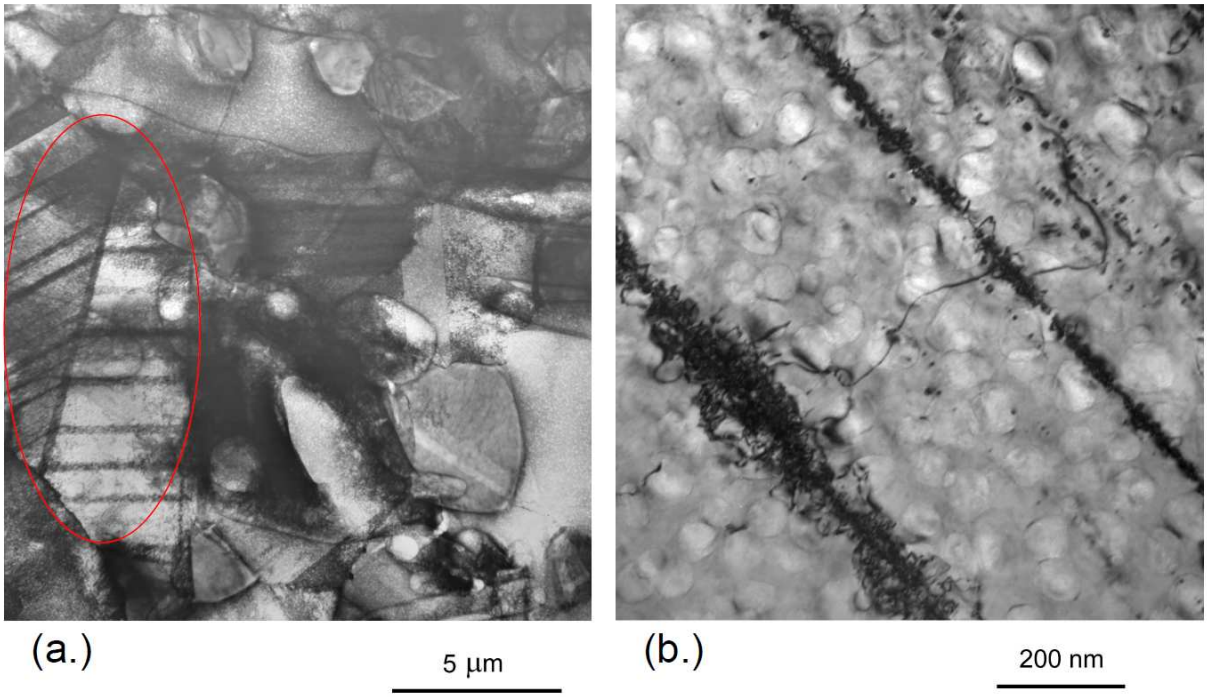

Figure 3.10. (a.) A low-magnification TEM image of persistent slip bands (shown within the red ellipse). (b.) a high-magnification image of two bands in a failed fatigue specimen of U720 tested at a high strain range, R = 0, and elevated temperature.

In this study, we formulate a model for predicting fatigue crack initiation in a wrought nickel-based superalloy, Udimet 720 (U720), although this methodology could be used to characterize fatigue in a variety of metals and alloys. This material was chosen due to the complexities and wide-distributions of microstructural features (especially grain size variability), further validating our model. The material exhibits a large twin volume fraction, is susceptible to the formation of persistent slip bands through shearing the matrix and precipitates, and at the same time, is interesting from an application point of view.

Chapter 4. Grain Boundary Characterization

4.1 Overview

In many engineering alloys, there exists a wide distribution of grain sizes; we investigate the role of grain boundaries as a strengthening mechanism in such a material. The coincidental site lattice (CSL) model is a powerful mathematical tool to characterize grain boundaries (GBs) and identify 'special' boundaries, which display beneficial mechanical behavior. We define the CSL and describe a detailed procedure to obtain this information from the grain orientation mapping via electron back scattering diffraction (EBSD). From this information, we show the evolution of the CSL for a nickel-based superalloy, Udimet 720 (U720), throughout various stages of processing (billet and forging) and experiments (tension, compression, and fatigue). A deeper level of understanding the GB's role in the mechanical behavior of the material is investigated through atomic simulations using molecular dynamics (MD) as the GB energy is determined for the most prevalent GBs within this material. The spatial map of the orientation and grain sizes measured from EBSD is linked to the GB energies calculated from MD. Based upon the large number of boundaries analyzed (29,035), there is a strong inverse correlation between GB energy and grain size for every specimen examined during the various processing and testing conditions.

4.2. CSL Procedure

From the EBSD scan, the orientation of each grain (Euler angles) in the scan and a list of the neighboring grains was obtained. From the Euler angles, (φ_1, Φ, φ_2), the rotation matrix, $\boldsymbol{g}$, of each grain is then found by:

$$g = \begin{bmatrix} \cos\varphi_1 \cos\varphi_2 - \sin\varphi_1 \sin\varphi_2 \cos\Phi & \sin\varphi_1 \cos\varphi_2 + \cos\varphi_1 \sin\varphi_2 \cos\Phi & \sin\varphi_2 \sin\Phi \\ -\cos\varphi_1 \sin\varphi_2 - \sin\varphi_1 \cos\varphi_2 \cos\Phi & -\sin\varphi_1 \sin\varphi_2 + \cos\varphi_1 \cos\varphi_2 \cos\Phi & \cos\varphi_2 \sin\Phi \\ \sin\varphi_1 \sin\Phi & -\cos\varphi_1 \sin\Phi & \cos\Phi \end{bmatrix} . \quad (4.1)$$

This allows us to calculate the misorientation rotation matrix, Δg, between each grain and its neighbor,

$$\Delta g = g_1^{-1} g_2 . \quad (4.2)$$

However, the misorientation matrix is not unique, since FCC materials have cubic symmetry. Thus, the misorientation matrix must be rotated about threefold axes (plus the identity) or in other words multiplied by the 24 cubic symmetry operators (known as class 432, O_{432}), where each symmetry operator is a rotation of the identity tensor. A loop is created over each symmetry operator to ensure that a minimum value of the misorientation between grains, Θ, is found.

$$\Theta = \min \left| \cos^{-1} \left\{ \frac{tr(O_{432} \Delta g) - 1}{2} \right\} \right| \quad (4.3)$$

During the EBSD scan, the minimum misorientation to define a GB was specified as 2˚, hence between two points a misorientation less than 2˚ was categorized as an internal grain rotation, whereas a larger misorientation indicated the presence of a GB.

As described in Chapter 2, we need a total of five degrees of freedom to fully characterize a GB, three for the misorientation and two to describe the plane of the GB [48-60, 66, 67]. In this work, we utilize an axis-angle pair scheme, which specifies the misorientation across the GB with an axis of misorientation (*UVW*) along with an angle (θ), as shown in Figure 4.1.

$$\theta = \cos^{-1} \left(\frac{\Delta g_{11} + \Delta g_{22} + \Delta g_{33} - 1}{2} \right) \quad (4.4)$$

$$(U,V,W)=\frac{(\Delta g_{23}-\Delta g_{32},\Delta g_{31}-\Delta g_{13},\Delta g_{12}-\Delta g_{21})}{\sqrt{(\Delta g_{23}-\Delta g_{32})^2+(\Delta g_{31}-\Delta g_{13})^2+(\Delta g_{12}-\Delta g_{21})^2}} \tag{4.5}$$

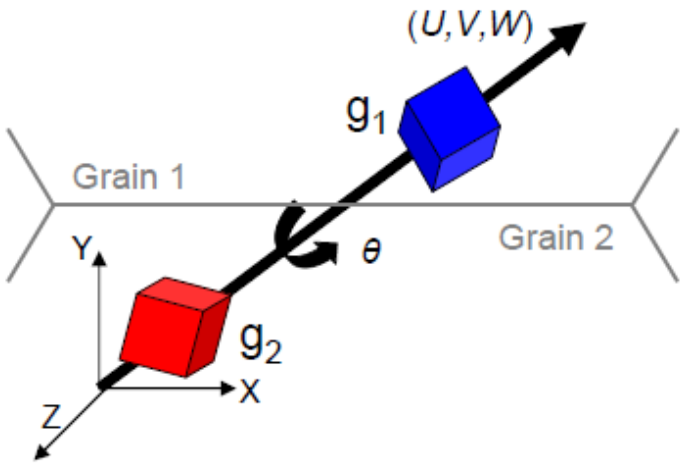

Figure 4.1. Schematic of the axis-angle pair for grain boundary description.

This gives the GB misorientation but not the GB plane. Thus, the description of the GB is matched with the axis-angle pair to specify its CSL value according to a reference table provided by Grimmer, Bollmann, and Warrington that includes the axis-angle pair for 47 Σ values from Σ3 to Σ49 [38]. The allowable tolerance between the measured and reference value of axis and angle is given using the Brandon condition [26]:

$$\vartheta=\vartheta_o\Sigma^{-1/2}, \tag{4.6}$$

where ϑ_o is the misorientation limit for a low-angle GB, set at 15˚. Thus, a low-angle GB (LAGB) is defined as a misorientation in the range of 2˚-15˚ and denotes a Σ1 GB. The Brandon condition has been chosen in this investigation compared to other criteria due to its accuracy and widespread application in literature. Hence, from this description, a Σ3 GB can have a deviation up to 8.66˚ and still display 'special' properties, which has been confirmed by experiments [27]. Further, the Brandon condition is invoked on each component of the axis-angle pair, thus

$\left|\theta' - \hat{\theta}\right| \leq \vartheta$ and $\left|(U',V',W') \bullet \left(\hat{U},\hat{V},\hat{W}\right)\right| \leq \vartheta$ must be satisfied to define a Σ GB, where the ^ and ′ denotes the reference and measured values, respectively.

It should be noted that the CSL Σ value is not a unique description of the GB, although for ease of reporting, we plot the CSL Σ values, as shown in Figures 4.2-4.6, albeit all calculations are performed based on the axis-angle pair description of the GB. In Figure 4.2, a histogram is shown of the CSL values for U720 material from the billet and forging. It can be seen that approximately 60% of the CSL values are comprised of low-angle GBs (Σ1s) and twins (Σ3s). The amount of low-angle GBs decrease during the forging process as the large deformation leads to additional misorientation within the aggregate of grains. The forging material has undergone a heat treatment, which increases the population of annealing twins within the material and as a consequence the population of Σ3 GBs.

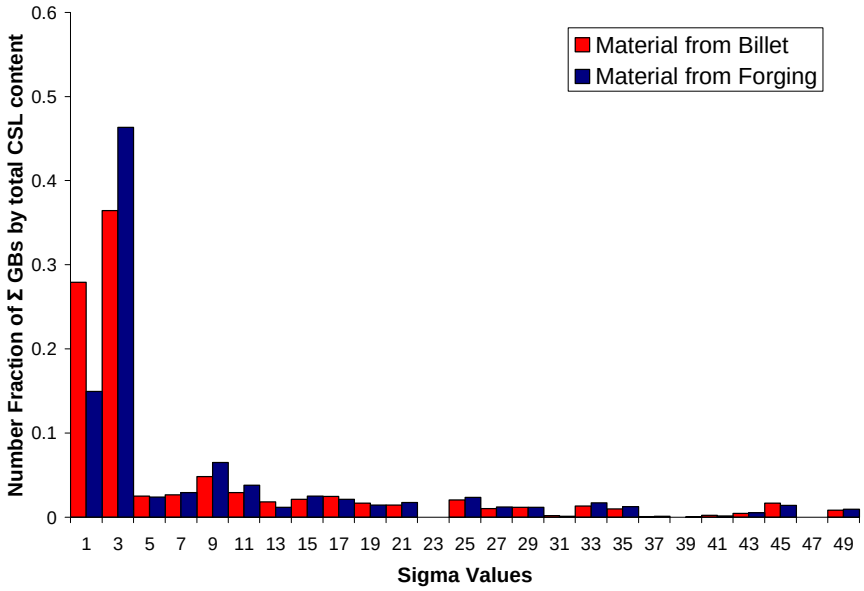

Figure 4.2. Histogram of CSL values for material from billet and forgings of U720.

Similarly, the CSL values were measured from EBSD scans of fatigue specimens after failure, as shown in Figure 4.3. Interestingly, the CSL Σ values and GB character distributions

did not substantially change from forging to fatigue testing regardless of the applied strain amplitude. Hence, during fatigue deformation, the Σ GBs stayed intact. By contrast, tensile testing resulted in unidirectional deformation to the specimen and a change in CSL distribution, as shown in Figure 4.4. The tensile specimens failed at a ductility of approximately 20%, and, as previously mentioned, the primary slip rotated the tensile axis to the [101] direction (Figure 3.4) resulting in <111> texture (Figure 3.2e). In doing so, the GB characters were redistributed into mostly Σ1 LAGBs, thus annihilating many of the Σ3 twins. The difference in test temperature from room to elevated temperature did not have a significant impact in the CSL distribution.

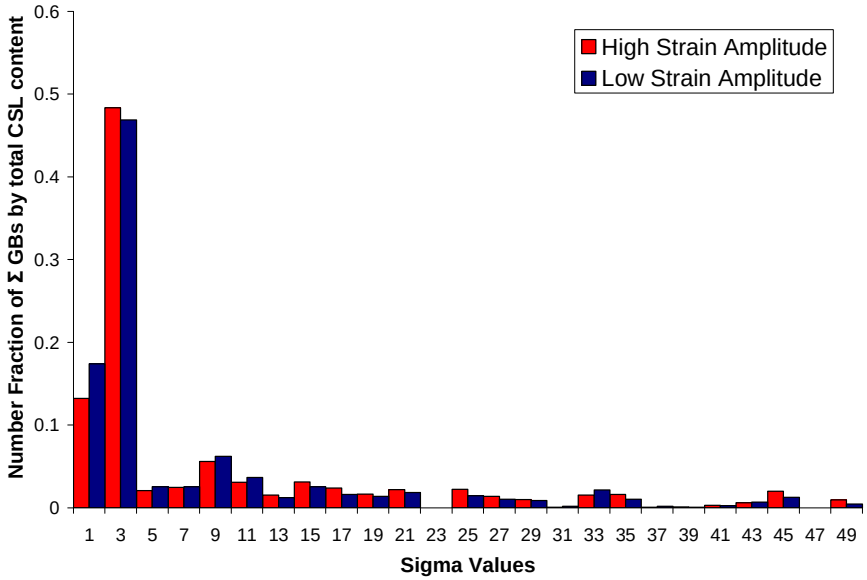

Figure 4.3. Histogram of CSL values for specimens of U720 after fatigue testing at elevated temperature.

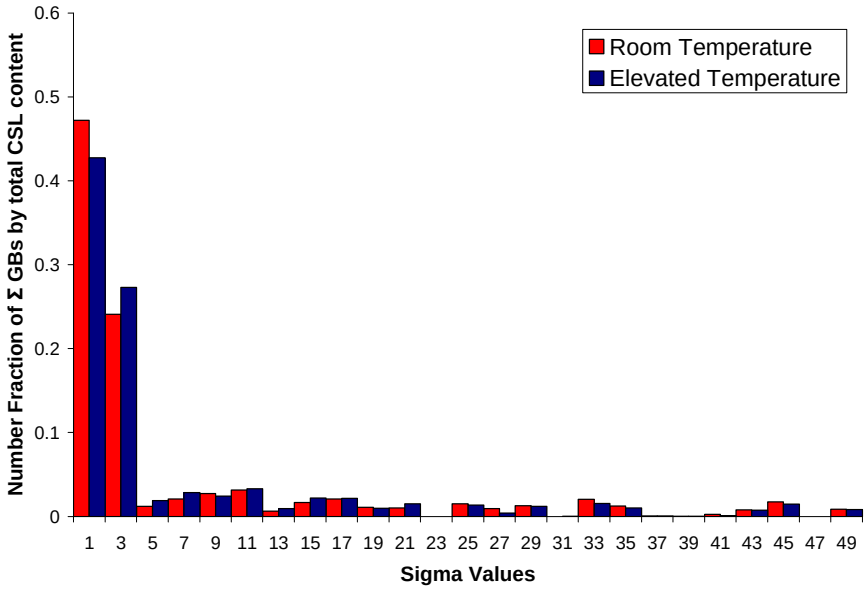

Figure 4.4. Histogram of CSL values for specimens of U720 after tensile testing to failure (approximate ductility of ~20%).

Figure 4.5 shows CSL data obtained with EBSD on a compression specimen tested to approximately 16% engineering strain. As previously discussed, the large amounts of strain forced the compression axes to rotate towards the $[11\bar{1}]$ slip direction (Figure 3.4) resulting in <110> texture (Figure 3.2f), although the CSL distribution did not dramatically change as was the case under tensile loading. There existed a slight increase in LAGBs due to the increase in texture and alignment of grains. Also, the population of Σ3 GBs slightly increased, which could possibly be attributed to deviations within the microstructure as a smaller sample area was scanned. The EBSD measurements on this compression specimen were performed at two distinct resolutions, in order to check the statistical significance of the data. The results were not substantially different; although due to the increase in magnification, fewer grains with a different number of data points per grain were scanned in the high magnification case. This is not surprising as the procedure that was described above analyzed the orientation over an entire grain and defined the GB relative to the orientation of each neighboring grain. The CSL results

for each specimen analyzed using our method are summarized in Table 4.1, which gives the values for the number of grains and grain boundaries detected during the EBSD scan. Further the quantified values are reported for the average grain size, ratio of CSL boundary content versus the total number of GBs (including irrational types), and population of low-angle grain boundaries and twins.

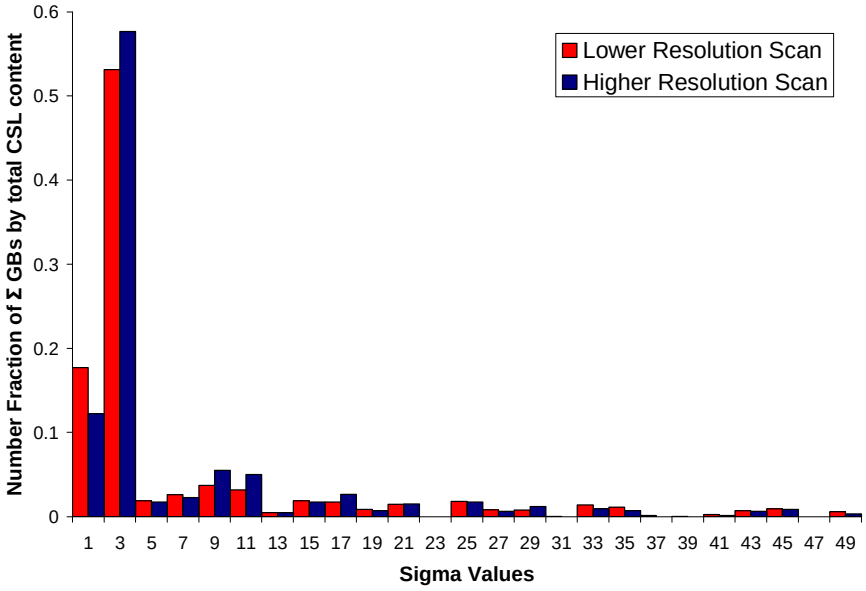

Figure 4.5. Histogram of CSL values for specimens of U720 after compression testing to approximately 16% engineering strain obtained through our EBSD analysis at two different scanning resolutions.

Table 4.1. Statistics from the CSL analysis throughout various stages of processing and deformation.

	Billet	Forging	Fatigue-low Δε	Fatigue-high Δε	Tensile-Room Temp	Tensile-High Temp	Com-pression Low Res	Com-pression High Res
Number of Grains Scanned	4,265	7,424	3,664	2,373	3,486	3,457	3,662	704
Total Area of Grains Scanned	9,948	37,310	60,542	60,254	56,803	57,198	9,963	2,479
Average Grain Size (sq. μm)	2.3	5.0	16.5	25.4	16.3	16.6	2.7	3.5
Number of Interfaces Detected	28,623	47,370	24,018	15,546	21,147	21,118	24,703	4,345
GBs within CSL (#)	6,593	11,504	6,220	3,637	5,480	5,329	6,524	1,275
GBs within CSL (in %)	23.03%	24.29%	25.90%	23.40%	25.91%	25.23%	26.41%	29.34%
LAGBs - Σ1 (#)	1,841	1,718	1,083	480	2,588	2,278	1,157	156
LAGBs - Σ1 (in %)	6.43%	3.63%	4.51%	3.09%	12.24%	10.79%	4.68%	3.59%
Twins - Σ3 (#)	2,401	5,330	2,915	1,758	1,320	1,455	3,467	735
Twins - Σ3 (in %)	8.39%	11.25%	12.14%	11.31%	6.24%	6.89%	14.03%	16.92%

As discussed, our method views the average orientation of each grain via its Euler angles and compares the information to its neighboring grains. Thus the information received about the CSL corresponds to the entire GB segment between adjacent grains. This methodology is in stark contrast to commercial codes such as HKL [245]. In such software, the EBSD analysis is performed in a point by point grid. Any misorientation between two points greater than a threshold (2˚ by default) is designated as a GB. Hence, the GB is composed of pixilated and serrated fragments. As a consequence, the reported CSL values are also pixilated; thus a segment between two adjacent lattices can be comprised of fragments containing various CSL characters. In this case, the resolution of the EBSD scan plays an important role in determining the CSL distribution as shown in Figure 4.6, as the histogram is considerably changed for a high versus low resolution scan across the same material.

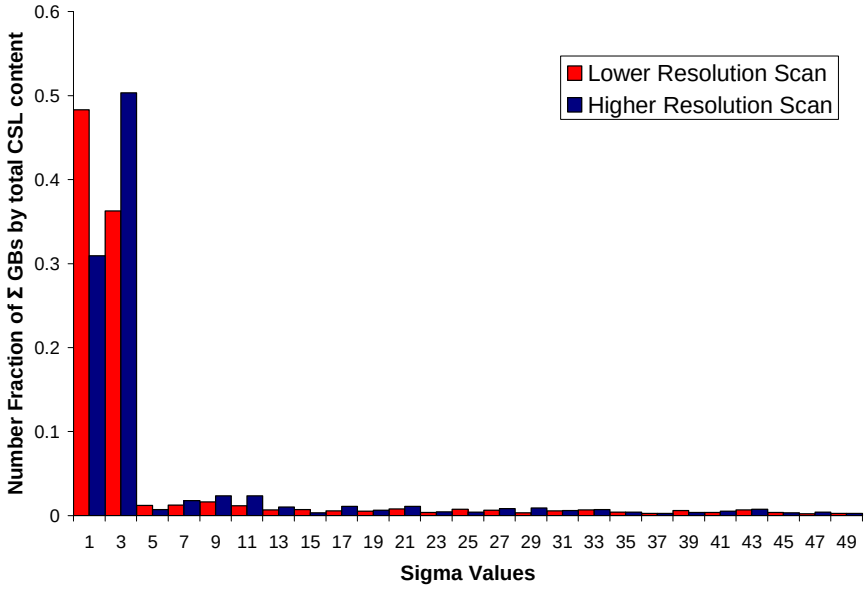

Figure 4.6. Histogram of CSL values for specimens of U720 after compression testing to approximately 16% engineering strain obtained through EBSD analysis at two different scanning resolutions. Analysis is completed with commercial HKL software by looking at pixilated segments along the GB.

Further, the CSL characters of the entire GB segment separating adjacent grains are physically more relevant versus a pixilated view. Hence, the CSL distributions obtained from

the two methods are essentially different techniques and do not yield the same type of information as shown comparing Figures 4.5 and 4.6. Although we contend that the information presented in Figure 4.5 from our methodology is more pertinent to the mechanical behavior and physics of the grain boundary as is the aim of this investigation. The next level of understanding the role of GBs is to measure their energy values through atomic simulations as described in the next section.

4.3. GB Energy

4.3.1. MD Set-up

To capture the physics at the grain boundary interface, it is necessary to investigate this problem at a smaller scale. Atomic simulations were utilized in the form of a molecular dynamics (MD) code called LAMMPs [251, 252] to study the effects of grain misorientation on the energy of its interface and to service our model. A system was set up to investigate a grain with a specific (mis)orientation 'sandwiched' between two similar grains, representing a specific tilt or twist GB with a corresponding CSL Σ value, as shown in Figure 4.7. Grains 1 and 2 in the structure were created with a specific orientation to represent distinct CSL boundaries (Table 4.2), in which the boundary plane is represented by ***n***. For tilt and twist GBs, the axis of rotation is represented by ***c*** and ***n***, respectively.

Table 4.2. For each tilt and twist GB, the axis and angle of rotation is displayed along with the resulting CSL Σ value and boundary plane normal. For tilt GBs, the axis of rotation is normal to the boundary plane. For twist GBs, the axis of rotation aligns with the boundary plane normal.

<110> Tilt GBs				<111> Twist GBs				<001> Tilt GBs			
Rotation Axis	Rotation Angle (˚)	Σ value	Boundary Plane	Rotation Axis	Rotation Angle (˚)	Σ value	Boundary Plane	Rotation Axis	Rotation Angle (˚)	Σ value	Boundary Plane
[110]	0.00	1	{001}	[111]	0.0	1	{111}	[001]	0.0	1	{100}
[110]	13.44	73	{1,1,12}	[111]	9.4	111	{111}	[001]	14.3	65	{810}
[110]	20.05	33	{118}	[111]	13.2	57	{111}	[001]	16.3	25	{710}
[110]	26.53	19	{116}	[111]	17.9	31	{111}	[001]	22.6	13	{510}
[110]	31.59	27	{115}	[111]	21.8	21	{111}	[001]	26.0	89	{13,3,0}
[110]	38.94	9	{114}	[111]	26.0	237	{111}	[001]	28.1	17	{410}
[110]	44.00	57	{227}	[111]	27.8	13	{111}	[001]	36.9	5	{310}
[110]	50.48	11	{113}	[111]	32.2	39	{111}	[001]	41.1	73	{830}
[110]	58.99	33	{225}	[111]	38.2	7	{111}	[001]	48.9	73	{11,5,0}
[110]	70.53	3	{112}	[111]	42.1	93	{111}	[001]	53.1	5	{210}
[110]	80.63	43	{335}	[111]	44.8	129	{111}	[001]	61.9	17	{530}
[110]	86.63	17	{223}	[111]	46.8	19	{111}	[001]	64.0	89	{850}
[110]	93.37	17	{334}	[111]	49.6	5	{111}	[001]	67.4	13	{320}
[110]	99.37	43	{556}	[111]	52.7	61	{111}	[001]	73.7	25	{430}
[110]	109.47	3	{111}	[111]	60.0	3	{111}	[001]	75.7	65	{970}
[110]	121.01	33	{554}					[001]	77.3	41	{540}
[110]	129.52	11	{332}					[001]	79.6	61	{650}
[110]	141.06	9	{221}					[001]	90.0	1	{010}
[110]	148.41	27	{552}								
[110]	153.47	19	{331}								
[110]	159.95	3	{441}								
[110]	166.56	73	{661}								
[110]	180.00	1	{001}								

In each structure, the FCC lattice is comprised of atoms with the Foiles-Hoyt Ni embedded atom method (EAM) potential, chosen to match the stable and unstable stacking fault energy of the material [253]. This EAM potential for Ni was chosen to match the intrinsic, γ_{SF}-127 mJ/m^2, and unstable, γ_{US}-255 mJ/m^2, stacking fault energies of the material, which compares well with experimental values of 125-128 mJ/m^2 and ab initio calculations of 273 mJ/m^2 for the γ_{SF} and γ_{US} energies, respectively [254]. It is critical to obtain reasonable values of the unstable stacking fault energy as this parameter has been tied to the mechanics of defects [255]. Also, the lattice constant of this EAM potential, 3.52 Å, exactly matches that of nickel. Periodic boundary conditions are enforced in all three directions to represent bulk material, and the simulation cell

is of sufficient size (*L,B,W* refer to Figure 4.7) to negate boundary-boundary strain field interactions or 'cross-talk' of the GBs:

$$L = \alpha\sqrt{h^2 + k^2 + l^2} \geq 8nm \tag{4.7}$$

$$B,W = \beta\sqrt{h^2 + k^2 + l^2} \geq 5nm \tag{4.8}$$

where *h,k,l* are the Miller indices for the three orthogonal vector representations of each grain orientation and α and β are scalars to satisfy the size requirements.

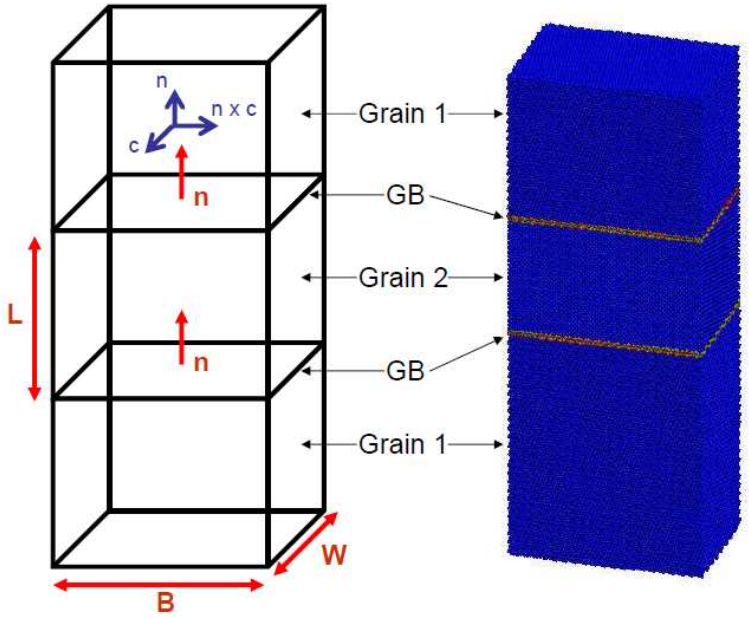

Figure 4.7. Grain boundary set-up for the atomic simulation displaying a pair of GBs per system. The normal to the GB, ***n***, represents the boundary plane. The axis of rotation for tilt and twist GBS is ***c*** and ***n***, respectively. The geometry (*L, B, W*) is chosen to satisfy periodic boundary conditions and avoid GB-GB interactions.

The system is first annealed to 800K and then quenched to 10K, afterwards the atoms are statically equilibrated or 'relaxed' using the conjugant gradient method to obtain the energy of the system of *N* atoms containing the pair of CSL boundaries, E_{CSL}^{GB}. Further, the box dimension in only the direction normal to the GB was allowed to relax, in order to alleviate any GB pressure. The energy associated with the grain boundary was calculated as follows:

$$\gamma_{GB} = \frac{E_{CSL}^{GB} - \frac{N}{M} \cdot E_{Perfect}^{FCC}}{2A}, \tag{4.9}$$

where A is the area of the GB ($B \cdot W$) and the factor of two is necessary since the system contains two GBs. In order to isolate the GB energy, we must remove the potential energy of the atoms in the lattice, $E_{Perfect}^{FCC}$ (4.45 eV per M atoms).

4.3.2. Results

The simulation was repeated for various twist and tilt grain boundary angles about various axes as the set-up details are listed in Table 4.2 and the results are shown in Figures 4.8-4.10. In Figure 4.8, a tilt GB is constructed about a rotation along the <110> axis of the crystal. It can be seen that this curve contain local minimums and cusps corresponding to preferred energy configurations as a result of the special Σ GBs in the CSL, which concurs with simplified defect structures at the interface as described by the structural unit model [42-47, 65]. At a rotation of 0˚, the atoms are in a perfect lattice configuration. At a rotation of 50.48˚, the defect structure at the interface is simple, therefore corresponding to a local minimum in the energy and the Σ11 GB. A 109.47˚ tilt rotation about the <110> axis has the lowest energy of any GB, which corresponds to a very simple defect structure known as a coherent twin or the Σ3 GB, as previously shown in Figure 2.2. For this reason, these boundaries are most abundant in this material as annealing twins form during processing, as shown in Figures 4.2-4.3. A characterization of 900 GBs in pure annealed nickel performed by Randle showed that over half of the interfaces consist of <110> tilt GBs [50]. Hence, the <110> tilt GBs are a preferred interface configuration and of importance for FCC materials and nickel alloys.

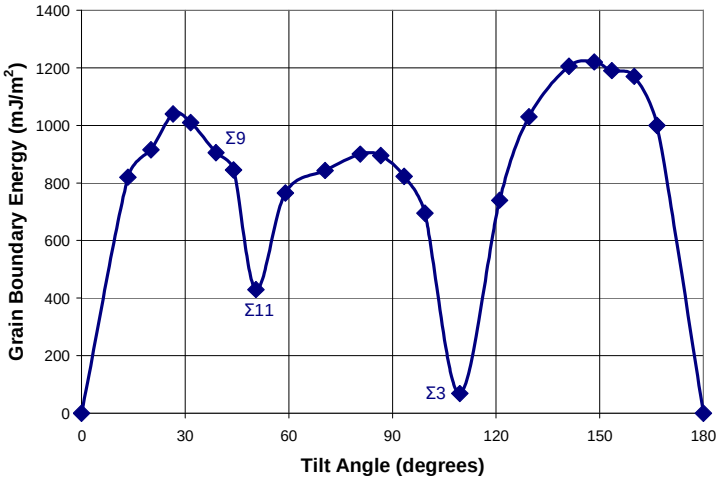

Figure 4.8. The grain boundary energy shown as a function of the tilt angle for nickel in the <110> direction.

Other types of GBs, specifically <111> twist and <001> tilt, were analyzed as shown in Figures 4.9-4.10, respectively. Each plot was mirrored about a line of symmetry corresponding to the boundary plane on the FCC lattice, which is 90˚ for each case. The minimum points in Figure 4.13 correspond to a 60˚ twist rotation about the <111> axis and a coherent twin (Σ3 GB), which is shown in Figure 4.3. Hence, we see that the same GB is characterized by a 109.47˚ tilt about the <110> axis and a 60˚ twist about the <111> axis. The local cusps in Figure 4.10 correspond to the Σ5 GB.

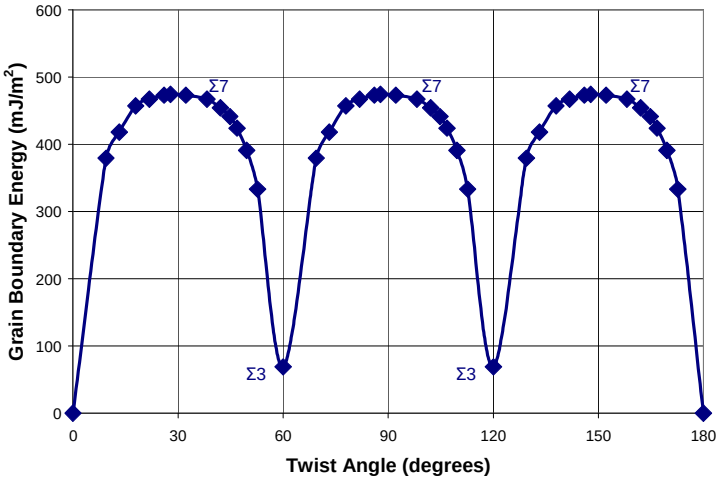

Figure 4.9. The grain boundary energy shown as a function of the twist angle for nickel in the <111> direction.

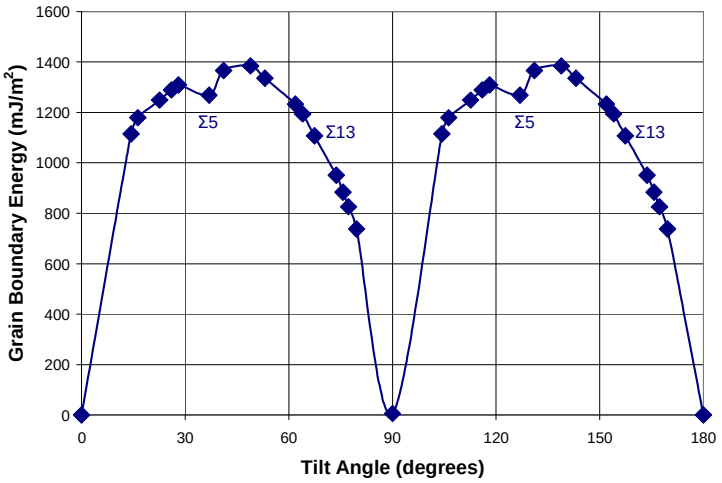

Figure 4.10. The grain boundary energy shown as a function of the tilt angle for nickel in the <001> direction.

The energies of the high-angle GBs are calculated through atomic simulations. The CSL configuration is well-suited for this investigation, since it can be fully described mathematically, is periodic, and, as a result, easily computationally implemented. However, the low-angle GBs cannot be fully characterized by a CSL, since they are not fully periodic. Hence, the energies of these boundaries are calculated by the Read-Shockley model, in which LAGBs are modeled as a series of dislocations and their resulting energies are calculated through linear elastic isotropic continuum theory [22]:

$$E = E_o\theta\left(A - \ln\theta\right), \tag{4.10}$$

$$\text{where } E_o = \frac{\mu b}{4\pi(1-\nu)} \text{ and } A = 1 + \ln\left(\frac{a_o}{2\pi r}\right).$$

In the Read-Shockley model, θ is the misorientation between grains in radians, μ is the shear modulus, υ is the Poisson ratio, $\boldsymbol{b}$ is the Burgers vector, a_o is the lattice spacing, and r is the cutoff radius of the dislocation core. This formula is valid for misorientations from 2˚ to 15˚ and compares well to the few MD results of CSL values for small misorientations about the <110>

tilt axis, as shown in Figure 4.11. Therefore, the energies are calculated from the Read-Shockley model for low-angle GBs and measured from MD for high-angle GBs. The next step in this analysis is to link these energies to the spatial EBSD scans for this material.

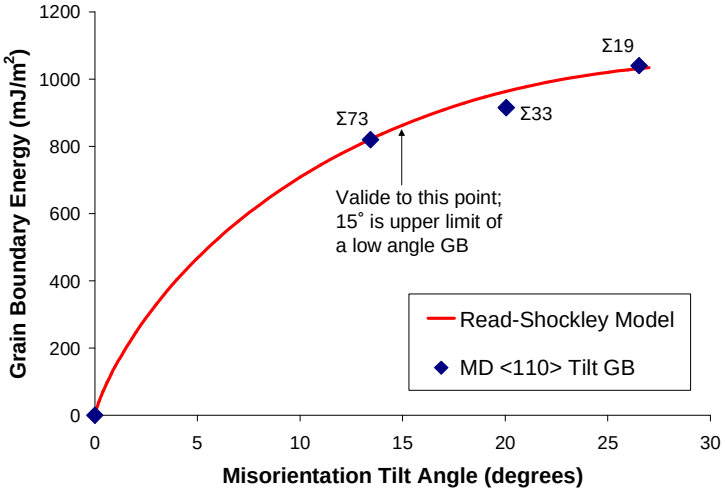

Figure 4.11. Comparison of GB energies from the Read-Shockley model (a continuum description of low-angle grain boundaries valid for misorientations from 2˚ to 15˚) and calculations from MD results of CSL values in and around that range.

4.4. Linking Characterization to Energetics

As previously discussed, to fully characterize a GB, we need a total of five degrees of freedom [48-60, 66, 67], although from the 2D EBSD scan and the axis-angle pair analysis, the GB normal is not available. This information can be obtained using serial sectioning of the test specimen [59, 60], although this method is a time consuming process in terms of data collection/interpretation and requires extensive equipment/software. In this procedure, we have calculated the axis-angle pair for each grain in the aggregate from an EBSD scan. Further, we have calculated the energies of the GBs via MD simulations and the Read-Shockley model, which we can use the Miller indices (*hkl*) description of the lattice to back-calculate the axis-

angle pair. Hence, through the axis-angle pair, we have a direct comparison to correlate the measured GB orientations of U720 from EBSD scans to the GB energy from MD simulations. We employ a simple assumption for the case of duplicate values of the axis-angle pairs, where the GB character is chosen based on the description of the GB containing the lowest energy value. During heat treatment of the material, the GB contains sufficient mobility to reorient itself into a low energy configuration. This assumption has validity as GB normals have been experimentally shown by Randle to reorient to lower energy configurations [50-52, 54] and in cases with sufficiently long heat treatments, the GBs are comprised of the lowest energy configurations [51]. Similarly, Rohrer et al. experimentally found that the GB plane is most frequently oriented such as to possess a low index plane with low surface energy [57]. Further, by MD simulations, Olmsted et al. showed that the coherent twin has the lowest GB energy and mobility, meanwhile GBs with higher energy also have higher mobility [66, 67]. Hence, GBs with higher energies have a higher mobility and driving force to reorient the GB normal into a lower energy configuration. Consequently, the 5 DOF description of a GB can be replaced by an axis-angle pair, reasonably well, where redundancies converge to the lowest energy configuration of the GB.

The grain boundary character developed through EBSD scans is linked to atomic simulations for high-angle grain boundaries to measure properties and behavior of the GB that cannot be obtained through experiments. Table 4.2 displays each of the 56 GB systems analyzed in this study, which is supplemented by a database with the energies of 388 GBs [66]. For low-angle grain boundaries, we employ the Read-Shockley model to calculate the energy [22]. Thus, the spatial map of the GB characters and grain size from EBSD scans are linked to the GB static relaxed energy from atomistic simulations. The GB energy is measured as a normalized value

(mJ/m^2). Each 2D scan of a grain is composed of multiple GB segments; the energies of each segment are summed and normalized by the number of GB segments as each grain may contain a different number of neighboring grains. The GB energy is seen to be inversely proportional to grain size (in terms of area) as shown for the low strain amplitude fatigue specimen in Figure 4.12. This EBSD scan contained 3,664 grains. In order to clearly graph this data, the GB energy has been binned and the grain area is averaged within each bin and the standard deviation for the bins is also shown. This procedure has been repeated for each of the 7 test specimens, and the same GB energy-grain area inverse correlation behavior was obtained for each specimen, as shown in Figure 4.13.

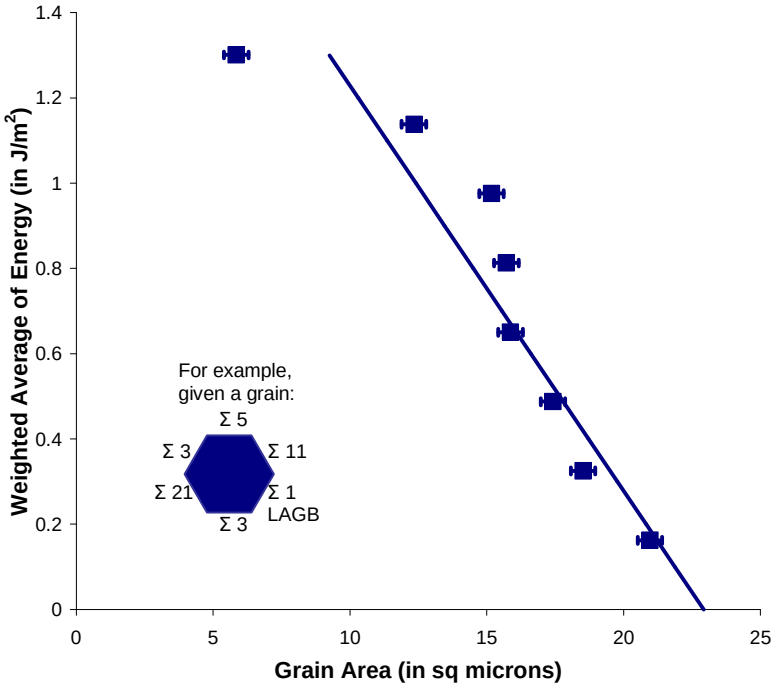

Figure 4.12. GB energy versus grain size (area) for a low strain amplitude fatigue specimen of U720 tested at elevated temperature. The graph is based on a scan containing 3,664 grains. The (normalized) GB energies obtained via MD are summed per grain and normalized by the number of GB segments per grain (refer to insert). These energies are plotted against the GB area, displaying an inverse correlation as shown by the best fit line through the data. For ease of plotting, the energies are binned and the grain areas are averaged.

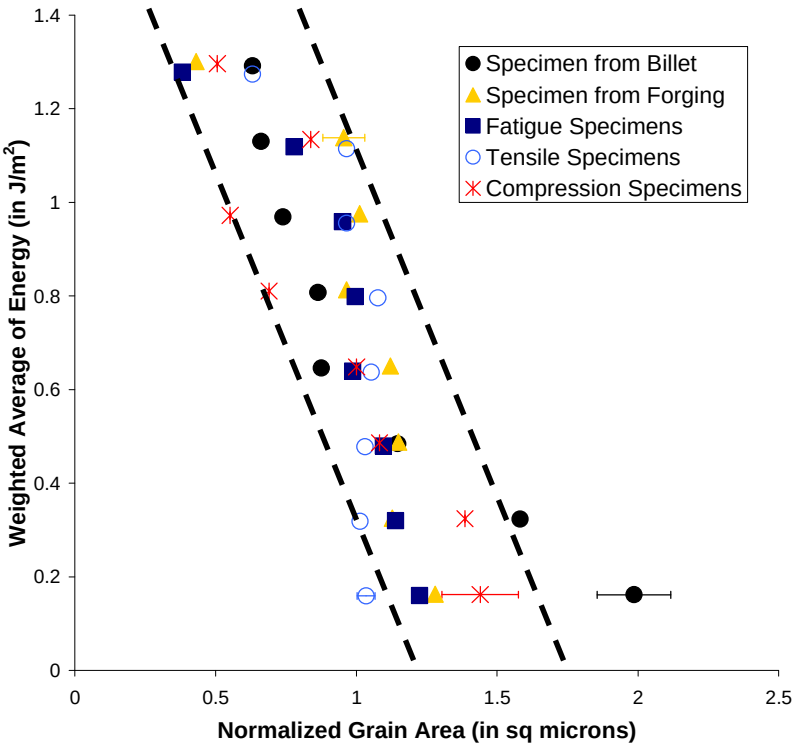

Figure 4.13. GB energy versus grain size (area) for seven specimens: 1 specimen from billet, 1 specimen from forging, 2 fatigue specimens, 2 tensile specimens, and 1 compression specimen. A total of 29,035 grains were analyzed in the EBSD scans across all 7 specimens. The same inverse correlation behavior between GB energy and grain size is shown in each specimen. In this figure, the dashed lines are drawn to guide the eyes.

The results of this analysis show that larger grains exhibit a smaller specific energy. We contend that the reasons are threefold. Twins are more prone to occur in larger grains as evident by a TEM analysis of this material. Thus due to the large amount of annealing twins present in large grains, the overall specific interface energy is lower for larger grains. Also, during heat treatment, larger grains have more mobility, thus they can orient themselves in favorable low-energy configurations, while smaller grains are merely pinned. In other words, large grains grow until they reach a low energy configuration. Finally, a small grain exhibits more curvature in the GB, which also contributes to a higher energy. Recently, Rohrer et al. established that an individual segment of a given boundary is prone to have a larger area when the GB character displays a lower energy value in Ni [58]. Our analysis emphasizes this relationship and extends

the correlation between length scale and energetics. For the first time, a link is made between the grain size and energies of the sum of its associated grain boundaries for a given grain. Every GB character for a given grain is examined and we establish an inverse relationship between the total interface energy and grain size.

4.5. Summary

This work has outlined considerable progress in characterizing grain boundaries in an engineering alloy and linking this information to grain size through the use of CSL distribution and GB energy. We have utilized a methodology to examine a GB as the entire region separating two grains and link it to a CSL description. The evolution of the CSL has been shown for various stages of processing (billet and forging) and deformation (tension, compression, and fatigue). Fatigue testing has little effect on the CSL distribution, although large deformation processes such as tension and compression lead to rotation and alignment of the grains and a greater population of LAGBs. In each of the specimens, the Σ3 GBs were prevalent, and it was shown that these represent coherent annealing twins.

The energies of the CSL GBs were measured using MD, while the Read-Shockley model was used to calculate LAGBs. The lowest energy configuration was observed for the coherent Σ3 twin GB, which explains its abundance in the measured EBSD analysis. A link was made between the calculated energies and the EBSD measurements of grain orientation and size. A strong inverse correlation exists between grain boundary energy and grain size for each specimen. The rationale behind this stems from larger grains exhibiting a greater twin density, more mobility to reorient the GB normal during heat treatment, and less GB curvature.

Chapter 5. Energy of Slip Nucleation and Transmission at GBs

5.1. Overview

In a polycrystalline material, there is a wide distribution of GB types with characteristic slip transmission and dislocation nucleation behaviors. There is a strong need to quantify the energy barriers of the individual GBs. In this chapter, we introduce a new methodology to calculate the energy barriers during slip-GB interaction, in concurrence with the generalized stacking fault energy curve for slip in a perfect FCC material. By doing so, we calculate the energy barriers to slip transmission at various classifications of GBs: <110> tilt – Σ3, 9, 11, 17, 19; <111> twist – Σ3, 7, 13, 21; and <001> tilt – Σ5. Similarly, the energy barriers to dislocation nucleation from these GBs are also determined. The character and structure of the GB plays an important role in impeding slip within the material. The coherent twin (Σ3) boundary provides the highest barrier for slip transmission. From this analysis, we show that there is a strong correlation between the energy barrier and interfacial boundary energy. GBs with lower static interfacial energy offer a stronger barrier against slip transmission and nucleation at the GB. The results have profound implications in understanding mechanical response (i.e. fatigue) influenced by the underlying grain boundary characters.

5.2. Simulation Methods

In this chapter, we build off of the atomistic simulations first introduced in Section 4.3.1. Specifically, we add forces to the static GB systems, in order to investigate the mechanical response of the GBs. For a dislocation to interact with a GB, it is necessary to have a single

controlled dislocation nucleating within the simulation and traveling towards the GB. This is accomplished by inserting a single spherical void within the simulation box below the GB, which acts as a stress concentrator to nucleate a dislocation and facilitate in slip-GB interaction. Care is taken to ensure that the strain field from the void does not interact with the strain field produced by the GB, thus the void is placed sufficiently far away from the GBs. After insertion of the void, the system is statically and dynamically relaxed using an *NPT* ensemble where the number of atoms in the simulation box, *N*, the pressure in the three directions (stress free boundaries), *P*, and the system temperature, *T* (10K), are held constant throughout the simulation.

In order to study the mechanical behavior of the GBs and measure their strengthening contribution via energy barriers to plastic flow, we must add forces and observe the kinetics of the GBs. Tension is applied in the simulation at a strain rate of 10^{10} s^{-1}, the high strain rates are indicative of MD. The atomic system is dynamically deformed with an NPT ensemble to a predetermined strain along the axis normal to the GBs, ***n***. During the simulation, the positions of the atoms, centro-symmetry parameter per atom [256], Virial stress, and energy per atom are measured and dumped per a time-step increment. Visual molecular dynamics (VMD) is used to visualize the simulation [257]. Also, the centro-symmetry parameter is utilized to locate and color the defects within the material based on its position with respect to its nearest neighbors (red indicates a partial dislocation, while gold denotes a stacking fault). For clarity, defect-free atoms that do not participate in the interaction are deleted from the MD simulation snapshots.

5.3. Energy Barrier Results

As previously mentioned in Chapter 4, the energy, E_{Static}^{GB}, of CSL grain boundaries was measured by relaxing the system. The simulation was repeated for various rotations about the

<110> tilt, <111> twist, and <001> axes, and the results are summarized in Figure 5.1, since they are useful to comprehend the GB energy barriers.

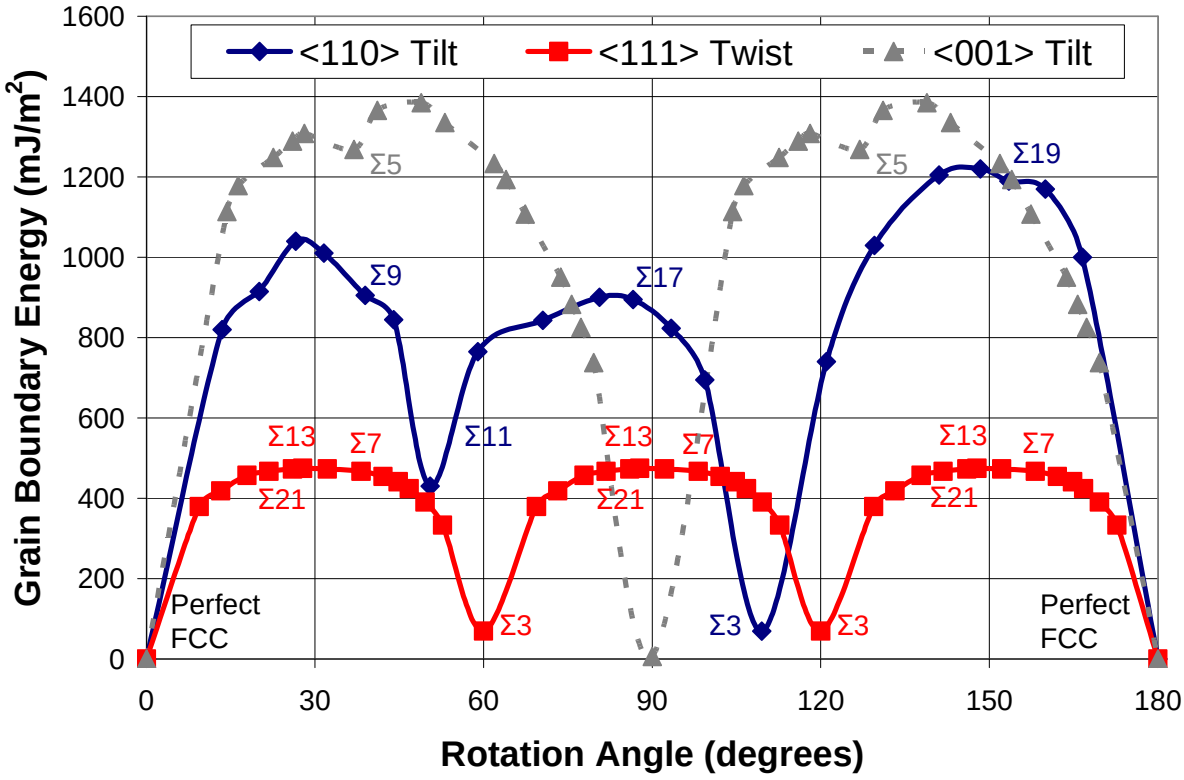

Figure 5.1. The grain boundary energy shown as a function of the rotation angle for nickel in the <110> tilt, <111> twist, and <001> tilt directions.

As aforementioned, the strengthening behavior of each GB was observed by deforming the simulation box. This resulted in a partial dislocation nucleating from the void and traveling along a $\{111\}$ plane until it reached the GB. In each case the GB acts as a barrier to impede dislocation motion. An example of such a reaction is shown for the case of a coherent twin or Σ3 GB in Figure 5.2a. For this case, the system is loaded in the [111] orientation and the incident dislocation is comprised entirely of an edge component, hence the dislocation reaction is two-dimensional and chosen for clarity. The trailing partial is pinned at the source resulting in a stacking fault in the wake of the dislocation. The Schmid factor of the coherent twin boundary is

zero. As shown by the reaction in Figure 5.2b, the high stability and coherency of the twin boundary forces the dislocation to transmit the GB on a non-Schmid, cubic $\{100\}$ plane, thus nucleating a Lomer type dislocation which glides in the adjacent grain. In this case, there is no resolved shear stress on the GB and the system is loaded uniaxial in the [111] direction, thus no other glissile slip systems are available leading to cubic slip penetration. This phenomenon has been observed by others in experiments (at room temperature of low stacking fault FCC alloys) [258, 259] and MD simulations [108, 260]. Although with the presence of a resolved shear stress at the GB, slip transmission occurs on a glide plane [260].

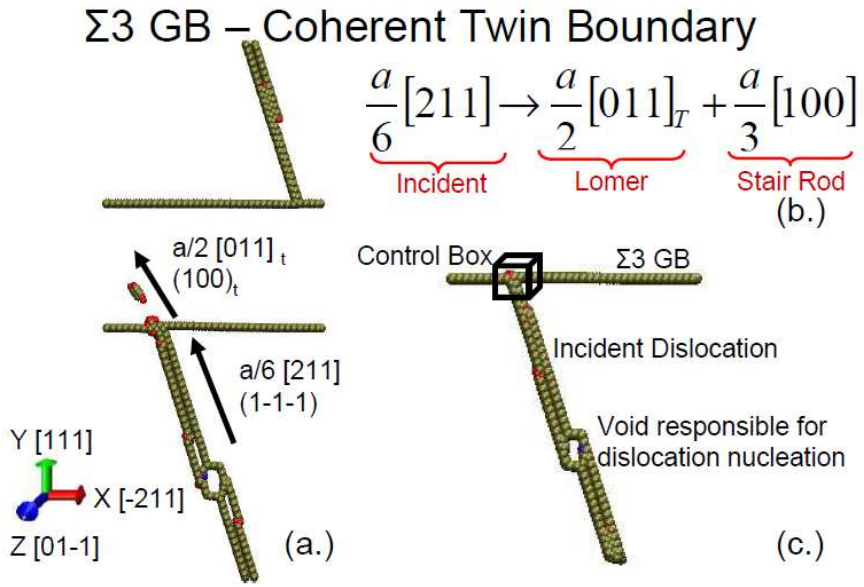

Figure 5.2. (a.) Dislocation - Σ3 GB (coherent twin) interaction and (b.) the resulting dislocation reaction. Please note that for clarity, only the atoms representing defects are shown. In this system, a void is introduced to facilitate dislocation nucleation. (c.) Schematic of a control box surrounding the atoms involved in the slip - Σ3 GB interaction.

To grasp the role of the GBs on the energetics of each system, a contour plot was created of the potential energy of each atom during the slip-GB interaction. The potential energy is governed by the spatial packing of the crystal; hence the introduction of defects and slip-GB interactions affects their position and potential energy. A cross-sectional view of the contour

energy plot for an incident dislocation interacting with a Σ3 GB is shown in Figure 5.3, which corresponds to the same reaction observed in Figure 5.2. It can be seen that the atoms around the void have higher energy due to a deficient number of nearest neighbors. Upon loading, a dislocation nucleates from the void, which is discernible by a heterogeneous rise in energy. The leading partial dislocation propagates towards the GB resulting in a stacking fault. During interaction, the dislocation is impeded as the energy in the vicinity of the interaction increases until it is sufficiently large to allow the dislocation to transmit to the adjacent grain. In this case, it corresponds to nucleation of a Lomer dislocation at the interaction site. Local variations in the energy are small and nearly insignificant. It is possible to calculate the energy barrier for dislocation-GB interaction by viewing a control box around the interaction, as shown in Figure 5.2c.

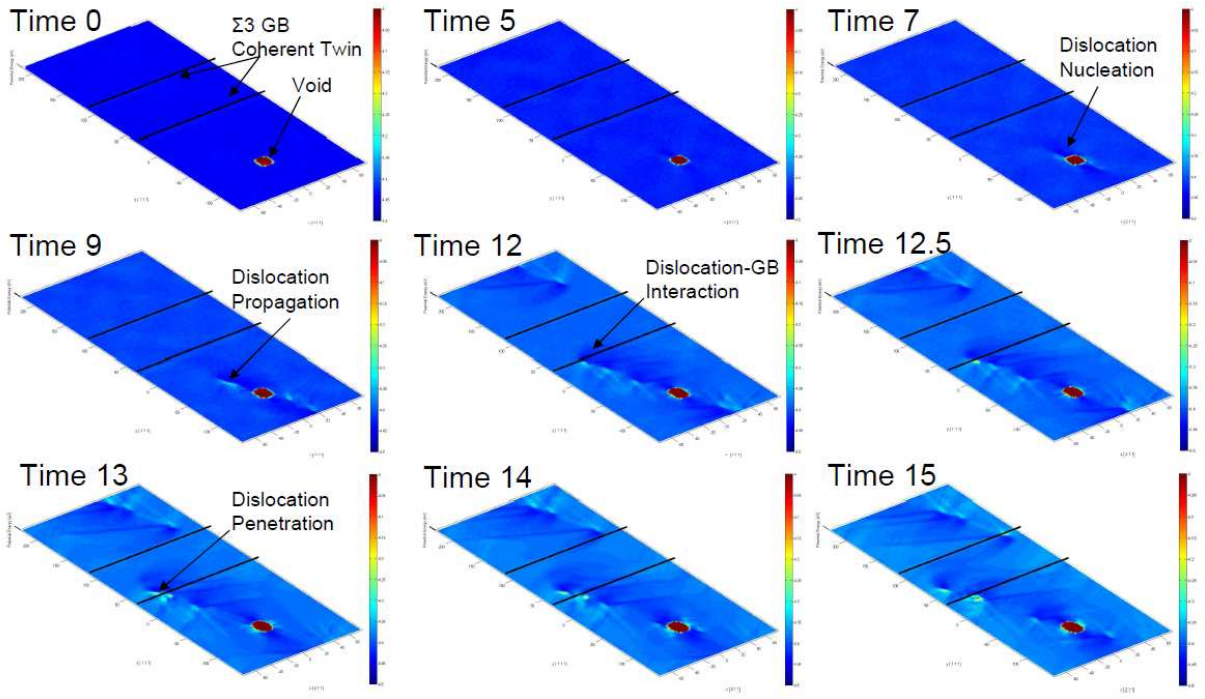

Figure 5.3. Cross-sectional view of a contour plot of the energy for the reaction shown in Figure 5.2 for various simulated time-steps.

To date, the vast majority of MD studies provide qualitative behavior into the mechanics of materials. Our goal is quantitatively understand the atomistics of GBs using MD. So, a control box is placed at the intersection of the dislocation and GB. In each case, the control box is only placed along the atoms which play a role in the interaction; hence it is not a simple cubic box. This process consists of writing codes to view the simulation using VMD of the defects identified by the centro-symmetry parameter. Extreme care is taken to select the positions of only the relevant defect atoms then running a Matlab algorithm that selects these atoms and measures their energy:

$$E_{Barrier} = \frac{\sum_{i}^{n} E_{load}^{i} - E_{static}}{volume}, \tag{5.1}$$

where for each atom *i* within the control box, the energy upon loading of that atom, E_{load}^{i}, is reduced by the energy of that atom in its static relaxed position, E_{static}, and normalized by the *volume* of the control box. The result of Equation 5.1 produces the energy barrier for slip-GB interaction in units of mJ/m^3. This process is dependent on the size of the control box, hence only the atoms contributing to the reaction must be included and monitored. Further, for the cases of a residual dislocation incorporated within the grain boundary plane, the control box must also include the spreading and dissociation of the dislocation within the boundary.

In order to verify our new method for determining the energy barrier, a system was constructed without a GB. In this case, the dislocation nucleated from the void and the control box measured the lattice resistance to slip in a perfect FCC crystal. For such a case, the energy was measured according to Equation 5.1 and multiplied by the slip length within the control box, ζ, to obtain the energy barrier in terms of fault energy per unit area. The result of which was compared to the generalized stacking fault energy (GSFE) calculated from molecular statics, ab

initio calculations [254], and experiments, as shown in Figure 5.4. There was only a 6% difference between the MD control box method and the relaxed GSFE curve, thus validating our method. In these simulations, a trailing partial was not produced; hence the second barrier of the control box curve is represented by a dashed line.

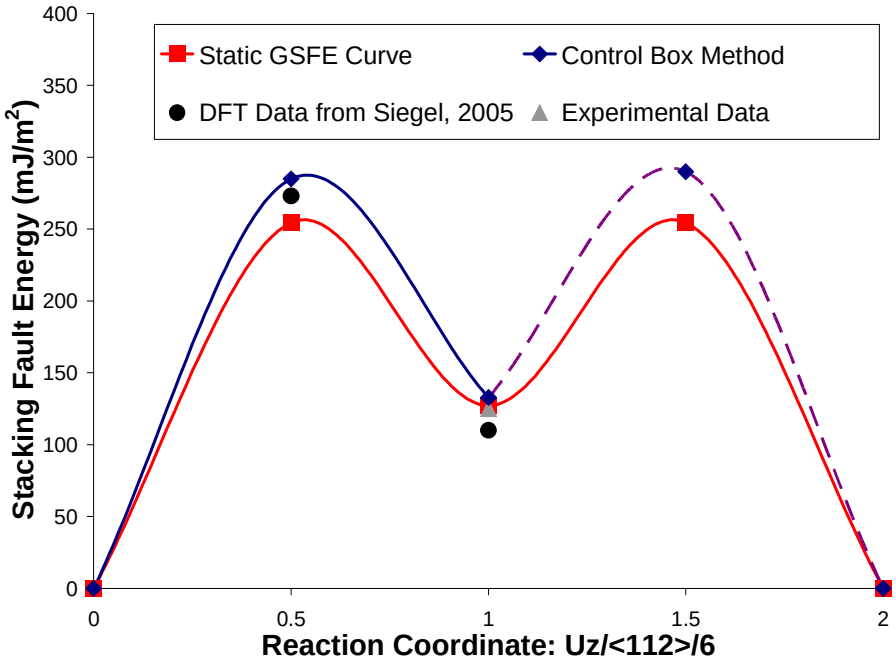

Figure 5.4. Verification of the method for measuring the energy barrier for slip in a perfect FCC material by placing a control box around a set of atoms and measuring the energetics during a molecular dynamics simulation. This is compared to values from experiments, density functional theory [254], and the molecular statics response, where the atoms are allowed to fully relax. The dynamic calculation is less than 6% different than the static curve.

The slip-GB reactions were observed for various types of GBs: <110> tilt – Σ3, 9, 11, 17, and 19; <111> twist – Σ3, 7, 13, and 21; <001> tilt – Σ5; and perfect FCC material. In each reaction, the incident leading partial dislocation glides along a $\{111\}$ plane and interacts with the GB as shown in Figures 5.5a-c for Σ3, Σ7, and Σ11 GBs, respectively. As shown in Figure 5.5b,c, typically the incident dislocation is a loop containing mixed screw and edge components. After interaction with the GB, a partial is transmitted into the adjacent grain on a glissile Schmid $\{111\}$ plane. Slip-Σ5 GB interaction results in a residual dislocation absorbed in the boundary

plane as shown in Figure 5.5c by the red loop within the GB, indicating a partial dislocation. The resulting energy barriers for slip to penetrate the GBs are shown in Figures 5.5d-f for Σ3, Σ7, and Σ11 GBs, respectively. In each case, local fluctuations in energy are observed as the system is loaded corresponding to vibrations of the atoms via a temperature thermostat. These fluctuations are small compared to the energy barriers. Also, prior to interaction, the elastic strain energy of the material is removed from the energy barrier plots. The systems are loaded to a predetermined strain, meanwhile the energy plots are linked to the visualization of the system, which indicate dislocation nucleation from the source and dislocation interaction with the GB. In each simulation, the dislocation nucleates at various applied strains due to the differences in the loading axis. After the dislocation interacts with the GB, the energy significantly rises to a maximum value and decreases after slip is transmitted into the adjacent grain. This value is taken as the energy barrier for slip transmission across a GB. It can be seen that the coherent twin boundary (Σ3 GB) provides a greater energy barrier to slip than the Σ7 and Σ11 GBs.

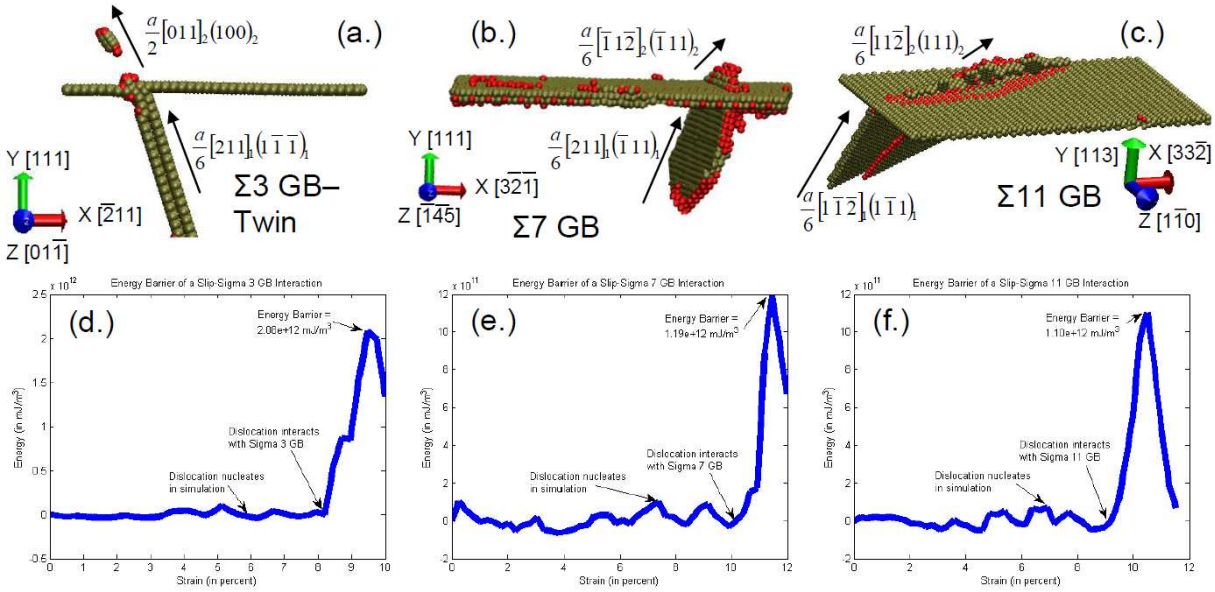

Figure 5.5. Interactions of dislocations with (a.) Σ3 GB (coherent twin), (b.) Σ7 GB, and (c.) Σ11 GB with the resulting dislocation reactions; and the corresponding energy barrier calculations for slip to penetrate the (d.) Σ3 GB (coherent twin), (e.) Σ7 GB, and (f.) Σ11 GB.

By removing the void and placing the control box along the entire GB, we can also measure the energy barrier for dislocation nucleation from a GB. This process was repeated for the same types of GBs as previously mentioned: <110> tilt – Σ3, 9, 11, 17, and 19; <111> twist – Σ3, 7, 13, and 21; <001> tilt – Σ5; and perfect FCC material. From this analysis, the dislocation emission from Σ5, Σ9, and Σ19 GBs is shown in Figures 5.6a-c, respectively. In each case, to satisfy compatibility of the system during the applied deformation, dislocations are nucleated from the GBs on a glissile Schmid $\{111\}$ plane. A single dislocation loop of mixed edge and screw components representing a leading partial is emitted for the Σ5 and Σ9 GBs, as shown in Figure 5.6a,b. For the case of nucleation from a Σ19 GB, the dislocations are emitted in a homogeneous manner as the intrinsic stacking fault facets extend from the GB. The dissociation of the GB corresponds to the structural units that comprise the static GB, which is in agreement with the literature [92].

The corresponding energy barriers to dislocation emission for the previous cases, Σ5, Σ9, and Σ19 GBs, are shown in Figures 5.6d-f, respectively. In each case, the energy of the atoms within the control box, i.e. the GB interface region, increases until nucleation of the first dislocation. At this point, the system can relax around the dislocation and the energy decreases. The result is the energy barrier for dislocation emission. These plots include the strain energy density as this contributes to dislocation nucleation. From the examples shown, the Σ9 GB offers the highest barrier to dislocation nucleation, while the Σ19 GB has the lowest energy barrier. For the cases of a dislocation nucleating from Σ3 GB, Σ11 GB, and perfect FCC material, these systems have a simple dislocation structure and stable configurations. Hence, in these simulations, dislocations are emitted in the matrix material preventing a measurement of the energy barriers for nucleation.

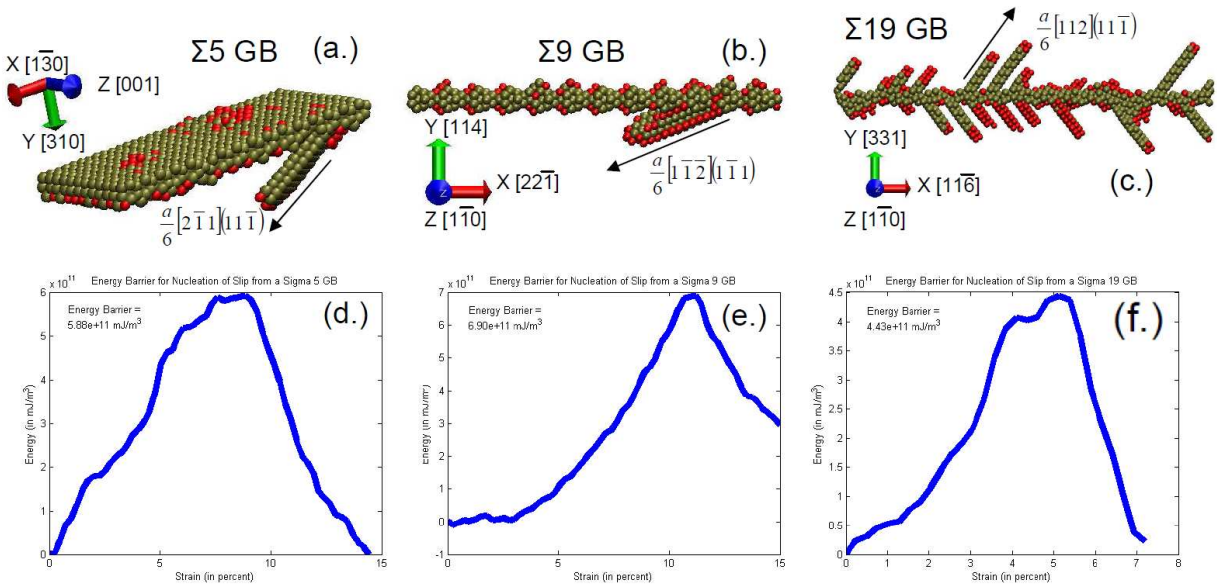

Figure 5.6. Nucleation of dislocations from (a.) Σ5 GB, (b.) Σ9 GB, and (c.) Σ19 GB with the direction and plane of the emitted dislocation; and the corresponding energy barrier calculations for dislocations to nucleate from the (d.) Σ5 GB, (e.) Σ9 GB, and (f.) Σ19 GB.

5.4. Discussion

To our knowledge, this study represents the first time the energy barriers for slip to penetrate a GB (Figure 5.5) or slip to nucleate from a GB (Figure 5.6) are measured from a control box of atoms pertinent to the interaction. This process is repeated for relevant GBs and the energy barrier results for slip interaction and slip penetration are calculated.

5.4.1. Slip Transmission through GBs

We rationalized the energy barriers for various types of GB with their static GB energy. The results of which are shown in Figure 5.7 as the energy barrier for slip transmission across a GB is plotted against the static GB energy for each GB. As expected, the perfect FCC material does not provide a strong barrier against slip, as this represents a perfect crystal and thus only lattice resistance to flow. For each type of GB, there is an inverse relationship between the

energy barrier against slip and static energy for each GB. A power law function was fit to the data resulting in the following:

$$E_{Barrier}^{Transmission} = 2.8\times10^{13} \cdot \left(E_{Static}^{GB}\right)^{-0.6}, \tag{5.2}$$

where the static GB energy, E_{Static}^{GB} (units of mJ/m^2), and the GB energy barrier to slip transmission, $E_{Barrier}^{Transmission}$ (units of mJ/m^3), are the same quantities measured in Equations 4.9 and 5.1, respectively. This relation is only valid for GBs in the range of the simulation data. The coherent twin boundary – Σ3 GB offers the lowest interface energy and highest barrier to slip, thus providing a significant strengthening contribution (although if additional defects are added to the Σ3 GB, the energy barrier decreases). As previously viewed (Figure 5.2), the Σ3 GB transmits a Lomer dislocation in the cube plane within the adjacent grain. Since this is not a closed packed plane, the energy barrier for slip along this plane is significantly higher.

Lee, Robertson, and Birnbaum proposed three criteria for strain incompatibility across a GB [71]. The first is a geometrical condition for predicting the active slip plane by minimizing the angle between the slip directions and line of intersection of the slip planes to the GB. The second part of the criterion determines the slip direction based on the maximum resolved shear stress on the active slip plane. The third condition requires a Burgers vector of the residual dislocation (difference in $\boldsymbol{b}$ of incoming and outgoing dislocation) to be minimized. In each slip-GB reaction investigated in this study, the results agreed with these criteria. The geometric condition is satisfied as the angle is minimized, for the case of the (111) twist GBs the angle is zero. The critical resolved shear stress condition is also satisfied, even for the case of cube transmission past the coherent (Σ3) twin boundary. Burgers vector analysis [260] of the simulation results reveal that the residual dislocations are in the form of either a stair rod or Frank dislocation and are minimized in all cases.

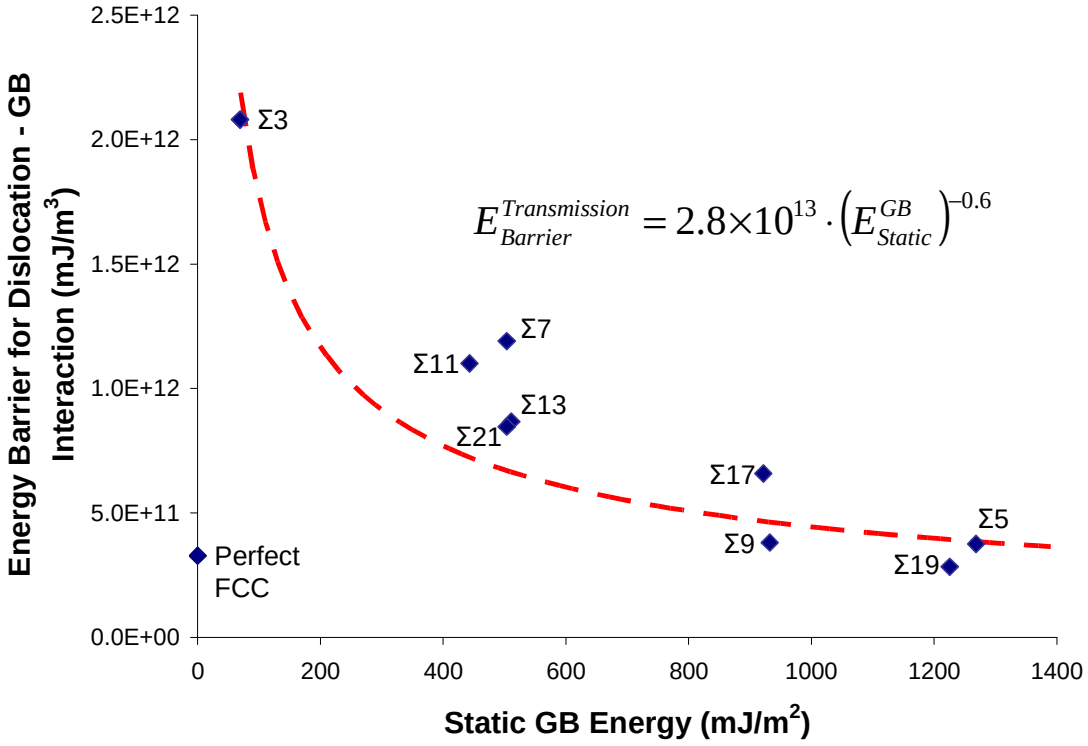

Figure 5.7. Energy barriers for slip to penetrate a GB plotted against the static GB energy for various types of CSL GBs. There is a relationship between the static GB energy and GB energy barrier to slip as shown by the power law fit of the data.

5.4.2. Slip Emission from GBs

Similarly, the energy barrier for slip nucleation from a GB is plotted against each GB's static energy, as shown in Figure 5.8. Once again, there is an inverse relationship between the static GB energy, E_{Static}^{GB} (Equation 4.9 – units of mJ/m^2), and the GB energy barrier to slip nucleation, $E_{Barrier}^{Nucleation}$ (Equation 5.1 – units of mJ/m^3), as shown by the power law fit:

$$E_{Barrier}^{Nucleation} = 6.0\times10^{15} \cdot \left(E_{Static}^{GB}\right)^{-1.3}. \quad (5.3)$$

As previously mentioned, due to the stability of the GBs, the energy barrier for dislocation nucleation could not be measured for GBs with low interfacial energy, as indicated in Figure 5.8 with the gray vertical line. Due to their stability, in the simulation, dislocations nucleated within

the matrix material as opposed to the Σ3 and Σ11 GBs. Hence, the above relationship is only valid to the right of the gray vertical line in the range of the simulation data.

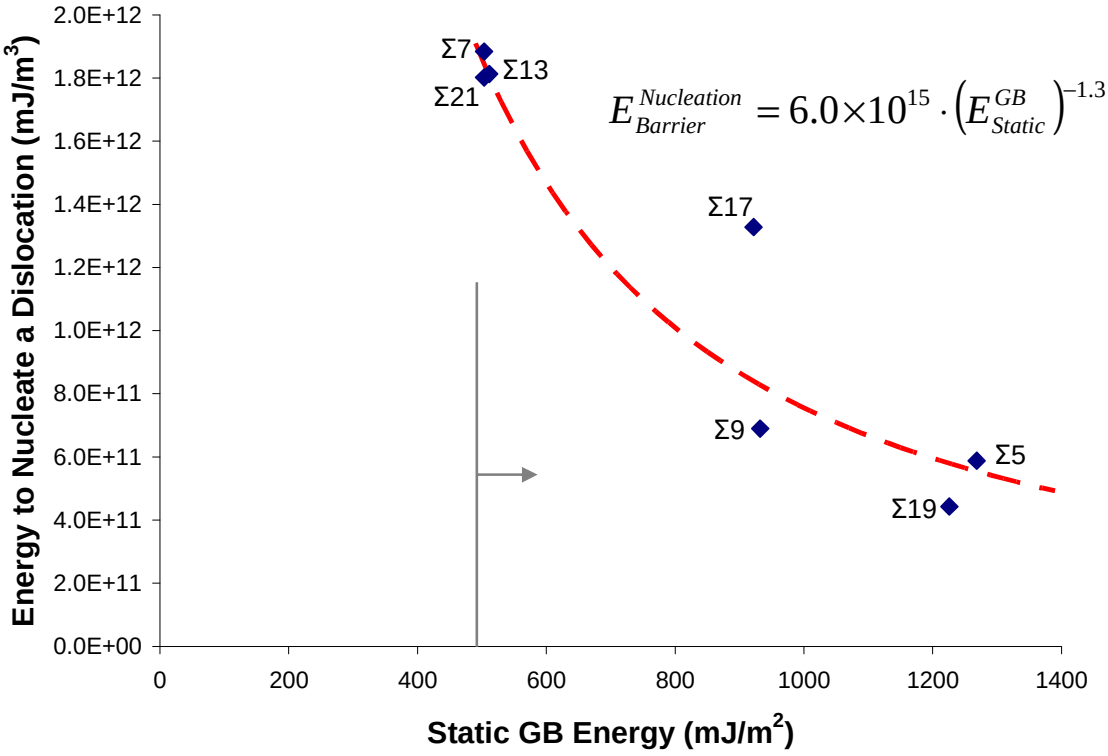

Figure 5.8. Energy barriers for slip to nucleate from a GB plotted against the static GB energy. There is a relationship between the static GB energy and GB energy barrier to dislocation nucleation as shown by the power law fit of the data. To the left of the gray solid line, the energy barriers cannot be measured, since the Σ1 (perfect FCC), Σ3 (coherent twin), and Σ11 GBs have a simple dislocation structure and stable configurations. Hence dislocations were nucleated in the matrix material during the simulation, preventing the energy barrier calculations.

Based on the results of this investigation, the slip-GB interaction is strongly dependent on the geometry of the bicrystal system, applied loading orientation, Schmid factor of the interface, and GB structure. The applied loading and Schmid factor play an important role in the kinetics of the dislocation behavior. The geometry and GB structure determine the static GB energy according to the structural units of the defects at the interface [42-45, 65]. This plays an important role in the transmission and nucleation processes. As it can be seen in Figure 5.6c, a GB with a dissociated structure results in growth of the intrinsic stacking faults during loading.

From afar, this can be viewed as nearly homogeneous nucleation. As a consequence, the energy barrier for nucleation and transmission from a GB exhibiting a dissociated structure is significantly lower. This is in direct opposition of the simple defect structure, i.e. Σ3 and Σ11 GBs, which have a low static GB energy and offer a substantial barrier to dislocation transmission. From these measurements of the energy barriers, we can draw a quantitative description of each GB's impact on the strengthening behavior of a material, thus providing a powerful contribution to the kinetics of slip. These energy barriers have direct implications to the field of material modeling, specifically crystal plasticity, fatigue, fracture, and creep, since we can more accurately interpret the role of each GB on the impedance of deformation. In the subsequent chapters, we use these energy barriers to service a model for prediction of fatigue crack initiation.

5.5. Summary

Molecular dynamics simulations are used to study the slip-GB interactions including strain transmission and dislocation nucleation at a GB. The aim of this work is to quantify the strengthening mechanisms of individual GBs. Significant contributions of this study are summarized as follows:

1. A new methodology is introduced to measure energy barriers based on placing a control box around the pertinent defect atoms. By tracking the atom position and their corresponding energies, during the interaction, it is possible to obtain the energy barrier for slip transmission or nucleation at a GB. This methodology is validated by comparing the energy barrier of slip in a perfect FCC material to the generalized stacking fault energy curve; the results displayed a modest 6% difference.

2. The energy barriers to slip transmission are calculated across various classifications of GBs: <110> tilt – Σ3, 9, 11, 17, 19; <111> twist – Σ3, 7, 13, 21; and <001> tilt – Σ5. Each reaction is in agreement with the Lee, Robertson, Birnbaum criterion for strain incompatibility. The coherent twin (Σ3) boundary provides the highest barrier for slip transmission.
3. The energy barriers to dislocation nucleation from the aforementioned GBs are calculated. The Σ3 and Σ11 GBs have a stable configuration, hence nucleation from the GB is not observed in the simulation. Upon loading of GBs with dissociated structures, the intrinsic stacking fault regions extended in a periodic manner across the interface. Hence, the nucleation event was nearly homogeneous resulting in a lower energy barrier.
4. The energy barrier from the slip-GB interaction is significantly affected by the character and the structure of the GB, as there is a strong correlation between the energy barrier and interfacial boundary energy. GBs with lower static interfacial energy offer a stronger barrier against slip transmission and nucleation at the GB.

Chapter 6. Fatigue Model – PSB Energy

6.1. Overview

In many engineering applications, fatigue is the dominant failure mechanism that governs the life of a component. Thus, many studies have focused on this phenomenon, although there is a need for a model that addresses fatigue based on the material's microstructure, specifically the energetics of the grain boundaries (GBs) and persistent slip bands (PSBs). Our approach is to model the energy of a PSB structure and use its stability with respect to dislocation motion as our failure criterion for fatigue crack initiation. The components that contribute to the energy of the PSB are identified, namely, the stress field resulting from the applied external forces, dislocation pile-ups, and work-hardening of the material is calculated at the continuum scale. Further, energies for dislocations creating slip in the matrix/precipitates, interacting with the GBs, and nucleating/agglomerating within the PSB are computed via molecular dynamics. The results of our simulations on the stability of a PSB produce the correct fatigue crack initiation trends for the grain size, grain orientation, character of the GB, precipitate volume fraction, and applied strain. From this information, we see that distinct GBs act as strong barriers to slip and increase the fatigue strength of the material.

6.2. PSB Energy Model

Our approach is to model the energy of a persistent slip band structure, E, and use its stability with respect to dislocation motion as our failure criterion for fatigue crack initiation. The concept of an energy balance and stability of a dislocation structure within a material is not new; it has a long standing historical basis [110, 181-186, 255, 261-263]. Also, this approach

allows us to address the small-length scale problems via incorporation of atomistic simulations. Hence, the atomic simulations provide important insights into the energy barriers and physics of the grain boundaries, which are crucial to fatigue of a polycrystalline material. All the contributing energy factors to the PSB are addressed and our energy balance is as follows:

$$E = -E^{\sigma}_{app}(\sigma, m, h, L, N) - E_{hard}(\rho, h, L, N) + E^{disl}_{pile-up}(h, d, L, N) + E^{disl}_{nuc}(m, \rho, \Sigma, h, L, L', N) + E^{PSB-GB}_{\text{int}\,eraction}(m, \Sigma, h, L, L', N) + E^{PSB-GB}_{LAGB}(m, \Sigma, h, L, L', N) + E_{APB}(h, L, \gamma'_{dist}, N) + E_{\gamma-SF}(h, L, \gamma'_{dist}, N) \quad (6.1)$$

where σ is the applied stress during fatigue loading, N is the number of cycles, m is the Schmid factor of the grain containing the PSB, L is the grain size, L' is the grain size of neighboring grains, h is the height of the PSB, d is the mean dislocation spacing within the PSB, ρ is the dislocation density within the PSB, Σ is the character of GB in the CSL, and γ' is the distribution of Ni_3Al-type precipitates. The first three terms of the energy expression displays terms that are associated with the continuum length scale, and other terms are derived by atomic simulations. Each term is discussed in the subsequent sections.

The geometry of the PSB within the most favorably oriented grain of a polycrystal is shown in Figure 6.1a. From which, it can be seen that the dislocations localize into the PSB and form wall structures. The PSB intersects the GB; as a consequence of slip within the PSB, extrusions are formed across the GB. Extrusions were originally defined for slip emanating at surfaces; however, PSB impingement at grain boundaries can also constitute crack initiation [119, 169-178]. In this case, as Mughrabi et al. has shown [151] (Figure 6.1b), interactions between PSBs and GBs in polycrystals result in a static extrusion resulting in ledges/steps thus roughening the GB. The number of dislocations within the extrusion is given by $n^{pen}_{dis}\vec{b}h$, where n^{pen}_{dis} is the number of dislocations that penetrate the GB on a single slip plane and $\boldsymbol{b}$ is the Burgers vector.

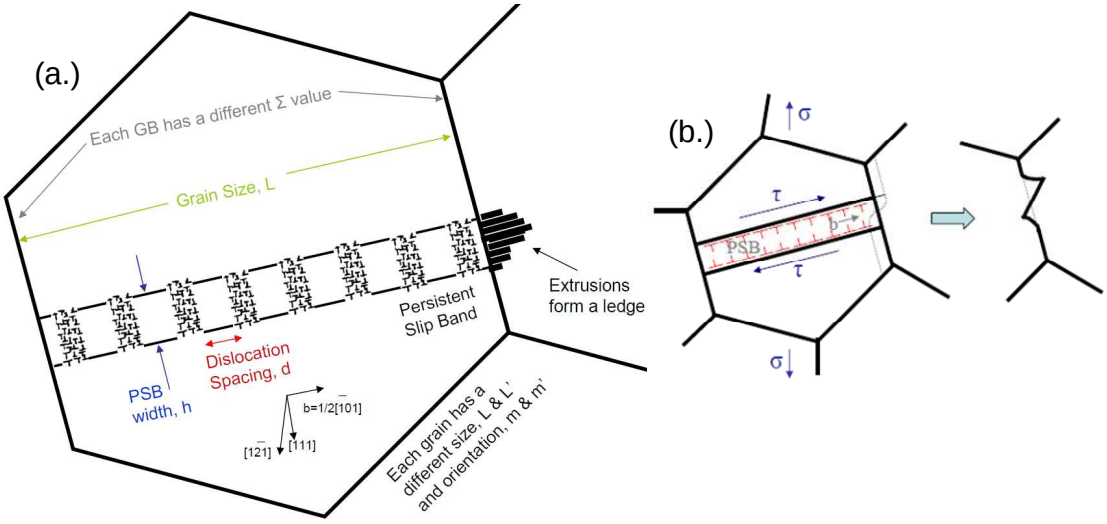

Figure 6.1. (a.) Schematic of the PSB geometry (*h*, *d*) in the polycrystal. The PSB forms across a grain of size *L* and orientation (Schmid factor, *m*) and intersects a pair of GBs each with an associated Σ value. (b.) Extrusions form across the GB. Although extrusions were originally defined due to PSBs emanating slip at a free surface, PSB interactions with GBs leads to static extrusions across the GB in the form of ledges and steps, redrawn from Reference [151].

6.2.1. Continuum Terms

The continuum terms (first three terms in Equation 6.1) create an internal stress field, in which the glissile dislocations must overcome this stress field to plastically deform the material [214] by an increment of slip, ∂X, as follows:

$$E_\tau = \bar{\tau}\vec{b}Ln^{layers}\partial X \tag{6.2}$$

where the overall shear stress, $\bar{\tau}$, is composed of the dislocation field in the PSB structure, τ^{dis}, the work-hardening of the system, τ^h, and the external applied resolved shear stress, τ^A.

$$\bar{\tau} = \tau^{dis} - \tau^h - \tau^A \tag{6.3}$$

It is paramount to account for each layer of successive dislocations that are gliding within the PSB. The number of moving planes within the PSB is quantified by n^{layers}, which is related to the PSB width, *h*.

$$n^{layers} = h / y^e \tag{6.4}$$

The width of the PSB, *h*, was measured from the TEM images of U720 (e.g. Figure 6.2). This quantity was seen to increase according to a square root function with increasing number of cycles [151] and saturate. The width of the PSB must be normalized by the distance between dislocations within the PSB to find the number of layers; in order to do so, the annihilation distance, y^e, of edge dislocations within a PSB is used. This quantity was originally calculated by Essmann and Mughrabi [141], who theorized that during saturation of the PSB, the dislocations approach this annihilation distance. The individual stress components that contribute to the internal stress field are discussed next.

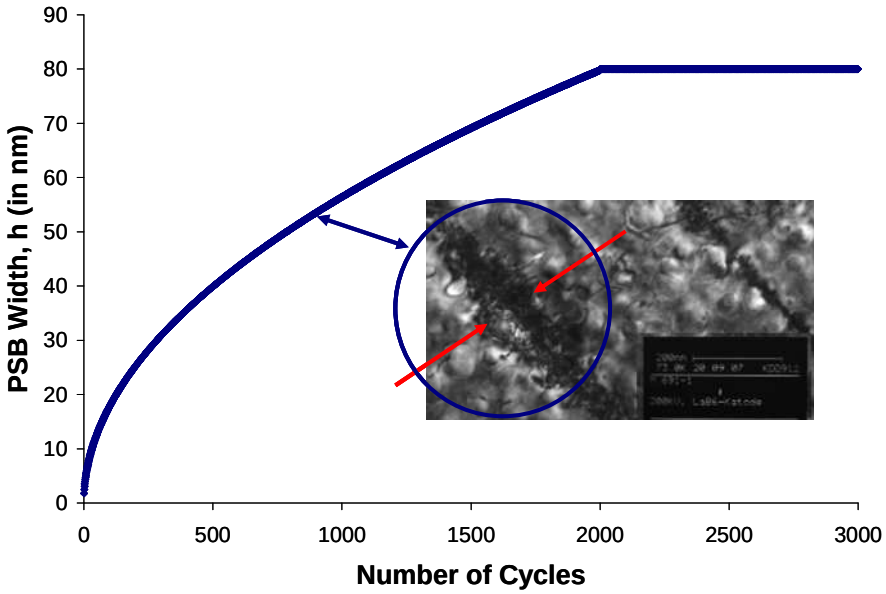

Figure 6.2. PSB width evolution during cyclic loading. The saturation is measured from TEM analysis.

6.2.1.1. Dislocation Pile-up

Within the PSB, dislocations agglomerate and form dipole structures, in order to minimize their total energy, as shown in Figure 6.1a. The dipole structure within the PSB can be modeled as layers of opposing signed dislocations [148, 180, 181] separated by a distance, *h*. Within each layer is a series of dislocations, equally spaced by *d*. In doing so, we can assume

linear elastic, isotropic, plane strain behavior thus greatly simplifying the problem, in order to find the stress within the PSB. The stress field created by the dislocation dipoles within the PSB is given by τ^{dis} as it varies spatially (x,y) within the PSB [165]:

$$\tau^{dis} = \frac{\mu b \pi}{(1-\nu)d^2}\left(\frac{y\left(1-\cos\left(\frac{2\pi x}{d}\right)\cosh\left(\frac{2\pi y}{d}\right)\right)}{\left(-\cos\left(\frac{2\pi x}{d}\right)+\cosh\left(\frac{2\pi y}{d}\right)\right)^2} - \frac{(h+y)\left(1-\cos\left(\frac{2\pi x}{d}\right)\cosh\left(\frac{2\pi(h+y)}{d}\right)\right)}{\left(-\cos\left(\frac{2\pi x}{d}\right)+\cosh\left(\frac{2\pi(h+y)}{d}\right)\right)^2}\right), \quad (6.5)$$

where the elastic constants μ, ν are the shear modulus and Poisson ratio at elevated temperatures, respectively. The resulting contour plot of the stress field due to dislocation pile-ups within the PSB is shown in Figure 6.3. The mean dislocation spacing, d, is determined based on the dislocation density within the PSB, ρ, as follows:

$$d = \frac{1}{\sqrt{\rho}}. \quad (6.6)$$

In Equation 6.5, the dislocation pile-up stress is given as a function of spatial position. It is of particular interest to understand which value is pertinent to our study. In previous models, Mura et al. [181-186] and Brinckmann [165] described failure for a PSB as a crack breaking apart the material in the middle of two opposing dislocation series, although this approaches the material's cohesive strength and refers to a more brittle mode of fracture. Another theory is the existence of a significant gradient in the strain field at the junction between the relatively soft matrix and a heavily work-hardened PSB resulting in crack initiation at this junction [135-139]. From the latter theory, the stresses near the top and bottom of the slip band are most significant to our model and are plotted in Figure 6.3.

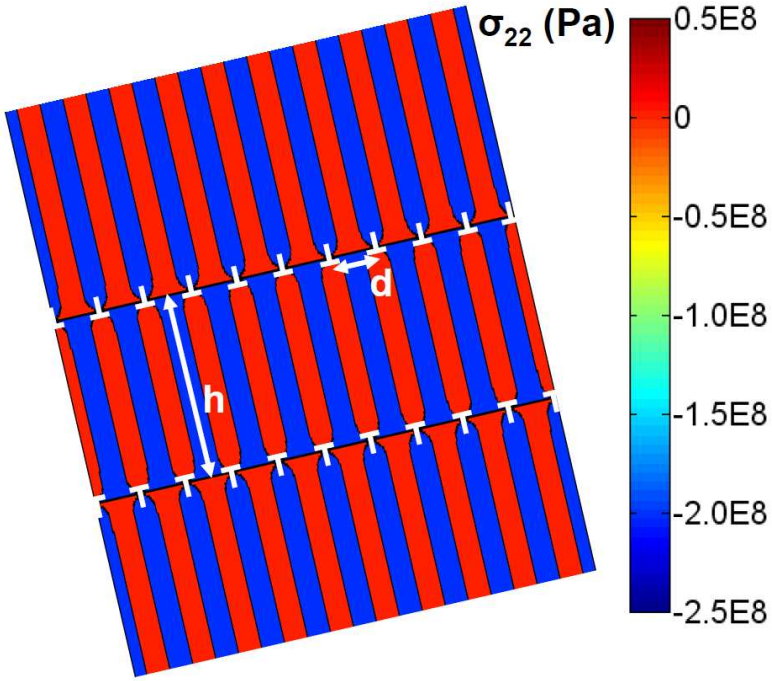

Figure 6.3. Contour plot of the stress field in a PSB (height *h*) from the dislocation dipole walls (separated by a distance *d*, as shown in the schematic in Figure 6.2). The PSB is modeled as two alternate layers of edge dislocations separated by *h* containing a series of dislocations with spacing *d*.

6.2.1.2. Work Hardening

As previously mentioned, dislocations shear a given precipitate and weaken the effective area of the particle, which makes it easier for subsequent dislocations to cut the particle on the same slip plane. The dislocations accumulate and interact with each other, resulting in significant work-hardening within the PSB [127, 128, 132, 141-143, 205]. This work-hardening in many ways can relax the elastic stored energy during cyclic loading. Hence, it must be taken into account. In this model, the work-hardening is assumed to follow a Taylor relationship:

$$\tau^h = \alpha\mu b\sqrt{\rho} + \tau_o, \tag{6.7}$$

where the scalar, $\alpha = 0.45$ [264]. The initial shear stress, τ_o:

$$\tau_o = \frac{\sigma_y}{M}, \tag{6.8}$$

is given by the yield stress at the test temperature normalized by the Taylor factor, *M*, which is random (3.06) for this material, as shown in Table 3.4. The evolution of dislocation density with loading cycles (*N*) was extracted from literature for a similar nickel-based superalloy studied by Huang et al. [205] and a power law was used to fit the data, *F(N)*, as shown in Figure 6.4.

$$F(N) = A_1 N^{c_1} + A_2 \tag{6.9}$$

Since Huang's study only represents one test condition, the functional form of the dislocation density was amended by the following ratios for each variable:

$$\rho \propto \frac{\left(\gamma_{ratio}^{pl}\right)^2 \left(m_{ratio}\right)^2}{\exp\left(E_{ratio}^{\gamma-nuc-GB}\right)} \cdot F(N) \tag{6.10}$$

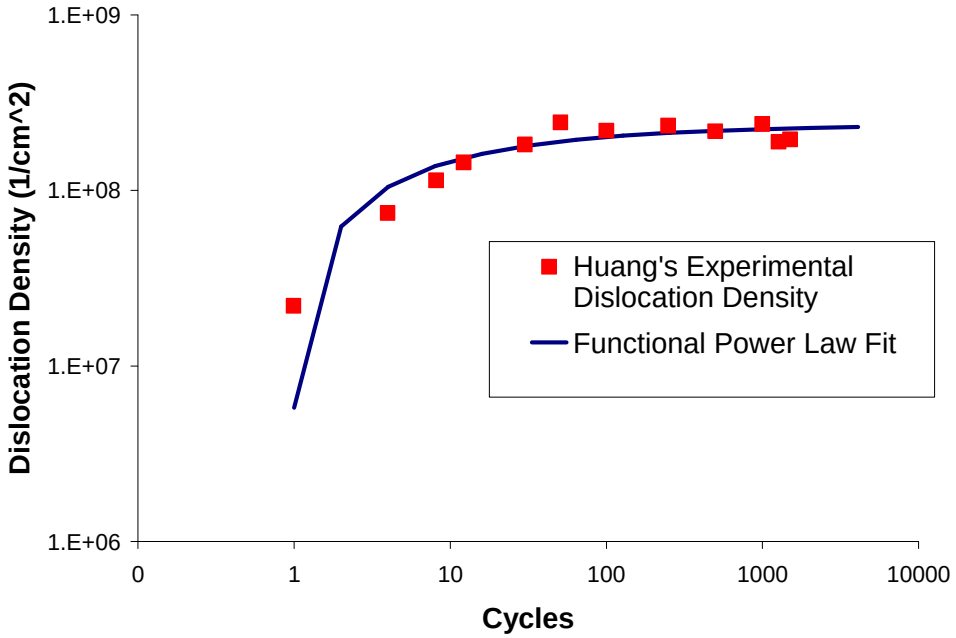

Figure 6.4. A power law fit is used to fit the dislocation density evolution. This data is taken from literature for a nickel-based superalloy from Huang et al. [205].

The relationship for the Schmid factor, *m*, and dislocation density is derived from simple expressions for the Taylor hardening and inelastic strain rate, respectively.

$$\tau = m\sigma = \alpha\mu b\sqrt{\rho} \;\Rightarrow\; \rho \propto m^2 \tag{6.11}$$

Similarly, by relating the Orowan equation to the inelastic strain rate, an expression between the dislocation density and activation energy is developed.

$$\dot{\gamma} = \vec{b}\rho\bar{v} = \dot{\gamma}_o \exp\left(\frac{-\Delta E}{kT}\right) \Rightarrow\; \rho \propto \exp(-\Delta E) \tag{6.12}$$

Due to the volatile nature of the exponential term, a Taylor expansion was used to the second power. The plastic strain amplitude relationship was verified by experimental data by Grosskreutz [132] for the dislocation density in copper single crystals as a function of shear flow stress, which can be related to the plastic shear strain as follows:

$$\rho \propto \left(\gamma^{pl}\right)^2. \tag{6.13}$$

6.2.1.3. Applied Stress

The applied shear stress (Figure 6.5a) for each grain, τ^A, is measured from the hysteresis behavior (Figure 6.5b), $\Delta\varepsilon^a$, of the material during the strain control test and multiplied by the Schmid factor of the individual grain, *m*.

$$\tau^A = m \cdot \Delta\sigma^A = m \cdot H(N) \tag{6.14}$$

The evolution of alternating stress during loading, $\Delta\sigma^A$, is obtained from the test data on the polycrystalline material, which is a nickel-based superalloy, U720 in this study. The stress response, *H(N)*, resembles a square root function as it hardens with increasing number of cycles and saturates. The stress is dependent on the applied strain, although at each strain range, the stress saturates after approximately 100 cycles.

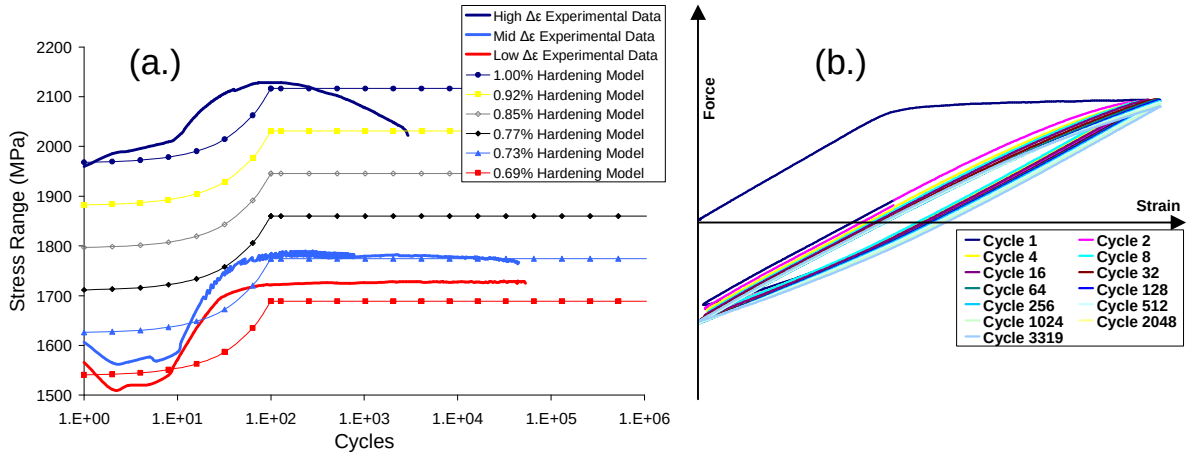

Figure 6.5. (a.) Evolution of the stress response to a strain-controlled LCF experiment, where each Δε value is normalized. At the highest strain range, multiple cracks form and interact resulting in cyclic softening towards failure. (b.) Hysteresis response of an LCF test of U720.

6.2.2. Atomistic Contributions

During the fatigue process, dislocations nucleate and shear the γ' precipitates to form shear bands. Once formed, the dislocations within the PSB interact with the GB. In order to capture the physics at the grain boundary interface, it is necessary to investigate this problem at a smaller scale. Hence, atomic simulations in the form of molecular dynamics (MD) are utilized and the results are incorporated into the energy balance in the form of energy barriers. This approach allows us to address the problems at hand and leverage our atomistic simulations, such that we do not encounter the inherently high stresses associated with MD. The following sections address the last four terms in Equation 6.1.

6.2.2.1. Dislocation Nucleation from GB and Agglomerating in the PSB

Dislocations nucleate during fatigue loading and agglomerate in the PSB resulting in a hardening response. GBs act as distinct sources for dislocations. Depending on the character of each GB, there is a different energy barrier for dislocation nucleation from the GB. In Section

5.4.2, it was shown that the energy barrier for nucleation, $E_{MD}^{\gamma-nuc-GB}$, is inversely related to the static GB energy, E_{Static}^{GB}, through a power law relation (Figure 5.8):

$$E_{MD}^{\gamma-nuc-GB} = 6.0\times10^{15}\cdot\left(E_{Static}^{GB}\right)^{-1.3}. \tag{6.15}$$

Hence, GBs with stable configurations and low interface energy have a larger energy barrier to nucleate a dislocation. With this information, we can model the energy associated with the nucleation of dislocations from a distinct GB as:

$$E_{nuc}^{disl} = \sum_{i}\partial X_i\cdot E_{MD}^{\gamma-nuc-GB}\left(\rho-\rho_o\right)\vec{b}hL^2\,. \tag{6.16}$$

The number of dislocations nucleating within the PSB during loading is represented by the evolution of dislocation density within the PSB multiplied by the cross-sectional area of the PSB: $(\rho-\rho_o)hL$. This energy contribution is dependent on the individual slip increment, ∂X_i for movement of a dislocation after nucleation.

6.2.2.2. Dislocation-GB Interactions to Form Extrusions

As previously mentioned, dislocations glide within the PSB and as a result the dislocations interact with the GB. Depending on the character of the GB, there are different energy barriers to dislocations penetrating the GB. Once again, this value is specific to the CSL Σ value, as measured from MD simulation, as shown in Figure 5.7. The relationship between the energy barriers for a dislocation to penetrate the GB, $E_{MD}^{\gamma-slip-GB}$, and the static GB energy is given by:

$$E_{MD}^{\gamma-slip-GB} = 2.8\times10^{13}\cdot\left(E_{Static}^{GB}\right)^{-0.6}. \tag{6.17}$$

In cases where the dislocations penetrate the GB, the PSB forms an extrusion across the GB, as shown in Figure 6.1. The intersection between the PSB and GB is a preferred site for

crack initiation as pointed out by Mughrabi et al. [151] and Blochwitz and co-workers [119, 169-171]. Thus, we must account for the energy in the formation of a static extrusion at the GB of the polycrystal; hence the associated energy with the PSB forming an extrusion (step/ledge features) at the GB is of the form:

$$E_{extrusion}^{slip-GB} = \sum_{i} \partial X_i \cdot E_{MD}^{\gamma-slip-GB} n_{dis}^{pen} \vec{b}h\,, \tag{6.18}$$

where n_{dis}^{pen} is the number of dislocations that penetrate the GB. This quantity can be approximated based on the AFM measurements of extrusions at the surface of a nickel-based superalloy by Risbet et al. [202-204]. In their study, they measured the height of the extrusions, which we normalize by the Burgers vector, ***b***, to obtain n_{dis}^{pen}. The extrusion height was measured as it evolved with increasing load cycles for various applied strain ranges. After a threshold number of loading cycles, N_{th}, the extrusions appeared and were pronounced; as expected, extrusions are observed after fewer cycles at higher applied strain ranges compared to lower strain ranges. The functional format, *G(N)*, used to fit this data is a square root dependency, based on models of Essmann et al. [148] and Differt et al. [149] of surface roughness.

$$G(N) = A_2\sqrt{N - N_{th}} \tag{6.19}$$

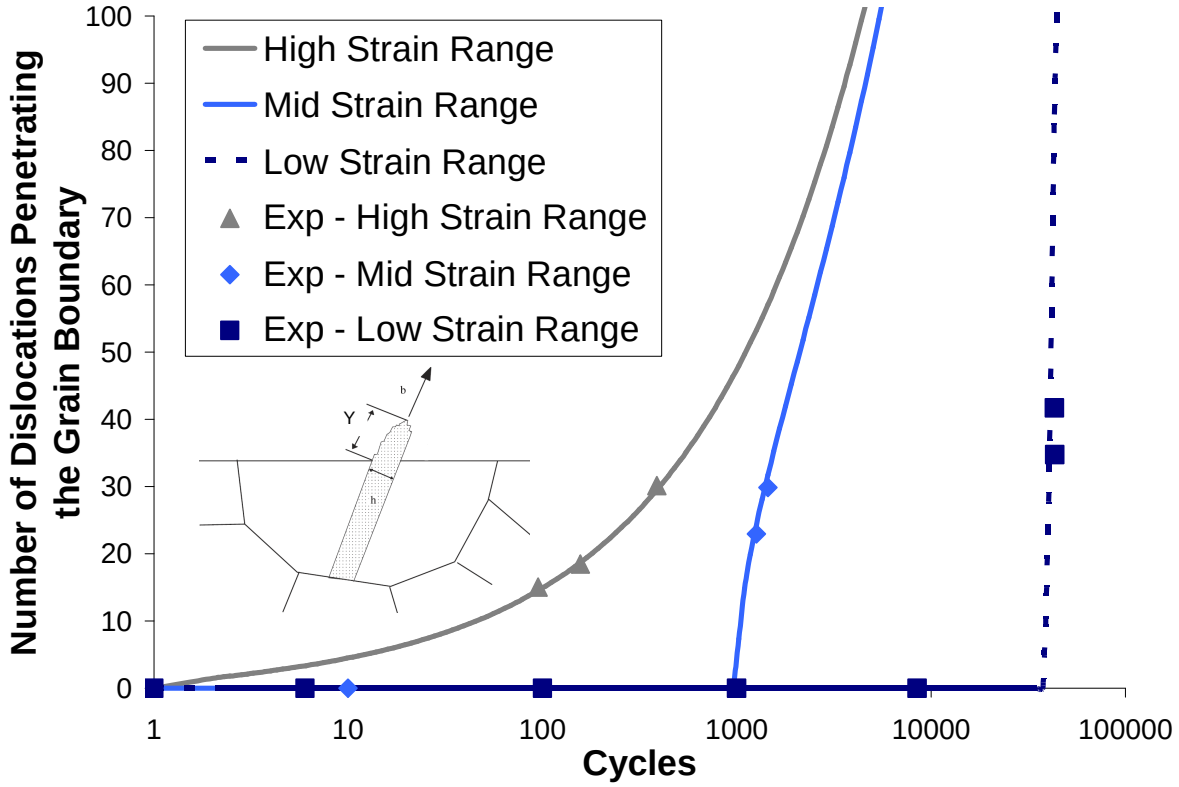

Figure 6.6. Number of dislocations forming an extrusion during cyclic loading. The data is measured via AFM by Risbet et al. [202-204] for a nickel-based superalloy and a functional was fit to the data according to Equation 6.19.

Once again, the values of the AFM measurements must be normalized to account for different microstructure conditions; hence n_{dis}^{pen} is proportional to the following ratios:

$$n_{dis}^{pen} \propto \left(\gamma_{ratio}^{pl}\right)^2 \left(m_{ratio}\right)^2 \left(L_{ratio}\right) \cdot G(N), \tag{6.20}$$

where the plastic strain ratio is confirmed by the experiments of Risbet et al. [202] and the theory by Mughrabi et al. [151], and the grain size dependency is derived by the irreversible slip in a PSB model by Risbet et al. [203]. Similar arguments were made for the Schmid factor and plastic shear strain dependence as aforementioned in Equations 6.11 and 6.13, respectively. We can effectively modify Risbet et al.'s AFM measurements of the extrusion height at the free surface to quantify the static extrusions across GBs.

6.2.2.3. Dislocations Shearing the Matrix and γ' Precipitates to form PSBs

The preceding sections addressed modeling PSB in general terms, here we refer to the case of superalloys investigated in this study. Thus, the mechanism for slip band formation in this material by cutting through the γ matrix and the γ' precipitates is discussed, as shown in Figure 6.7a. In order to do so, the dislocation must overcome an associated energy based on the glissile dislocation destroying the (FCC) lattice stacking sequence (Figure 6.7c) in the γ matrix and stacking sequence and order in the γ' precipitates as shown in Figure 6.7d,e, which correspond to the stacking fault, γ_{SF}, and anti-phase boundary, γ_{APB} (APB) energy, respectively. Various types of γ' precipitates form in these complex alloys; however, all are basically the same with respect to the issue of slip localization and shearing. Based on the composition of U720 and our characterization, we see the majority of the precipitates are comprised of Ni_3Al. For the sake of brevity, we model the γ' precipitates as Ni_3Al, which are in an ordered $L1_2$ structure, thus the ordering of the Ni and Al atoms within the lattice create the additional obstacle to slip (Figure 6.7d). Hence, the energy associated with the formation of the PSB from shearing the γ matrix and the γ' precipitates is given by:

$$E_{APB} + E_{\gamma-SF} = \left(f\int_o^L \gamma_{APB} dL + (1-f)\int_o^L \gamma_{SF} dL \right) n_{eff}^{layers} \partial X \ , \tag{6.21}$$

where f is the volume fraction of γ' precipitates and n_{eff}^{layers} is the number of effective layers contributing to the stacking fault or APB energy, as each additional layer provides 95% of the energy value of the prior layer. For U720, the fraction of γ' precipitates is approximately 0.20 as shown in Figure 6.7b by the use of image analysis software on optical micrographs.

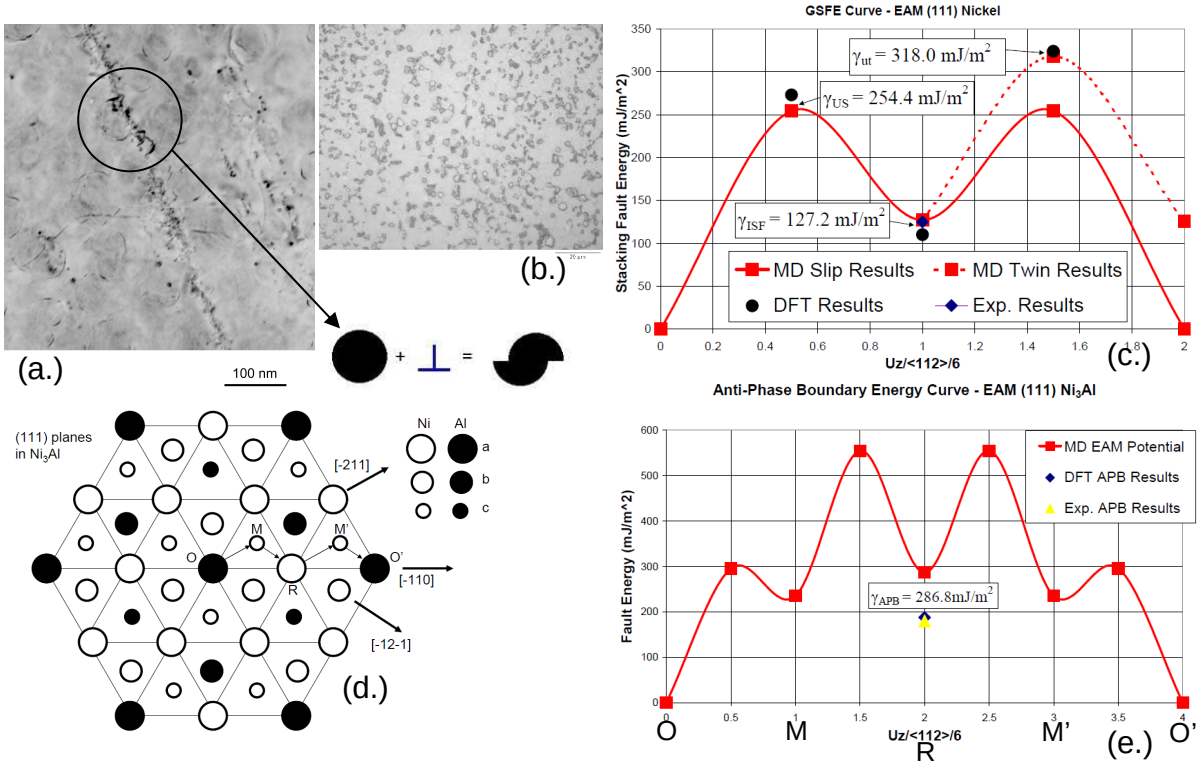

Figure 6.7. (a.) Dislocations shearing the γ' precipitates, which is necessary to form slip bands. g/3g weak-beam image shown with contrast inverted. (b.) Optical image of U720, displaying the γ' precipitates (fraction ≈ 0.20). (c.) Generalized stacking fault energy (GSFE) curve, which corresponds to the energy pathway for slip in the matrix material. (d.) Schematic of the ordered Ni_3Al γ' precipitates, redrawn from Reference [265]. (e.) The corresponding energy pathway that must be overcame to penetrate the precipitate, also referred to as the anti-phase domain boundary energy (APB).

An EAM potential for Ni [253] was chosen to match the intrinsic, γ_{ISF}-127 mJ/m^2, and unstable, γ_{US}-255 mJ/m^2, stacking fault energies of the material (Figure 6.7c), which compares well with experimental values of 125-128 mJ/m^2 and ab initio calculations of 273 mJ/m^2 for the γ_{ISF} and γ_{US} energies, respectively [254]. It is critical to obtain reasonable values of the unstable stacking fault energy as this parameter has been tied to the mechanics and nucleation of dislocations [255]; hence this Ni potential was used to generate the MD simulations for dislocation nucleation and penetration of GBs (Chapter 5). The anti-phase boundary energy is calculated using the EAM potential for Ni-Al in the $L1_2$ structure [266], each of which gives very good agreement with the individual stacking fault energies for Ni and Al, although the APB

energy is slightly higher compared to experimental and ab initio results for the ordered Ni_3Al intermetallic [265] (Figure 6.7e).

6.2.3. Failure Criterion

Remaining consistent with the other historical energy balance for fracture [261], twins [262, 263], dislocation emission [110, 255], and crack initiation [181], we check the stability of the PSB by differentiating with respect to plastic deformation, specifically movement of the glissile dislocations. Each component of the energy balance in Equation 6.1 is expressed as an increment of slip, ∂X_i, thus making differentiation very amenable and computationally efficient. The minimum energy of the PSB is determined:

$$\frac{\partial E}{\partial X_i} = 0 . \tag{6.22}$$

Additionally, the second derivative of the energy must be positive to ensure that the energy corresponds to a local stable minimum. Thus, we establish Equation 6.22 as our failure criterion for fatigue crack initiation corresponding to stability and equilibrium of the PSB's energy.

Hence, this model sums the energy contributions of each term in Equation 6.1 within the grain most likely to form a PSB (favorable energy for failure based on combination of orientation, grain size, and adjacent grain boundary character - CSL Σ values). This energy balance evolves with increasing loading cycles; meanwhile physically there is significant irreversible slip within the PSB leading to dislocations penetrating the GB thereby forming extrusions. When stability of the PSB is reached, i.e. it reaches a minimum energy configuration, a crack initiates from the PSB. The crack nucleates at the site of the extrusions (ledge and step features) at the intersection of the PSB and GB.

6.3. Test Cases

Various test cases at a series of total applied strain ranges, $\Delta\varepsilon^a$, were created to check this model for trends such as grain sizes, CSL Σ values, and Schmid factors. The microstructure features of the grain within the polycrystal in which a PSB forms is shown in Table 6.1 for each test case along with the resulting cycles to crack initiation. The results are plotted in Figure 6.8 in a typical strain-life format. From these test cases, we can observe the variation in life by changing a single parameter. Hence, changing the grain size from 2 μm to 4 μm results in a reduction of life as shown by the differences in the blue to gray and similarly red to black curves (both solid and dashed lines) in Figure 6.8. Hence we can see that smaller grains exhibit a longer fatigue life as expected from literature [8-14].

Table 6.1. Fatigue model test cases results showing the cycles to crack initiation for various applied strain ranges based on deviations in the microstructure (grain sizes, CSL Σ values, and Schmid factors). Please note that the applied strain ranges are normalized values.

	Case 1	Case 2	Case 3	Case 4	Case 5	Case 6	Case 7	Case 8
Grain Size (μm)	2	2	4	4	2	2	4	4
CSL Sigma Value, Σ	7	7	7	7	9	9	9	9
Energy ratio (from Σ)	3.63	3.63	3.63	3.63	1.16	1.16	1.16	1.16
Schmid Factor	0.3	0.42	0.3	0.42	0.3	0.42	0.3	0.42
N_i for $\Delta\varepsilon^a$ = 1.00%	13,247	6,459	11,152	5,428	8,143	3,965	3,259	6,700
N_i for $\Delta\varepsilon^a$ = 0.92%	18,800	9,171	15,831	7,711	11,574	5,647	4,643	9,526
N_i for $\Delta\varepsilon^a$ = 0.85%	28,319	13,986	23,877	11,786	17,581	8,757	7,230	14,501
N_i for $\Delta\varepsilon^a$ = 0.77%	44,862	22,207	37,845	18,727	27,926	13,976	11,552	23,049
N_i for $\Delta\varepsilon^a$ = 0.73%	58,982	30,874	50,019	26,298	37,993	20,687	17,393	31,644
N_i for $\Delta\varepsilon^a$ = 0.69%	132,615	83,150	114,651	73,165	95,537	65,241	57,564	82,097

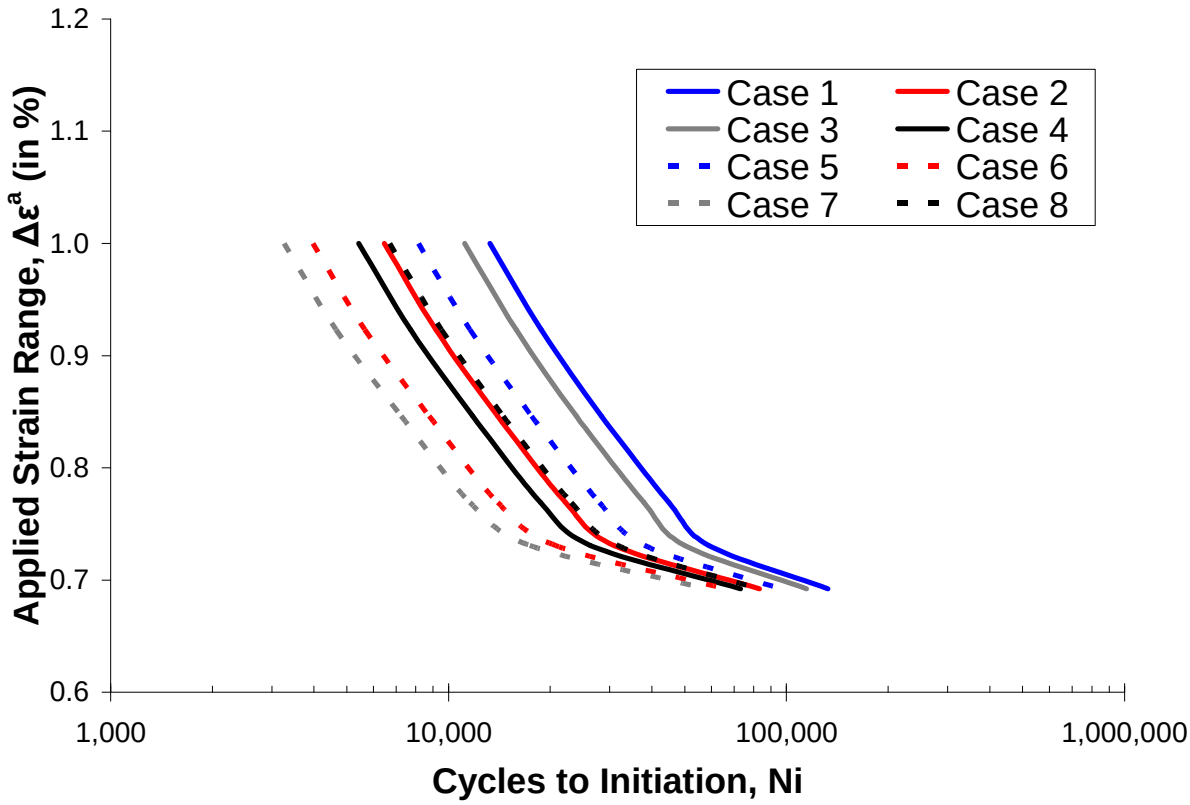

Figure 6.8. Strain-life curve for predicting crack initiation based on our physically-based fatigue model. The various curves represent test cases as described in Table 6.1. Please note that the applied strain ranges are normalized values.

Also, we see that the crack initiation life is significantly affected by varying the character of the GB, which is intersected by a PSB resulting in formation of a static extrusion at the GB. In Table 6.1, we display the result of two CSL Σ values: Σ7 and Σ9. In these cases, the Σ7 GB corresponds to a 38.2˚ twist rotation about the <111> axis and a relatively low energy of 503.5 mJ/m^2, meanwhile the Σ9 GB is a 38.94˚ tilt rotation about the <110> axis resulting in a significantly higher energy of 932.2 mJ/m^2. For the purpose of our code, the activation energy ratios as expressed in Equations 6.10 for the Σ7 and Σ9 GBs are 3.63 and 1.16, respectively; in this case the ratio refers to the activation energy value in comparison to the saturation values shown in Figure 5.8. Hence the result of varying the GB character from Σ7 and Σ9 is seen by comparing the solid to dashed lines of similar color in Figure 6.8. The lower static energy GB

(Σ7) offers a longer life, since it offers more impedance to slip nucleation/penetration thus resisting crack initiation; this in agreement with early work [17-19] suggesting GBs with low Σ value do not crack during fatigue testing. As expected, the most significant model dependency is the grain orientation as deviations of the Schmid factor from 0.3 to 0.42 results in substantial life degradation as shown by comparisons of the blue to red and gray to black curves (both solid and dashed lines) in Figure 6.8.

6.4. Discussion

This model is physically-based, thus incorporating the microstructure of the material, which provides an attractive solution to material failure. Moreover, the model sums the individual contributions to the PSB's energy, as PSBs have been observed in this material as a consequence of fatigue loading. As the PSB energy reaches a stable configuration and a minimum value, a crack initiates at the extrusion resulting from the penetration of the PSB across a GB. It is noteworthy that this physically-based model displays the correct trends for grain size, grain orientation (Schmid factor), GB character (CSL Σ value), and volume fraction of γ' precipitates as well as the familiar curvature for the strain-life plot. We analyzed the sensitivity of the microstructural variables on the model's prediction for cycles to crack initiation as shown in Figure 6.9.

The grain size sensitivity results showed that decreasing the grain size from 30 μm to 1 μm resulted in an approximately 5.3x increase in life until crack initiation, as shown in Figure 6.9a. Although experimental data is not readily available on U720, this trend (i.e. decrease in grain size leading to longer fatigue life) is seen in literature, as previously discussed [8-14]. Lukas and Kunz observed a fatigue life increase of ~3x (at a middle $\Delta\varepsilon^a$) by decreasing the grain

size by a factor of ~17x in copper [12]. Our model predicts an increase in fatigue life of 2.94-3.17x for a similar decrease in grain size. Thus, the trends and magnitudes that our fatigue model predicts seem reasonable, in addition our model predicts that PSB form in the larger grains in a polycrystal with a wide distribution of grain sizes, as observed for a variety of materials [119-121] including nickel-based superalloys [207]. The grain size dependency is inherent to our model. As each term essentially involves an energy density, which must be multiplied by the volume of the PSB to obtain the energy. Since, PSBs span the entire length of the grain, there is a grain size dependency in each term. For the energy to nucleate dislocations from the GB and accumulate in the PSB, the length scale dependency is squared. Since the energy density is proportional to the number of dislocations in the PSB; in order to find this quantity, the dislocation density, ρ, must be multiplied by the area of the PSB (hL).

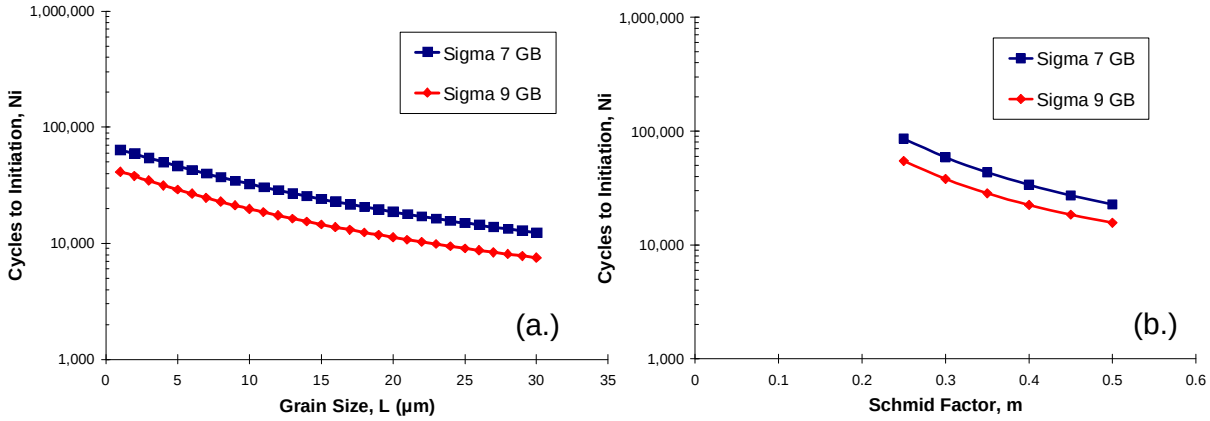

Figure 6.9. Sensitivity analysis of the model based on varying the input factors for (a.) grain size, L, and (b.) Schmid factor, m, for PSBs forming extrusions across Σ7 and Σ9 GBs. For these test cases, the applied strain range is 0.73%.

Likewise, an approximately 2.6x increase in fatigue life was observed by a variation in the Schmid factor from 0.50 to 0.25 in the grain orientation sensitivity chart in Figure 6.9b. Thus, higher Schmid factors (more favorable orientations) are prone to PSB formation and shorter fatigue life. This trend has been confirmed by experiments in the literature [120, 166-

168, 170, 207, 267 1981, 1981]. Experiments cannot quantifiably describe a one-to-one relationship between Schmid factor and fatigue life in polycrystals; this type of unique relationship is only established through a model with predictive capabilities. To establish the models relationship with the Schmid factor, we must analyze the individual terms. The continuum stress field is linearly dependent on the Schmid factor, since there is a direct correlation between the grain orientation and resulting number of dislocations. Further, both the dislocation nucleation and extrusion energy terms are proportional to the Schmid factor squared as previously discussed, thus controlling the relationship.

As seen in Figure 6.9, by changing the character of the GB from Σ9 to Σ7, the fatigue life increased by approximately 55%. The dominating terms controlling this behavior were the dislocation nucleation and extrusion energy both had a power-law dependence on the activation energy barrier presented by the character of the GB. Once again, it is difficult to establish bicrystals of U720 to experimentally depict this trend. Thus, we must rely on the MD simulations and model's prediction, and also confirm this behavior from the literature. There have been many experimental studies, which suggest lower energy CSL boundaries resist cracking and have an extended fatigue life [17-19].

Further, each term in this analysis is seen to saturate except for the extrusion energy. Hence, during the fatigue process, there is a dynamic equilibrium between the dislocation nucleation and annihilation, which results in the dislocation density reaching a nearly constant value. The saturation of the dislocation density evolution represents irreversibility within the fatigue model. At the saturation point, the number of dislocations that are generated and annihilated are approximately equivalent. Thus, the dislocation nucleation energy, applied stress, dislocation pile-up energy, work-hardening, and energy associated with slip (APB and SF)

also reach a constant value in our model. Although, during this saturation process, the dislocations still flow within the PSB, resulting in extrusions at the GB, hence the extrusion energy is the only term in our energy balance that does not saturate.

The back-stress that the material experiences during the unloading portion of fatigue is taken into account from the internal stress field created by the pile-up of dislocations, applied loading, and work-hardening of the system. Additionally, this model can be amended to account for fatigue loading with various R-ratios (mean stresses). The application of normal loading has been shown to affect the stacking fault energy curve [268], thus having a significant impact on the response of each of the terms established by atomic simulations (last four terms in Equation 6.1). Further, we would like to reiterate, that U720, a wrought nickel-based superalloy, was chosen to display our model's effectiveness due to the complexities and vast distributions of features in the material's microstructure. The concepts presented in this model are general for fatigue in any pure metal or alloy whose failure mechanism is attributed to slip localization in the form of PSBs, thus this model is applicable to a wide-class of materials in order to predict fatigue crack initiation.

6.5. Summary

This study represents a substantial effort in the field of physically-based fatigue modeling. The major contributions are as follows:

- Through optical and TEM imaging, the fatigue crack initiation mechanism in U720 is experimentally observed to be transgranular facets formed from persistent slip bands.

- The contributing elements to the energy of the PSB were identified. In order for plastic deformation to occur within the PSB, a dislocation must glide within a stress field established by the dislocation pile-up, work-hardening of the material, and applied stress. Additionally, the energy barriers for dislocations to nucleate from and penetrate a GB were determined from MD simulations. These MD contributions serviced our model as the γ matrix/γ' precipitates were sheared, dislocations nucleated/collected within the PSB, and extrusions formed at the intersection of the PSB and GB.
- The aforementioned terms were expressed in an energy balance for the total energy of the PSB, which evolved with increasing fatigue cycles. Stability of the PSB corresponded to a minimum value of the energy balance, which was computed as the derivative of the total PSB energy with respect to plastic deformation (i.e. an increment of slip) reaching zero, which is consistent with other historical energy balance approaches.
- This methodology is attractive since it is physically-based and inherently accounts for the microstructure of the material. The result of which produces the correct trends for predicting fatigue crack initiation based on total applied strain range, grain size, grain orientation, GB character (CSL Σ value), and volume fraction of γ' precipitates; all of which have a significant impact on the fatigue life of the material.

Chapter 7. Role of GBs on Fatigue Crack Initiation

7.1. Overview

In this chapter, we extend the PSB energy balance methodology to predict failure in a polycrystalline material, in order to do so, we investigate PSB-GB interactions. These PSBs are able to traverse low-angle grain boundaries (LAGB), thus belonging to clusters of grains. As a consequence of the ongoing cyclic slip process, the PSBs evolve and interact with high-angle GBs (HAGBs), the result of which leads to dislocation pile-ups, static extrusions in the form of ledges/steps at the GB, stress concentration, and ultimately crack initiation. Hence, our fatigue model is driven by the microstructure, and its results predict that cracks initiate near twin boundaries from PSBs spanning a single large grain with a favorable orientation or multiple grains connected by low-angle GBs. Excellent agreement is shown between model predictions based on EBSD scans of U720 and experimental data.

7.2. Extension of Model to Polycrystalline Materials

In Chapter 6, we establish an energy balance based on a PSB in the most favorably oriented grain of a polycrystal. This methodology is extended to include the experimental observations of Zhang, et al. [173, 176-178, 208], which state that PSBs can traverse LAGBs (Figures 7.1a,c) and are impeded by HAGBs (Figures 7.1b,d). Hence, PSBs can form over multiple grains, which need to be accounted for in our study. From these observations, we no longer consider the most favorably oriented grain but rather the most favorable grain clusters for PSB formation and crack initiation. Many experimental and numerical analyses have addressed

the role of grain-grain interaction in heterogeneous monotonic deformation [269-274], thus supporting our concept of grain clusters leading to fatigue damage.

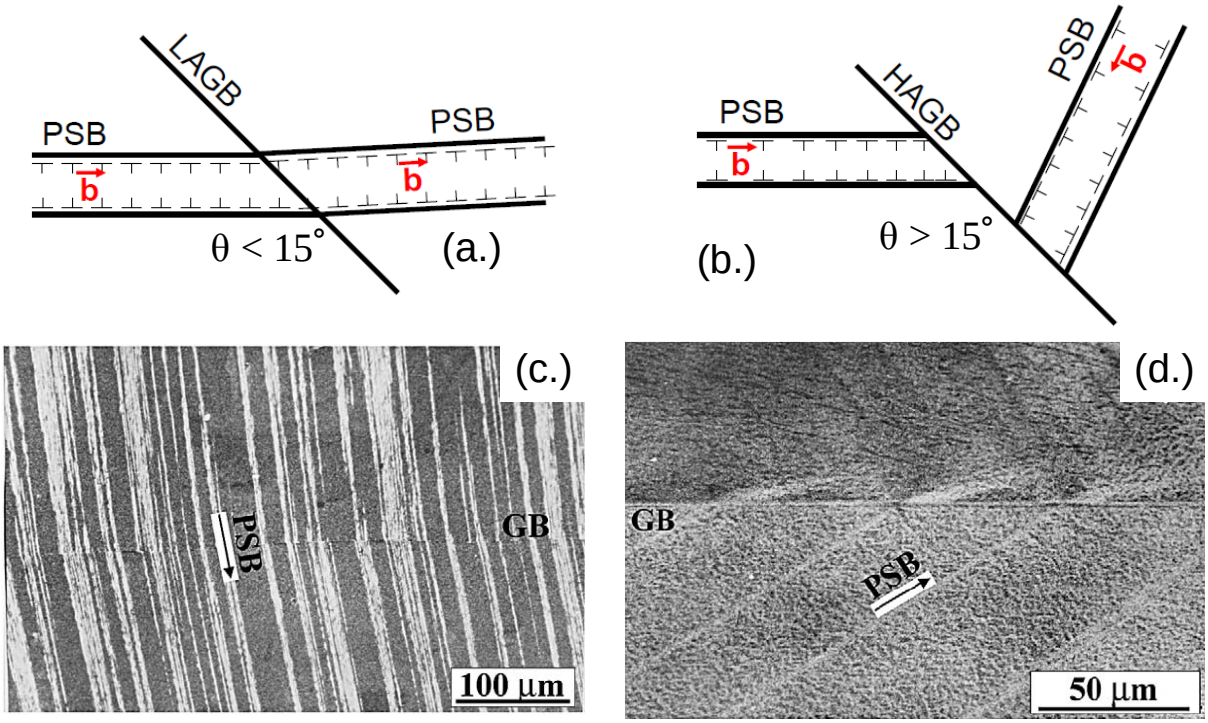

Figure 7.1. (a.) Transmission of a PSB through a LAGB (misorientation, θ < 15˚), (b.) PSBs cannot penetrate through HAGBs (θ > 15˚). (c.) PSB penetrate a LAGB [178], (d.) PSB impeded by a HAGB resulting in dislocation pile-up and stress concentration [178]. TEM images of PSB-GB interactions are shown for Cu, taken from Zhang and Wang.

From the EBSD analysis, the LAGBs are identified within the material. In these cases, the PSB is permitted to traverse the LAGB and into the adjacent grain. This can occur multiple times if LAGBs connect clusters of grains adjacent to one another, as shown in Figure 7.2. In cases where a grain cluster exists, the Schmid factor of the cluster is the average of the Schmid factor of the individual grains. This is justified, since this material experiences planar slip, hence one slip system is activated in each grain and the LAGB requires a misorientation between the grains of less than 15˚. Therefore, the same primary slip system is activated in the adjacent grain with only minor deviations in the slip direction. Further, the area of each grain in the cluster is summed to obtain the area of the grain cluster. The energy of the PSB traversing the LAGB,

$E_{LAGB}^{\gamma-slip-GB}$, is accounted for and added to the overall energy balance (Equation 6.1) according to the following relationship:

$$E_{LAGB}^{PSB-GB} = \sum_i \partial X_i \cdot E_{MD}^{\gamma-slip-GB} \vec{b}h, \tag{7.1}$$

where $E_{MD}^{\gamma-slip-GB}$ is the energy barrier for slip penetration into the adjacent grain as indicated by the Σ1 GB value in Figure 5.7.

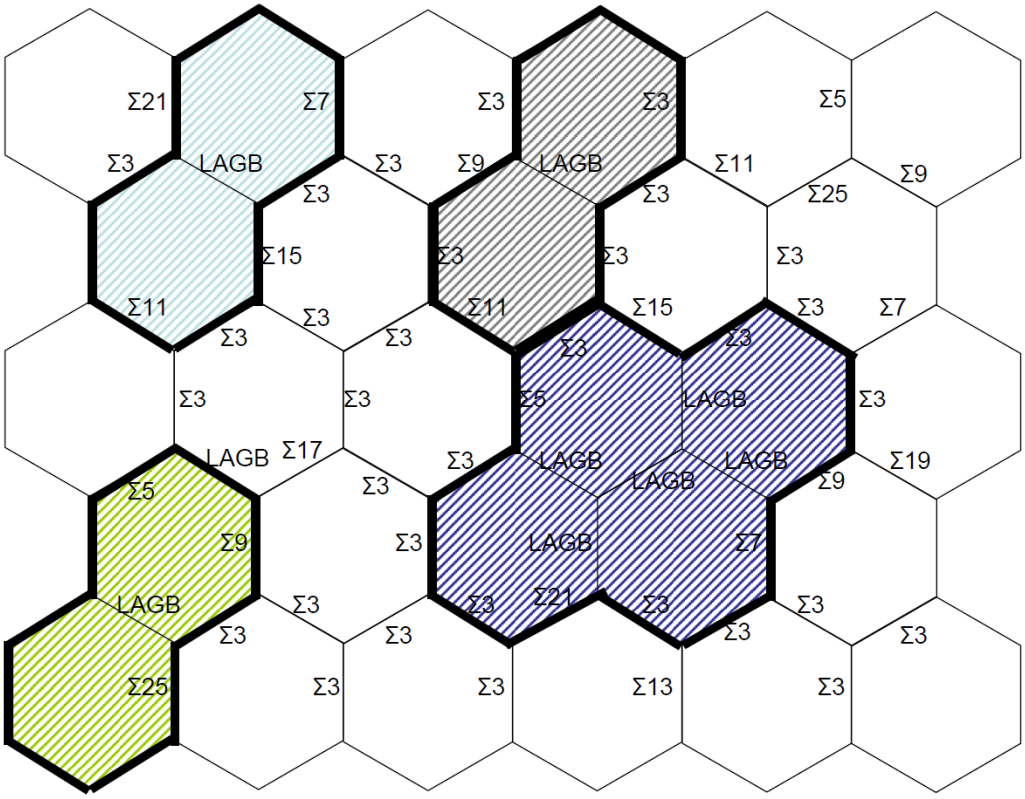

Figure 7.2. Schematic of a microstructure displaying the GB characters. From experimental observation, PSBs are able to traverse LAGB. Thus, PSBs form in grain clusters connected by LAGBs as indicated.

Additionally, dislocation evolution is seen within each grain in the cluster. Hence, energy associated with dislocations nucleating and agglomerating within the PSB is taken from the most favorable GB to emit dislocations during loading. In other words, as shown in Figure 5.8, the lowest energy barrier for nucleation is analogous to the highest static GB energy, which is the GB most likely to emit dislocations within each grain of the cluster. This highest GB

energy value per grain is weighted by the grain area and summed for each grain within the cluster. Hence, for a cluster containing j grains, Equation 6.16 becomes:

$$E_{nuc}^{disl} = \sum_{i} \partial X_i \cdot \left\{ \sum_{j} E_{MD,j}^{\gamma-nuc-GB} L_j^2 \right\} (\rho - \rho_o) \vec{b} h \,. \tag{7.2}$$

Once the chain of LAGBs is constructed, the PSB-GB interaction energy is calculated from the GB exhibiting the highest energy barrier against slip. This GB effectively impedes the PSB resulting in dislocation pile-up, static extrusions at the GB, stress concentration, and ultimately crack initiation. Therefore, the GB with the largest energy barrier analogous to the lowest static GB energy (according to Figure 5.7) is selected for the grains at the outskirts of the grain cluster; this value is used in Equation 6.18 to account for PSB-GB interactions.

7.3. Polycrystalline Fatigue Model

Thus far, we have presented a methodology for predicting fatigue crack initiation based on an energy balance, which examines each grain in the polycrystalline aggregate along with the formation of clusters, i.e. grains connected by LAGBs. In a sense, a weakest link is determined and cracks initiate from the PSB-GB interaction in this grain or grain cluster. A sensitivity analysis was preformed on the fatigue model by varying the orientation and size of the grains/clusters, while the GBs character and neighboring grains are held constant. As shown in Figure 7.3, the grain size (1 to 20 μm) and Schmid factor (0.215 to 0.5) were systematically varied, and the resulting fatigue lives were calculated. As expected, for large, favorably oriented grains, cracks initiated at a lower life as opposed to small grains with low Schmid factors. From this analysis, we can disregard the small grains (of size L in meters) with low Schmid factors, m, since the aggregate of grains fails from the weakest link. Hence, a threshold function is

determined based on Figure 7.3, whereas grains/clusters that exhibit a fatigue life of greater than 20,000 cycles were discarded.

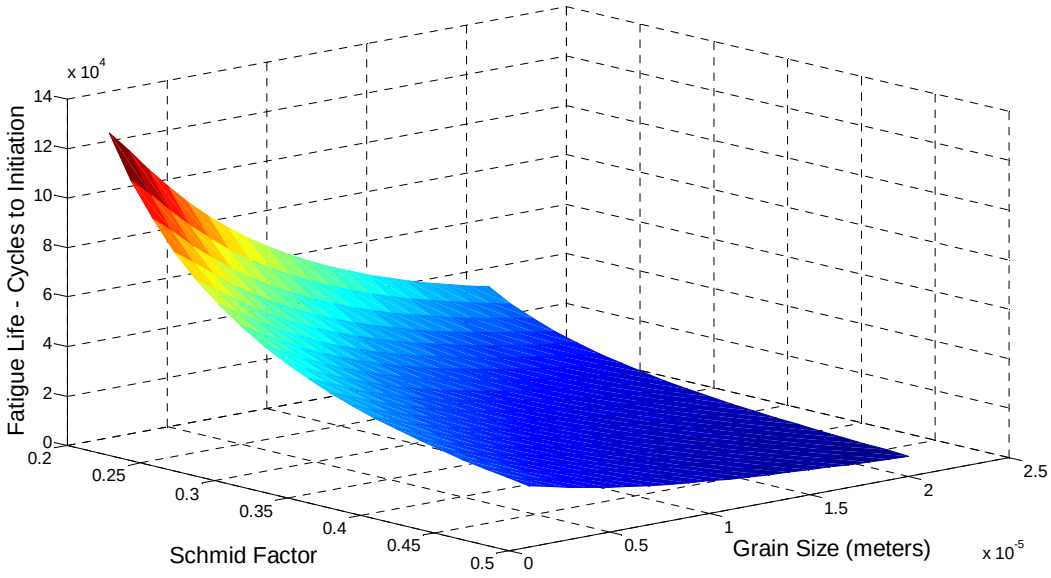

Figure 7.3. Sensitivity analysis of the model based on varying the input factors for grain size, *L*, and Schmid factor, *m*. This analysis allows us to set a threshold range on grains with problematic sizes and orientations that are most likely to be the weakest link in a polycrystalline aggregate.

This simulated result produces the following condition based on a curve fit of Figure 7.3, which must be satisfied to consider the specific grain or grain cluster in the energy balance.

$$m - 4.7x10^{8} L^{2} + 2.6x10^{4} L \geq 0.67 \tag{7.3}$$

Hence, regardless of the orientation, according to Equation 7.3, any grain less than 7.5 μm is not considered in the energy balance, since it is highly likely a crack will initiate elsewhere in the material. There is no upper bound to Equation 7.3 as larger grains are more likely to initiate fatigue cracks. As shown in Figure 3.5, this criterion discounts approximately 98% of the grains. For example, for specimen 2 containing 3664 grains, 113 grains/clusters satisfy Equation 7.3, in which 54% were single grains, 27% were grain clusters connected by a single LAGB, and 19% were grain clusters containing 3 to 7 grains. This simplification greatly improves computational

time. Given raw EBSD data, this code locates the fatigue clusters most likely to nucleate a crack and computes the fatigue life via an energy balance for each individual grain and cluster of grains satisfying Equation 7.3. Thus, cracks initiate in the specimen at the weakest link of the microstructure, from which a fatigue life is predicted. On average, for a given applied strain range, this aforementioned algorithm runs in approximately 15 seconds on a typical desktop computer, thus offering significant savings on computational cost versus other microstructurally driven fatigue models – such as cyclic crystal plasticity.

In order to illustrate the dominant terms in the overall energy balance (Equation 6.1), we show the energy evolution for specimens 1 and 2 at the highest and lowest applied strain ranges in Figure 7.4. Each term's contribution to the energy balance along with the total energy of the PSB is shown evolving with the applied loading cycles. As discussed, the continuum terms (first three terms of Equation 6.1) provide a stress field that must be overcome for slip within the PSB. Consistent with traditional energy balances, the relaxation of the elastic stored energy (due to the external forces) appears in the energy balance (Equation 6.3), resulting in a negative value for the blue line in Figure 7.4. The sharp kink in the blue line for the lower strain ranges (Figures 7.4b,d) occurs upon saturation of the dislocation density and the material hardening stress response to the applied external strain. The blue and light blue dashed lines represent dislocations cutting through the γ matrix and the γ' precipitates to form the PSB, which remain relatively constant throughout fatigue loading. The red dashed curve represents the energy of dislocations nucleating from the GB and forming within the PSB. This value increases slightly as the dislocation density increases and saturates. Physically, cracks initiate at the static extrusions (i.e. ledges/steps) across the GB as a consequence of PSB-GB interaction, dislocation pile-up, and stress concentration; hence this corresponding energy drives the energy balance.

Dislocations pile-up at the GB and eventually penetrate the GB forming extrusions, at which point the energy raises substantially as shown by the red curve. The black curve represents the total energy of the system, which is the sum of all other curves. The overall energy value is initially dominated by the applied work and later balanced by the PSB-GB interaction energy. Each of these curves represents the derivative with respect to a slip increment. Hence, as the black curve approaches zero, this corresponds to stability of the PSB and is our criterion for crack initiation. Attention must be paid to ensure that the stability refers to a minimum energy configuration of the PSB, hence the derivative of the total energy is zero and its second derivative is positive; this occurs the second time the black curve reaches zero. For clarity, this point is enlarged in the inset of Figures 7.4a,c.

The algorithm flowchart for our microstructure-based fatigue code is shown in Figure 7.5. The model reads in data from an EBSD scan in the form of grain ID, Euler angles, grain area, and a list of nearest neighbors per grain. This data is manipulated by a CSL code as described in Chapter 4, which characterizes the GBs according to its CSL Σ value and assigns a corresponding GB energy from MD simulations. The ensuing data is read into the grain cluster code as described in Section 7.2, which allows PSBs to transfer through LAGBs resulting in the formation of clusters, thus producing a list of grains and grain clusters. Based on the Schmid factor and size of each grain/cluster, its probability of failing is calculated by Equation 7.3. For grains that are likely to fail, the PSB energy balance is computed according to Chapter 6. The fatigue code requires inputs regarding the applied strain range and elastic/yield properties of the material (although deviations in the elastic/yield properties have a negligible effect on the predicted fatigue life). Finally, four experimental functionals (Chapter 6) and MD simulation ((Chapter 5) in the form of energy barriers (Equations 6.15, 6.17) and SF/APB energy) results

are needed for the PSB energy balance. Thus, the number of cycles to initiate a crack, N_i, is computed for a grain/cluster in the polycrystal. This process is repeated for each grain/cluster and the number of cycles to crack initiation is predicted based on the minimum value of N_i.

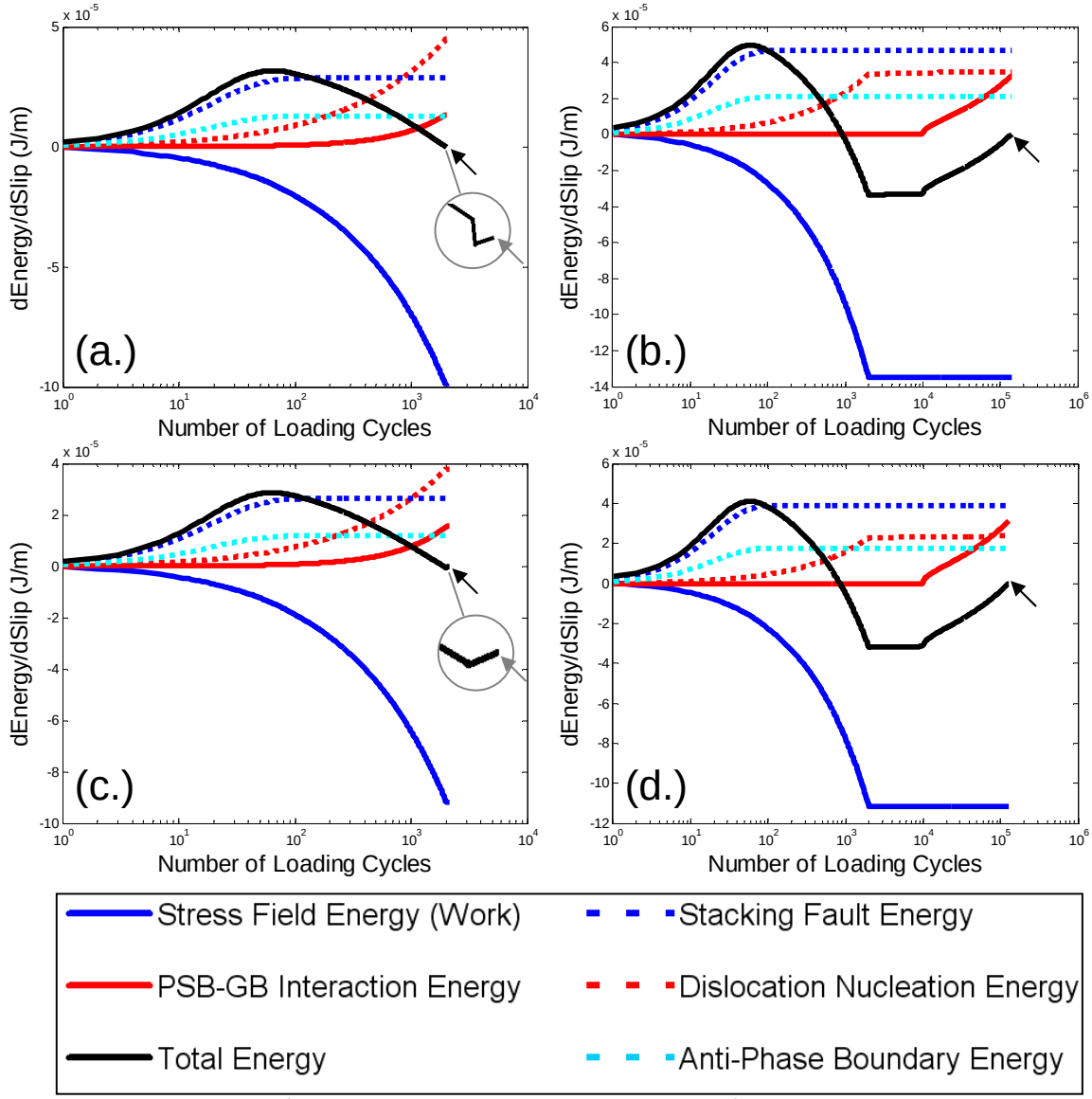

Figure 7.4. The evolution of the individual and total energy components from our energy balance (Equation 6.1) with increasing loading cycles; each term is expressed as a derivate with respect to a slip increment. Hence, the total energy (black line) reaches a minimum as its derivate approaches zero, which is defined as stability of the PSB and crack initiation. Four scenarios are shown corresponding to (a.) Specimen 1 at the highest applied strain range – 2,009 cycles to initiation, (b.) Specimen 1 at the lowest applied strain range – 140,518 cycles to initiation, (c.) Specimen 2 at the highest applied strain range – 2,138 cycles to initiation, and (d.) Specimen 2 at the lowest applied strain range – 129,323 cycles to initiation. In Figures 7.4a,c, the inset shows an enlarged image of the failure point, which indicates the total energy's derivative approaches zero with a positive slope (thus indicating a local minimum in energy).

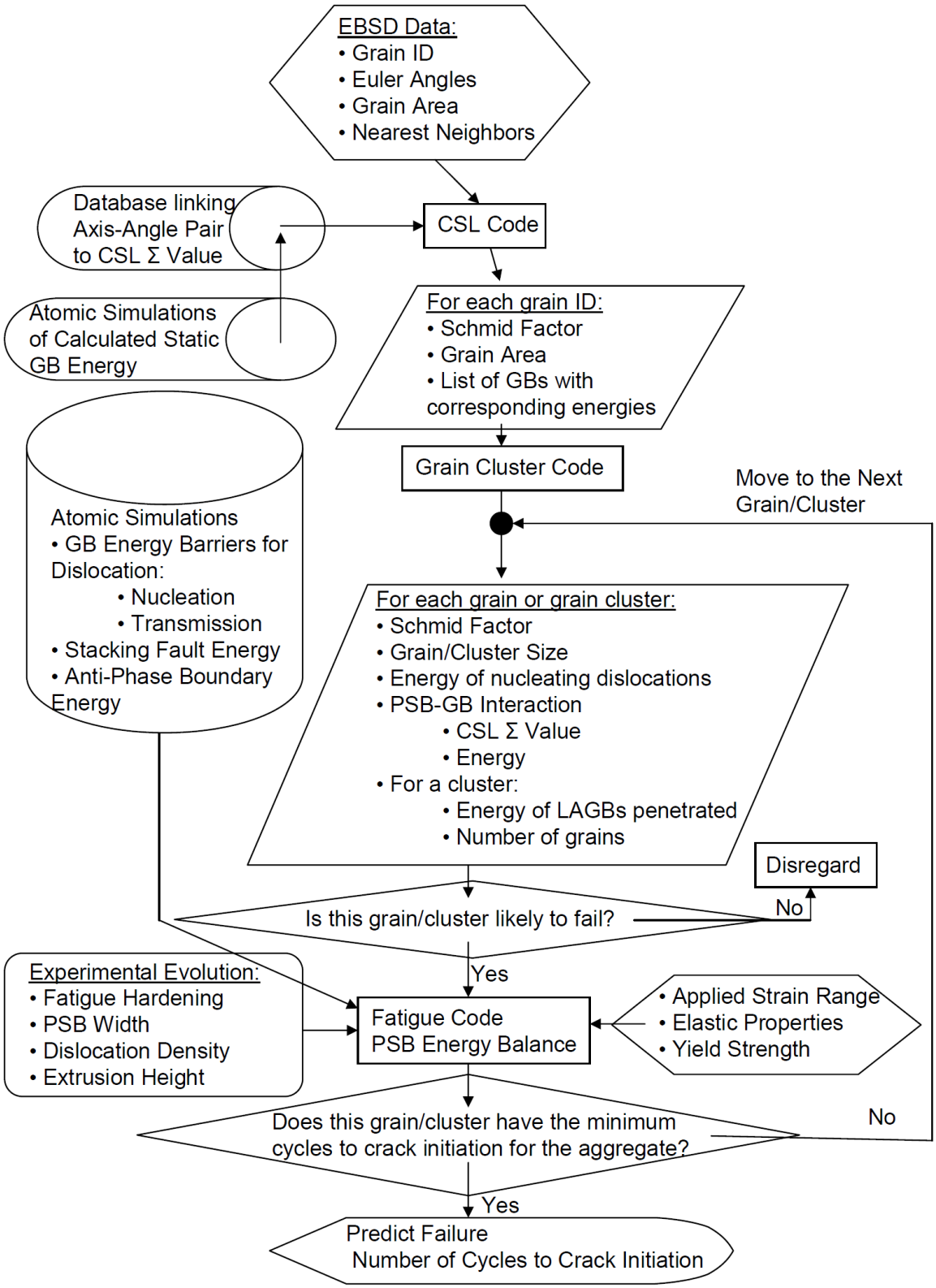

Figure 7.5. Algorithm flow chart describing the microstructure-based fatigue code methodology.

7.4. Results and Discussion

Material characterization in the form of EBSD was completed on three specimens as shown in Table 7.1. The resulting microstructures were loaded into our fatigue model to search for grain clusters most likely to fail. From this analysis, we determined the PSB which first nucleates a crack and the associated number of loading cycles in which this occurs. The results are shown in Figure 7.6 for the theoretical fatigue life of the three simulated specimens along with the experimental log averages and log standard deviations representing 84 experiments as shown with a normalized applied strain range. It can be seen that the model results are within a single standard deviation of the experimental results, thus producing very good agreement.

Table 7.1. Statistics of EBSD characterization on the specimen's microstructure.

	Specimen 1	Specimen 2	Specimen 3
Number of Grains	2,373	3,664	7,424
Average Grain Size (μm)	5.3	4.2	2.4
Grain Size Standard Deviation (μm)	2.2	1.9	0.9
Largest Grain Size (μm)	18.4	16.7	8.3
Average # of GBs per 2D Grain Scan	5.6	5.6	5.4
Average Schmid Factor	0.450	0.451	0.456
Low Angle GB (LAGB or Σ1) Fraction	13.2%	17.4%	9.4%
Σ3 -Twin Boundary Fraction	48.3%	46.9%	46.3%
Taylor Factor of Aggregate	3.065	3.074	3.071

The nickel-based superalloy, U720, tested in our study displays a lot of microstructure deviation (Table 7.1) and as a consequence, a large scatter in fatigue results is observed. The simulated specimens are no different, in the sense that specimens 1 and 2 exhibit a large standard deviation in grain size; meanwhile specimen 3 displays a very fine grain size with minimal deviation. All three specimens have a random orientation of grains, thus no texturing effects are observed. Each of the specimens has a large percentage of twins. Also, specimen 1 and 2 have more LAGBs, consequentially more grain clusters form in these two specimens.

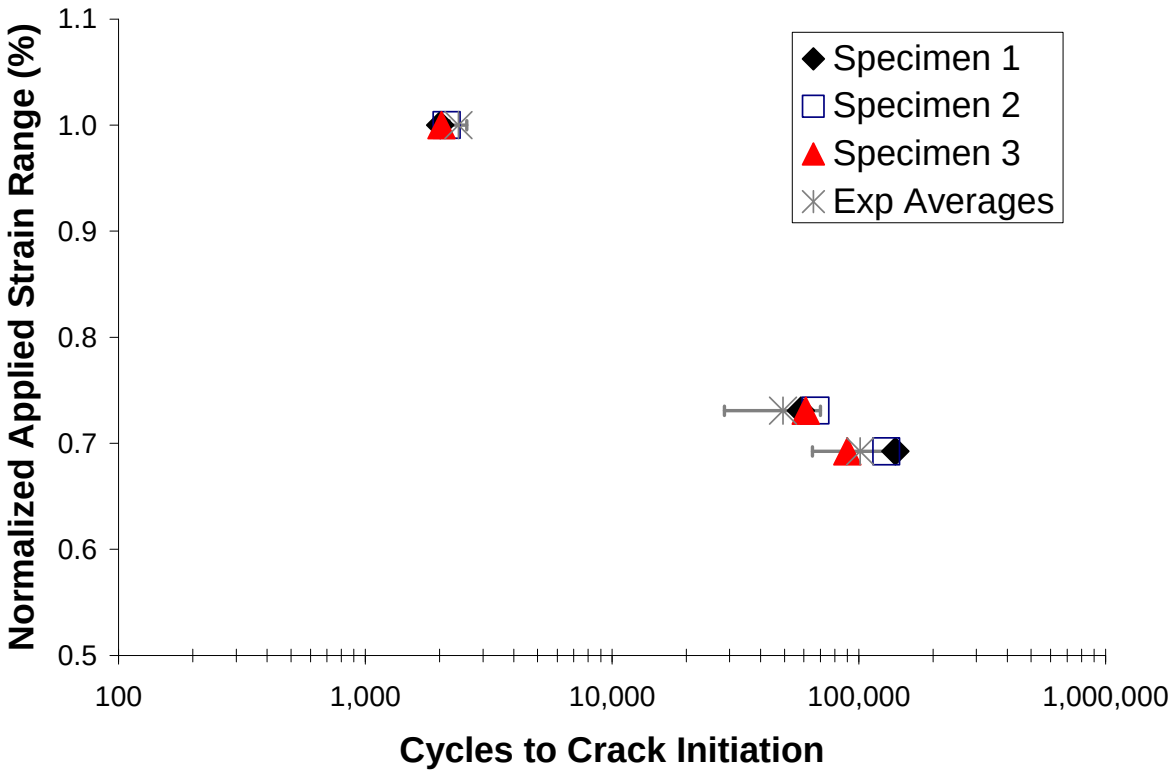

Figure 7.6. Predicted fatigue results for the three specimens which were characterized by EBSD scans (Table 7.1). The predictions are compared to experimental log averages and log standard deviations based on 84 fatigue experiments. Please note the applied strain ranges are normalized values.

It is expected that due to the large number of LAGBs and larger grain size, specimens 1 and 2 would have a shorter fatigue life, which is seen in the intermediate strain ranges. Although surprisingly, each of the specimen has nearly the same fatigue life over the span of the simulated strain ranges. From a statistical point of view, in the case of fatigue, which contains multiple variables, failure is not due to extreme cases, such as unusually large grains or many connected LAGBs. Rather, the critical condition more readily occurs, due to a natural series of factors aligning themselves, such as a couple of large grains (size – one standard deviation greater then average) connected across a LAGB to form a cluster that is orientated with a high Schmid factor.

Interestingly, in Figure 7.6, the fatigue life trends from the three specimens is not always the same, i.e. a given specimen type has the shortest fatigue life at a given strain range and the

longest life at a different strain range. Hence, we see different terms dominate the energy balance at different strain ranges. Thus, in a given aggregate, different grain clusters are the weakest link depending on the applied strain range as shown in Table 7.2. At low strain ranges, a single grain is the cause of failure (Figure 7.7a); meanwhile, at higher applied strain ranges, a cluster containing multiple grains typically fails first (Figure 7.7b). In specimen 3, the grain size is small and narrowly distributed; hence the same grain cluster fails at each strain range.

Table 7.2. Model predicted fatigue results in terms of number of cycles until crack initiation for three specimens at a range of normalized applied strains. The location in the microstructure, i.e. weakest link – grain or grain cluster, where the crack initiates is illustrated by the number of grains within the cluster (1 if a single grain), Schmid factor, size, and GB character in which PSB-GB interaction takes place.

Specimen Number	Normalized Strain Range	Cycles to Initiation	# of Grains within Cluster	Schmid Factor	Cluster Size (μm)	CSL Σ Value
1	1.00	2,009	3	0.493	9.39	3
1	0.92	2,055	1	0.460	12.94	3
1	0.85	2,785	1	0.492	15.29	3
1	0.77	17,795	1	0.492	15.29	3
1	0.73	58,306	1	0.492	15.29	3
1	0.69	140,518	1	0.492	15.29	3
2	1.00	2,138	3	0.493	8.63	3
2	0.92	2,271	2	0.486	11.03	3
2	0.85	5,876	2	0.429	12.99	3
2	0.77	23,185	1	0.483	12.80	3
2	0.73	66,913	1	0.483	12.80	3
2	0.69	129,323	1	0.483	12.80	3
3	1.00	2,036	2	0.497	8.34	3
3	0.92	4,437	2	0.497	8.34	3
3	0.85	10,270	2	0.497	8.34	3
3	0.77	23,864	2	0.497	8.34	3
3	0.73	61,104	2	0.497	8.34	3
3	0.69	89,847	2	0.497	8.34	3

From the simulated specimens, we see the size of the clusters is in the range of 8.3 μm to 15.3 μm. This approaches the facet sizes (15 μm to 135 μm) measured from the fracture surfaces of failed fatigue experiments, as shown in Figure 3.9. We would expect to see larger grain clusters, which mimic the facet size, if more specimens are tested from EBSD scans that encompass a greater area. Another possible reason for the discrepancy between cluster size and

facet size is that experimentally short cracks initiate and experience slow crack growth. These fine growth features cannot be distinguished in the facet; hence the facet is not a good measure of grain cluster size which causes crack initiation.

In each specimen, the crack initiate from a PSB-GB interaction, in which the GB is composed of a Σ3 boundary, also known as a twin (Figures 7.7). Our model's results match experimental observations, [207, 218-223], which suggest that cracks most likely initiate near a twin boundary, as shown in literature (Figure 7.7c) and SEM analysis of U720 fracture surfaces (Figures 3.8b,c). We showed that the TB has the highest energy barriers against slip (Figure 5.7). As a consequence, PSBs are impeded resulting in high stress concentration, higher energy, and crack formation. Physically, the material alleviates the high resolved shear stress by nucleating a crack.

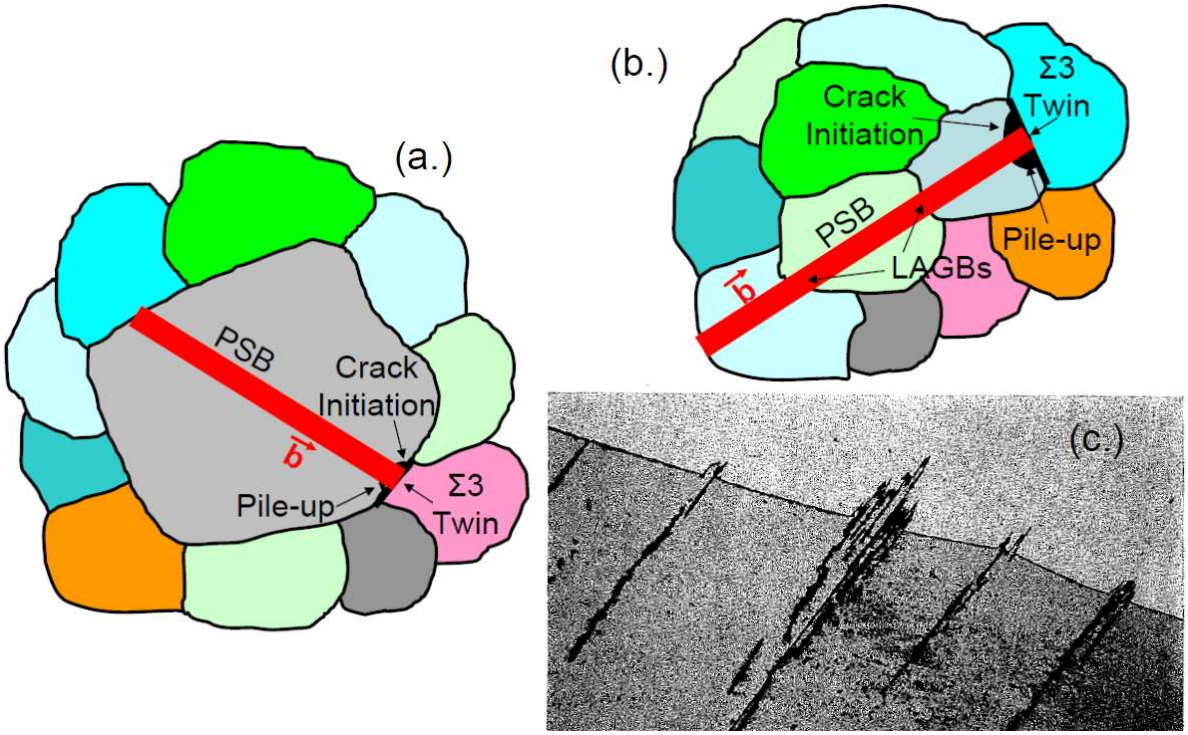

Figure 7.7. PSB are impeded by twin (Σ3) boundaries resulting in dislocation pile-up, stress concentration, and crack initiation as shown in (a.) one large grain and (b.) three small grains connected by LAGBs. (c.) PSBs are seen to be impeded by TBs in Cu resulting in dislocation pile-up and formation of static extrusions at the GB. This image is taken from Boettner et al. [220].

As aforementioned, in literature the role that twins play in the fatigue response of a material is still an issue of debate. From our analysis, we establish their role as follows. Twins are both beneficial and detrimental to the fatigue performance. As previously shown, TBs exhibit the lowest static energy (Figure 5.1) as well as the highest energy barrier for slip transmission (Figure 5.7). Hence, twins have an important role in the macroscopic hardening of the material, since they do not allow for emission of dislocations and further confine their motion. This hardening response (as shown by the applied work curves in Figure 7.4) acts to extend the fatigue life of the material. Although, in microstructures that have widely distributed grain sizes or contain a large percentage of LAGBs, PSBs are seen to form in large grains (Figure 7.7a) and/or multiply connected grains (Figure 7.7b), i.e. grain clusters. As the PSB interacts with the TB, the results show that the TB's high energy barrier for slip, results in dislocation pile-ups, stress concentration, static extrusions, higher energy, and ultimately crack initiation. Thus, TBs are detrimental to and reduce the fatigue response once a PSB forms in materials with large grains or chains of connected LAGBs, as shown in Figures 7.7a,b.

Finally, the proposed fatigue model is physically-based and incorporates features of the microstructure. In building the energy balance, four functionals are fit to experimental data: (a) the macroscopic hardening stress from fatigue experiments, (b) PSB width from TEM measurements, (c) the dislocation density evolving with number of cycles from literature for a similar nickel-based superalloy [205], and (d) PSB extrusion height (AFM) measured from literature [202-204]. Hence minimal experimental fitting parameters are used and further no extraneous fitting constants are used in this model. From this study, we can conclude that this model is in very good agreement with the experimental data and is therefore validated.

7.5. Summary

In this chapter, we extended the previous PSB energy model to account for PSB-GB interaction, in order to predict fatigue crack initiation in polycrystalline materials. As a consequence of this effort, the major contributions are as follows:

- PSB are more likely to form in large grains with favorable orientations. Although, the PSBs can traverse LAGBs, thus linking grains together to form grain clusters. In doing so, we account for groups of grains, which are likely to fail and thus modify the energy balance appropriately.
- EBSD scans were completed on three specimens. From this data, grain clusters were identified and the fatigue analysis was completed on each cluster to determine the fatigue life of the weakest link in the material. The results were in excellent agreement with the experimental fatigue ranges of this material, thus validating our model.
- From the three specimens, we see that the grain clusters resulting in failure exhibited a range of grain sizes and contained various numbers of grains within the clusters. Hence, extreme cases (often known as large as (ALA) grains or a large number of connected LAGBs) did not constitute failure. Further, cracks initiated near a twin boundary, corresponding with experimental observations. Thus, the PSB-GB interactions resulted in dislocation pile-up, stress concentration, an increase in energy, and crack initiation. Additionally, we see that at various applied strain ranges, different mechanisms or terms within the energy balance dominated failure, resulting in various grain clusters representing the weakest link.

Chapter 8. Predicting Fatigue Scatter

8.1. Overview

Scatter observed in the fatigue response of a nickel-based superalloy, U720, is linked to the variability in the microstructure. In this chapter, we attempt to model fatigue scatter through the methodology presented in Chapters 6 and 7; fatigue life is predicted based on the energy of the PSB, which inherently accounts for the microstructure of the material. The present approach circumvents the introduction of uncertainty principles in material properties. It builds a framework based on mechanics of microstructure, and from this framework, we construct simulated microstructures based on the measured distributions of grain size, orientation, neighbor information, and grain boundary character, which allows us to calculate fatigue scatter using a deterministic approach. The uniqueness of the approach is that it avoids the large number of parameters prevalent in previous fatigue models. The predicted lives are in excellent agreement with the experimental data validating the model capabilities.

8.2. Establishing Simulated Microstructures

In the preceding chapters, we have presented a methodology for predicting fatigue crack initiation based on an energy balance, which exams each grain in the polycrystalline aggregate along with the formation of clusters, i.e. grains connected by LAGBs. In a sense, a weakest link is determined and cracks initiate from the PSB-GB interaction in this grain or grain cluster. From this methodology, fatigue life is tied to the energy of a critical PSB, which inherently

accounts for the microstructure of the material. By varying the microstructure, we can account for microstructurally driven fatigue scatter.

As previously mentioned, the attributes associated with the microstructure of the material were measured from EBSD scans of three specimens (forging, low $\Delta\varepsilon$ fatigue, and high $\Delta\varepsilon$ fatigue) and pooled together to establish representative distributions. The measured attributes are the grain size, grain orientation in terms of Schmid factor, number of adjacent grains, and CSL Σ value as shown in Figure 8.1. In Figure 8.1d, the character of the GBs are consolidated by the CSL Σ value, although in actuality we measure an axis-angle pair for each GB, which provides a more accurate representation of the boundary. Using the axis-angle description, we calculate the associated GB energy from MD simulations, as discussed in Chapter 4. Hence, an aggregate of 2000 grains was constructed, and for each grain, the grain size, grain orientation (Schmid factor), and number of GBs were selected randomly from the measured distributions (Figures 8.1a-c, respectively). Also, the neighbor information for each grain is randomly assigned and the GB character in terms of an axis-angle pair and its static interfacial energy is allocated from the measured distribution (Figure 8.1d) for the GB connecting the two adjacent grains in a self consistent manner.

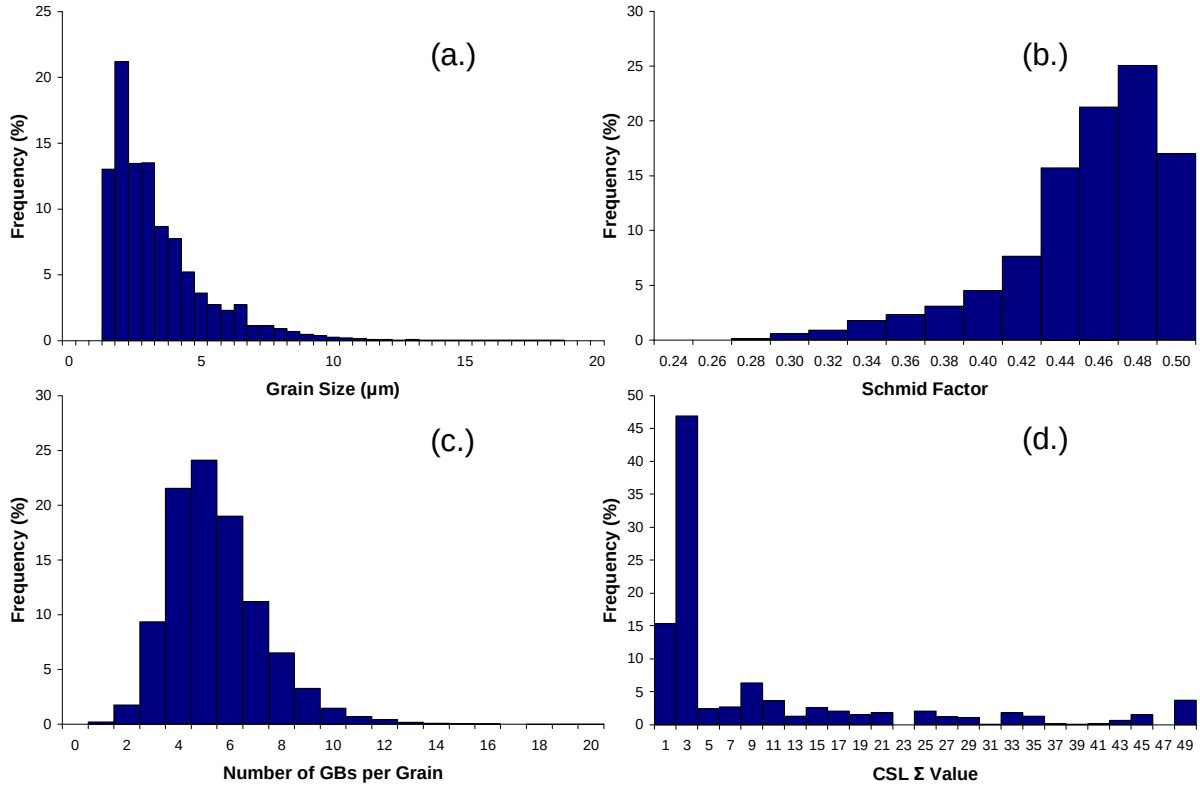

Figure 8.1. By pooling the EBSD results from three specimens, histograms are calculated of the: (a.) grain size, (b) Schmid factor, (c) number of GBs per grain, and (d.) GB character in terms of the CSL Σ values.

In order to assign the orientation of the neighboring grains, we first established these grains' Euler angles (selected at random from the measured distribution) and from this information, the CSL values were calculated. Although, as shown in Table 8.1, this methodology did a poor job in predicting the preferred low energy GBs, i.e. twins. This provides insight into an interesting question. With the large Brandon deviation associated with the Σ3 GB, do we automatically assume a large population of twins? The answer is no. Comparing a random texture (random Euler angles as seen in the EBSD scans) to a simulated random distribution of Euler angles, we see that there is a substantially different distribution of CSL values (Table 8.1). Hence, as we suspected, the microstructure (while still being randomly orientated) aligns to a low energy CSL configuration.

Table 8.1. Percentage (relative to the total number of CSL boundaries) of the LAGBs and TBs measured from EBSD (averaged over 3 specimens) and simulated from distributions using the Euler angles or axis-angle pair information.

	Measured from EBSD	Simulated from Euler Angles	Simulated from Axis/Angle Pair
Percentage of LAGBs	15.4%	13.8%	15.0%
Percentage of Twins	46.8%	17.0%	46.9%

Thus, attributes are randomly assigned for each grain in the polycrystal to create a 'simulated specimen', as shown in Figure 8.2. We repeat this process to generate 1000 specimens, which accounts for the variability in the material based within the observed ranges of microstructural features. For each specimen, the microstructure is simulated, grains/clusters most likely to fail are identified, and the cycles to crack initiation is predicted for a series of six applied strain ranges. Hence, the aforementioned code takes ~28.2 seconds to run for each specimen on a standard desktop computer, thus offering substantial computational savings as opposed to other microstructurally driven fatigue software.

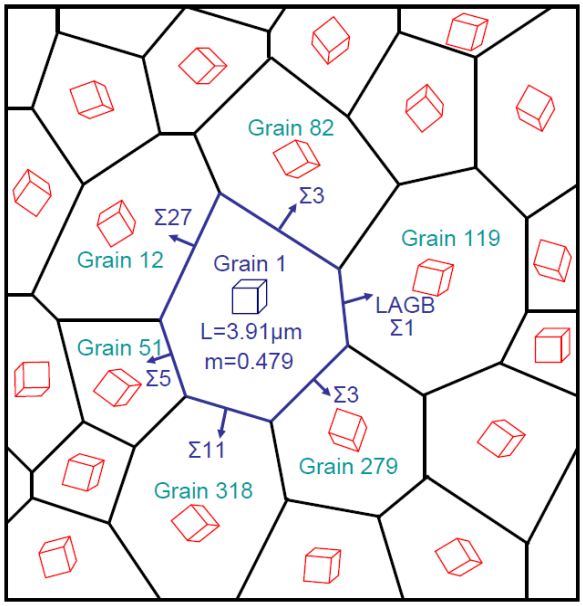

Figure 8.2. Schematic of a reconstructed microstructure for a simulated specimen. For each grain, the size, orientation, number of GBs, and associated GB character is selected randomly from the distributions in Figure 8.1; afterwards, the nearest neighbors are assigned.

8.3. Monte Carlo Results and Discussion

For each of the 1000 simulated specimens, the fatigue life in terms of cycles to crack initiation is predicted using the methodology outlined in Section 7.3. The results are shown in Figure 8.3 (1000 model predictions – red diamonds compared to 84 experiments – blue triangles) and Table 8.2. Based on these results, we can conclude that by varying the microstructure, the model accurately accounts for the fatigue scatter. For each strain range, the averages of the predicted results and experiments are nearly identical, further the minimum and maximum values are in excellent agreement.

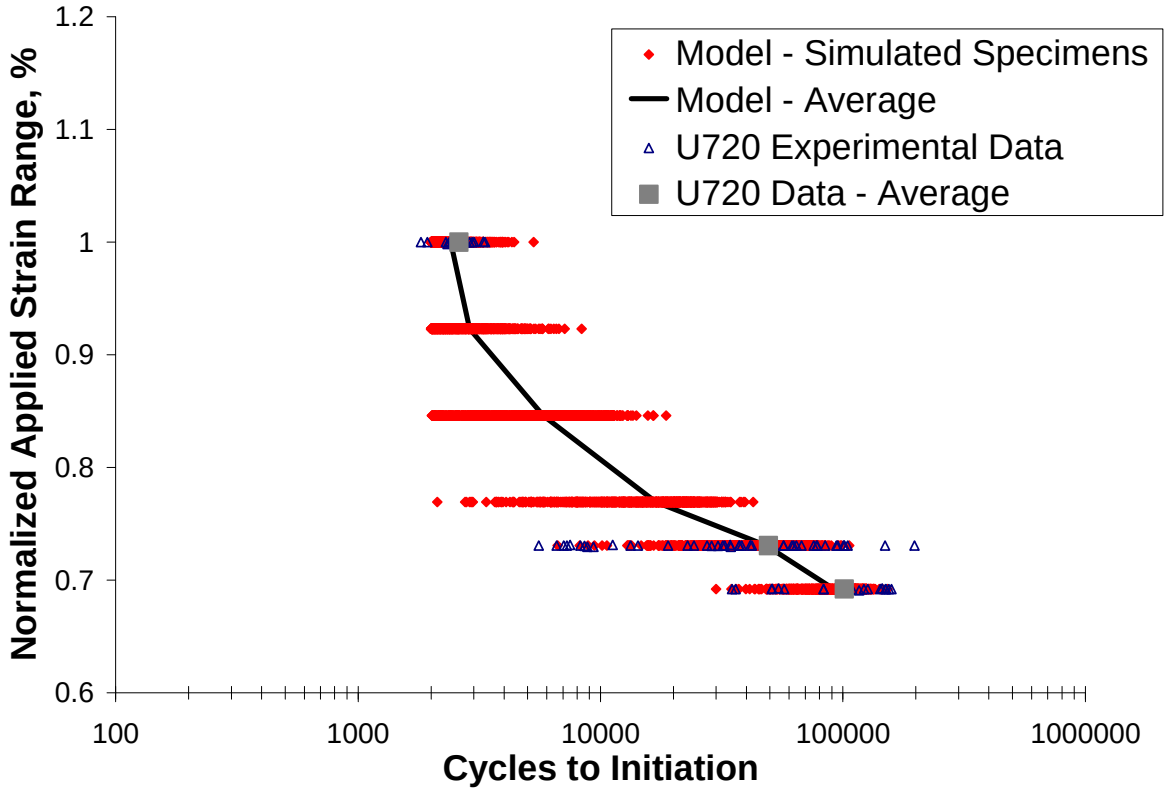

Figure 8.3. Predicted fatigue results for 1000 simulated specimens at each strain range compared to specimen from 84 fatigue experiments. The individual specimens as well as the averages provide good agreement between model predictions and experimental results. Please note that the applied strain ranges are normalized values.

Table 8.2. Model predicted fatigue results in terms of number of cycles until crack initiation for 1,000 simulated specimens at a series of normalized applied strain ranges.

Strain Range	Average	Standard Deviation	Log Average	Log Standard Deviation	Maximum	Minimum	Number of Data Points
1.00	2,410	419	2,379	342	5,297	2,003	1,000
0.92	2,886	812	2,792	615	8,372	2,003	1,000
0.85	5,794	2,674	5,193	1,974	18,616	2,018	1,000
0.77	16,914	7,097	15,178	5,981	42,667	2,121	1,000
0.73	48,348	17,034	44,889	15,108	105,980	6,654	1,000
0.69	91,861	20,447	89,367	19,248	152,630	30,024	1,000

Within a given specimen, it was previously shown in Section 7.4 that the grain cluster most likely to fail is dependent on the applied strain range. In other words, based on the loading magnitude, we see different terms dominate the energy balance (Equation 6.1) resulting in crack initiation occurring in a different combination of microstructure features. Hence, for the 1000 simulated specimens, modeled at six applied strain ranges, we have 6000 possible failure locations from individual grains or grain clusters, which allows us to analyze the statistics of the predicted locations likely to initiate cracks.

The vast majority (96%) of the cracks initiate due to PSB interaction with a twin boundary, as shown in Figure 8.4a, which is in agreement with experimental observations [207, 218-223] and Figures 3.8b,c as twins are evident within the facets of failed U720 specimens. As shown in Figure 5.7, the $\Sigma 3$ twin boundary exhibits the highest energy barrier for slip transmission. Thus, dislocation motion is impeded by twins resulting in pile-ups. To alleviate the high energy and stress concentration caused by the pile-ups, the material forms a crack in the vicinity of the twin. Hence, we experience cracking near twin boundaries in our simulations, as a consequence of the high associated energy barrier coupled with the large percentage of annealing twins within this material (Figure 8.1d). Additionally, the PSB preceding crack initiation occurs in a single large grain (Figure 7.7a) 55% of the time as shown in Figure 8.4b. In

the remaining simulations, PSBs spanning multiple adjacent grains connected by LAGBs (Figure 7.7b) initiate cracks, although these grain clusters are most likely to be comprised of only two (30.9%) or three (10.9%) grains. Seven grains constituted the largest predicted cluster, albeit this was an isolated and rare case.

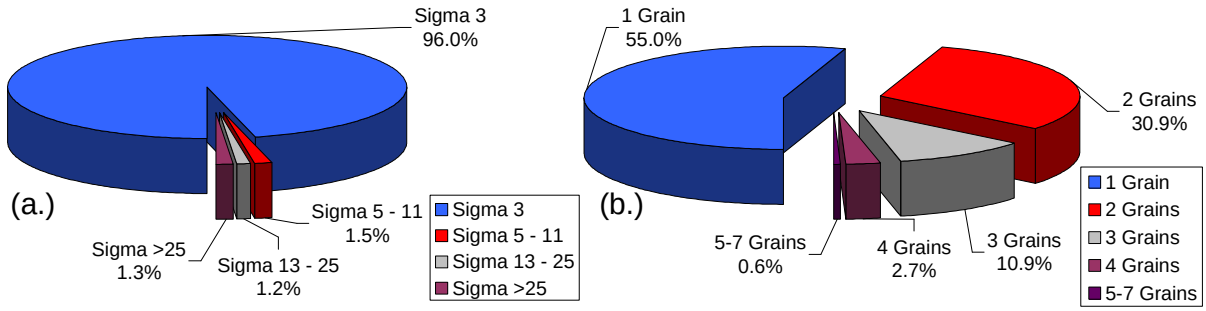

Figure 8.4. From the 1000 simulated specimens at each strain range, the grain cluster, in which a crack was predicted to initiate, is analyzed. (a.) Cracks initiated due to PSB-GB interaction, thus the distribution of GB Σ character resulting in crack formation is shown. As expected, the model predicts that most cracks initiate in the vicinity of Σ3 GBs, i.e. twins. (b.) The distribution of number of grains within the grain cluster most likely to fail.

Further, the size of the simulated grain clusters initiating cracks are analyzed and compared with the experimental distributions of grain size and facet size, as shown in Figure 8.5. We see the size of the problematic grain clusters is in the range of 7.7 μm to 21.2 μm. Hence, this range is on the tail end of the measured grain size. Thus, in the cases where the grain cluster is comprised of a single grain (55%), these grains are amongst the largest size in the measured population. Also, the cluster size distribution approaches the facet sizes (15 μm to 135 μm) measured from the fracture surfaces of 89 failed fatigue experiments. We would expect to see larger grain clusters, which mimic the facet size, if the EBSD scans encompassed a greater area or the simulated specimens contain a greater number of grains. As previously discussed in Section 7.4, the facet length also encompasses short crack growth, hence it is not a good indicator of PSB length leading to crack initiation.

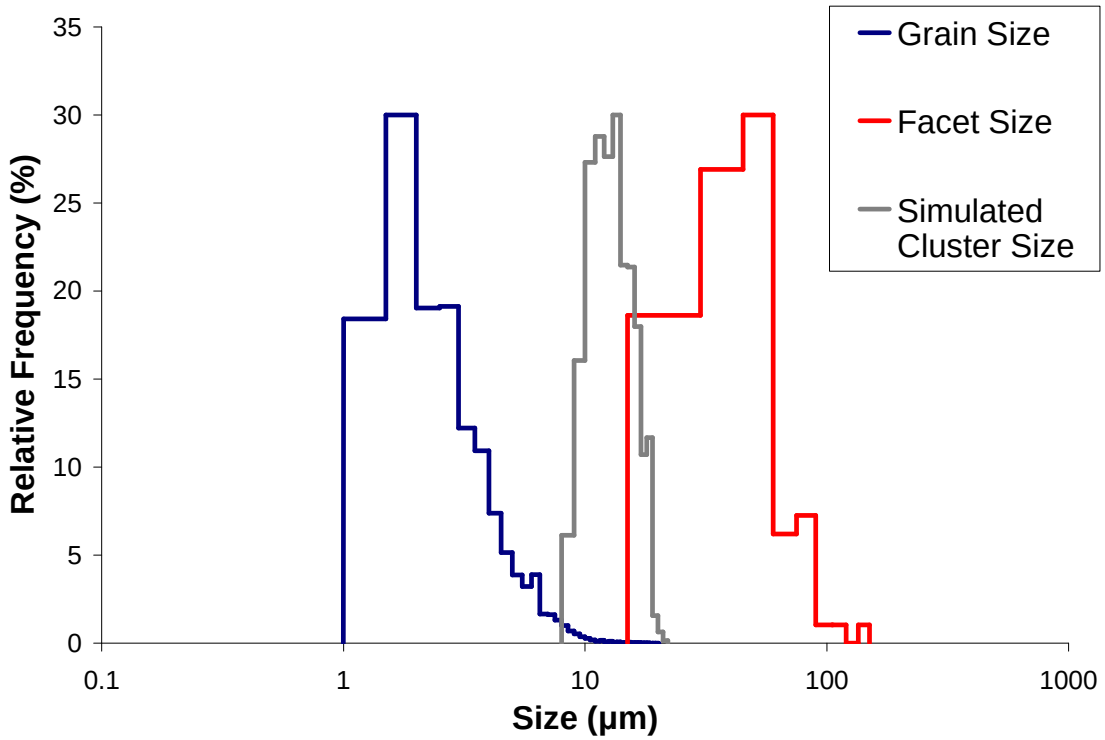

Figure 8.5. Histogram comparisons for the grain size measured from EBSD of the three pooled specimens, the facet size measured from SEM images of 89 failed fatigue specimens, and the size of the simulated grain cluster most likely to initiate a crack from a PSB.

As previously discussed, many contributing microstructural variables (i.e. grain orientation, grain size, GB character, γ' precipitate density, and neighboring grains) affect the fatigue life. We investigated the correlation between each of these parameters to the predicted life; the results showed that the grain size dependency is best correlated to the fatigue life. As shown in Figure 8.6, for each of the 1000 simulated specimens (at 0.73% applied strain), the predicted fatigue life is shown as a function of the size of the grain or cluster of grains most likely to initiate a crack. When the microstructure's weakest link is composed of a larger grain, a shorter fatigue life is observed. The data is split into three categories, single grain failures (55%), clusters consisting of two grains (30.9%), and clusters consisting of three or more grains (14.1%). From these data sets, a regression analysis was performed. On average, clusters composed of a greater number of grains have a shorter fatigue life for a given cluster size. Of

course, the data does not collapse to a single line since many other factors play a role in predicting fatigue life. Further, in Figure 8.6, the gray dashed line represents the minimum predicted fatigue life based on the critical grain size within the distribution. This type of curve can be used for design purposes as microstructures are typically inspected for ALA (as large as) grains. The fatigue life can be simply forecasted from this curve in a conservative manner (since, in general, ALA grains are not necessarily the weakest link), while more accurate predictions can be determined when factoring in the other microstructural parameters into the fatigue model. It should be noted that Equation 7.3 was introduced to improve computational efficiency and a cutoff grain size is introduced, as shown by the vertical gray dotted line.

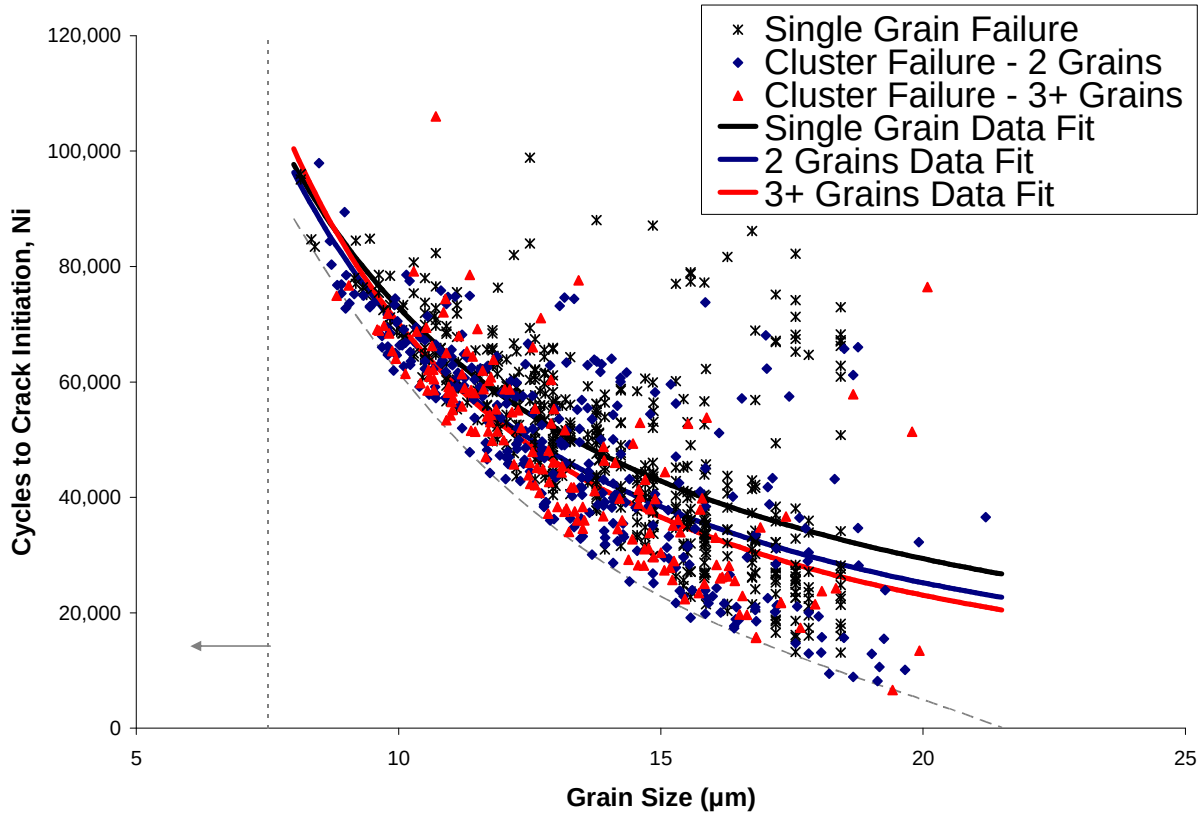

Figure 8.6. Results of 1000 simulated specimens at 0.73% (normalized) applied total strain range. The predicted fatigue life is plotted against the size of the individual grain or cluster of grains most likely to initiate a crack in each simulated specimen. The data is separated into the number of grains causing failure and best fit lines are drawn for each group. The dashed gray line represents the minimum fatigue life for a given grain size, which may be used for design purposes. The vertical dotted gray line represents the outcome of Equation 7.3, which does not affect the results of this model.

In essence, this model identifies the weakest link in the microstructure, which ultimately results in crack nucleation. The nature of weakest link models is that with increased sampling of grains, the probability of finding a detrimental grain cluster increases. Changing the representative volume element (RVE, i.e. number of grains in our simulated microstructure) results in a shift of the predicted fatigue response, thus displaying lower lives, as shown in Figure 8.7 for 100 simulated specimens at each RVE size: 1000, 2000, 3000, and 4000. In other words, by increasing the number of grains or RVE, we increase the probability of finding a larger weakest link in the microstructure and effectively lower the fatigue life of the simulated specimen. Of course, the RVE size is a function of the microstructure, which in the present case is characterized by EBSD scans of 3 specimens (containing 2373, 3664, and 7424 grains). Therefore, our pooled distributions are comprised of 13,461 grains, hence choosing a RVE size of 2000 grains represent a substantial subset of each EBSD scan, while still addressing computational efficiency.

In general, fatigue modeling, especially in the presence of scatter, has not been based on a physics of solids approach. Hence the present study addresses this need as a model is developed based on the microstructure of the material. Our model displays excellent agreement between predicted fatigue scatter and experimental results; thus providing a powerful tool demonstrating predictive capabilities.

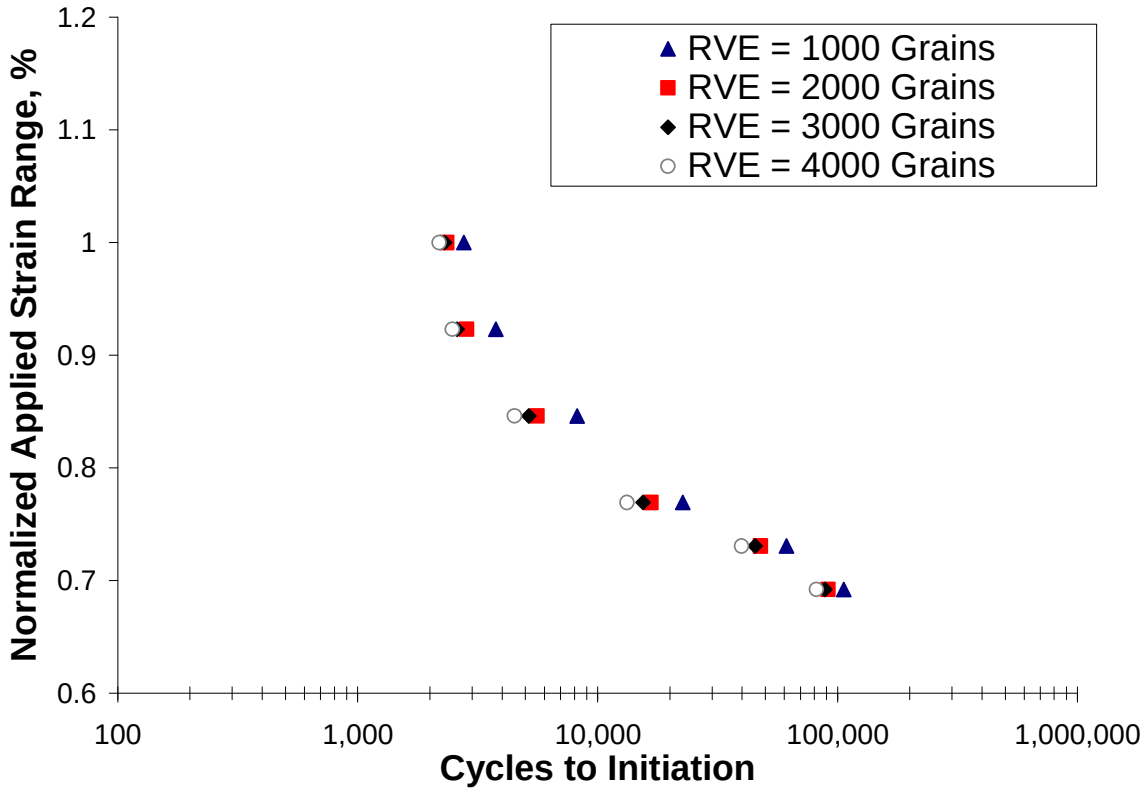

Figure 8.7. Predicted fatigue results in terms of average life for 100 specimens. This plot displays the effect of the number of grains within the simulated microstructure, i.e. representative volume element, on the predicted values of cycles to initiation. As expected, more grains increase the probability of finding a weakest link and early failure. Please note that the applied strain ranges are normalized values.

8.4. Summary

This study represents a substantial effort in the field of physically-based fatigue scatter modeling. The major contributions are as follows:

- EBSD scans were completed on three specimens and pooled together to obtain distributions of the representative grain size, orientation (Schmid factor), number of adjacent grains, and GB character in terms of an axis-angle pair with a corresponding GB energy. From this data, simulated microstructures were generated by randomly assigning attributes to the grains from the measured distributions. Using our fatigue analysis software, the fatigue life was predicted

on each of these simulated specimens and compared with experimental results, which displayed excellent agreement both in terms of scatter and average values.

- From the thousands of simulated specimens, we can conclude single large grains are most likely to form cracks. Although two or three grains connected by LAGBs were a significant source of crack initiation; also in one rare case, a crack initiated from a grain cluster comprised of seven grains.
- In nearly all the simulated specimens, the cracks initiated near a twin boundary, corresponding to experimental observations. This is established in our model as twin boundaries possess the highest energy barrier for slip transmission. Thus, the PSB-GB interactions resulted in dislocation pile-up, stress concentration, an increase in energy, and crack initiation.

Chapter 9. Conclusions and Recommendations

9.1. Conclusions

The aim of this research was to understand the role of grain boundaries on the fatigue life of a nickel-based superalloy, U720. In doing so, we wanted to use this information to service a fundamental model to predict fatigue crack initiation based on the material's microstructure. The goal of this model was to reduce the large number of fitting parameters or constants prevalent in other fatigue models and rely primarily on physical approaches. From this point, we wanted to quantify fatigue scatter in a deterministic framework, which attributed microstructure variability to fatigue scatter. The preceding work was presented in a sequential manner in an attempt to address each of the aforementioned objectives. The research contribution of each chapter is summarized as follows:

In Chapter 4, the grain boundaries of U720 were characterized via EBSD scans. We chose to utilize a CSL framework, in order to express the GBs in a mathematical context. The evolution of the CSL has been shown for various stages of processing (billet and forging) and deformation (tension, compression, and fatigue). Fatigue testing has little effect on the CSL distribution. In each of the specimens, the $\Sigma 3$ GBs were prevalent, and it was shown that these represent coherent annealing twins. To gain a deeper understanding of GBs, the energies of the CSL GBs were measured using MD, while the Read-Shockley model was used to calculate low-angle GBs. The lowest energy configuration was observed for the coherent $\Sigma 3$ twin GB, which explains its abundance in the measured EBSD analysis. A link was made between the calculated energies and the EBSD measurements of grain orientation and size. A strong inverse correlation exists between grain boundary energy and grain size for each specimen. The rationale behind

this stems from larger grains exhibiting a greater twin density, more mobility to reorient the GB normal during heat treatment, and less GB curvature.

In Chapter 5, we investigated the mechanical response of GBs using MD simulations to study the slip-GB interactions including strain transmission and dislocation nucleation at a GB. The aim of this work was to quantify the strengthening mechanisms of individual GBs. In order to do so, a control box was placed around the defect atoms during slip-GB interactions to measure the energy barriers. This methodology was validated by comparisons to the generalized stacking fault energy. The energy barriers to slip transmission and dislocation nucleation are calculated across various classifications of GBs: <110> tilt – Σ3, 9, 11, 17, 19; <111> twist – Σ3, 7, 13, 21; and <001> tilt – Σ5. The coherent twin (Σ3) boundary provides the highest barrier for slip transmission. The energy barrier from the slip-GB interaction is significantly affected by the character and the structure of the GB, as there is a strong correlation between the energy barrier and interfacial boundary energy. GBs with lower static interfacial energy offer a stronger barrier against slip transmission and nucleation at the GB.

In Chapter 6, we presented the framework for a physically-based fatigue model. This model analyzed the PSB energy within a grain in a polycrystal, which was most likely to initiate a crack. The contributing elements to the energy of the PSB were identified. In order for plastic deformation to occur within the PSB, a dislocation must glide within a stress field established by the dislocation pile-up, work-hardening of the material, and applied stress. Additionally, the energy barriers for dislocations to nucleate from and penetrate a GB were determined from MD simulations. These MD contributions serviced our model as the γ matrix/γ' precipitates were sheared, dislocations nucleated/collected within the PSB, and extrusions formed at the intersection of the PSB and GB. The aforementioned terms were expressed in an energy balance

for the total energy of the PSB, which evolved with increasing fatigue cycles. Stability of the PSB corresponded to a minimum value of the energy balance, which was computed as the derivative of the total PSB energy with respect to plastic deformation (i.e. an increment of slip) reaching zero, which is consistent with other historical energy balance approaches.

In Chapter 7, the previous fatigue model was extended to predict crack initiation in polycrystalline material based on EBSD scans of the microstructure. This is accomplished by allowing PSBs to traverse LAGBs, thus linking grains together to form grain clusters. In doing so, we account for groups of grains, which are likely to fail and thus modify the energy balance appropriately. The model was validated by simulating the fatigue life of three EBSD scans, which were in very good agreement with the experimental data. The simulated crack initiation sites constituted a range of grain sizes and contained various numbers of grains within a cluster. Further, the cracks initiated near a twin boundary, corresponding with experimental observations. The rationale behind this was the high energy barriers for slip-GB interactions for a TB. Thus, the PSB-GB interactions resulted in dislocation pile-up, stress concentration, an increase in energy, and crack initiation. Additionally, we see that at various applied strain ranges, different mechanisms or terms within the energy balance dominated failure, resulting in various grain clusters representing the weakest link.

In Chapter 8, simulated microstructures were generated by randomly assigning attributes to the grains from the measured distributions of grain size, orientation (Schmid factor), number of adjacent grains, and GB character in terms of an axis-angle pair with a corresponding GB energy. Using our fatigue analysis software, the fatigue life was predicted on each of these simulated specimens and compared with experimental results, which displayed excellent agreement both in terms of scatter and average values. From the thousands of simulated

specimens, we can conclude single large grains are most likely to form cracks. Although two or three grains connected by LAGBs were a significant source of crack initiation. In nearly all the simulated specimens, the cracks initiated near a twin boundary, corresponding to the experimental observations.

For completeness, we began this project with an objective of answering the following questions. In doing so, we successfully created a model, which can quickly quantify the fatigue life and scatter of a material based on an EBSD scan. From the knowledge that we have gained throughout this project, we are in a prime position to now address these questions:

- *Can we determine a criterion for crack initiation in U720?* An energy balance was calculated based on the energy of a PSB. Crack initiation was defined based on the stability of the PSB (minimum energy) with respect to plastic deformation.
- *How do mis-oriented grains affect the fatigue properties?* LAGBs allow PSB transmission resulting in grain clusters. Also, TBs result in pile-ups and are preferred sites for crack initiation (but also have many beneficial features as well).
- *How does grain size distribution and adjacent small/large grains within a polycrystalline material affect fatigue life?* Large grains are detrimental to fatigue life, although there are many other factors (neighboring grains, GB character, grain orientation) that play a role in crack initiation.
- *Can we account for fatigue scatter?* Yes, we can account for fatigue scatter solely on the material's microstructure.

9.2. Recommendations

In this study, we have modeled the fatigue response of a nickel-based superalloy with an emphasis on GBs. We have made every attempt to make this model physically-based and reliant on a simple energy balance. As a consequence, this model should be easily amendable to account for additional phenomenon. In order to increase the accuracy of this model, enhance our understanding of GB's affect on fatigue, or simply extend this model's applications, we propose the following as future work:

1. Measure the energy barriers from MD simulations for additional GB configurations (including asymmetric type) observed in the U720 microstructure.
2. In the MD simulations, add defects to the neighboring grain or at the GBs (such as vacancies or ledges/steps) to better represent real microstructures and observe the variation in the energy barriers for dislocations to penetrate the GB.
3. Using ab initio techniques, add $M_{23}C_6$ particles to the GBs, to investigate the effects of carbides on the GB energy and strain incompatibility.
4. Apply dislocation dynamics to investigate PSB-PSB interactions, which is of interest for accurately predicting multiple crack initiation for high applied $\Delta\varepsilon$.
5. Measure the GB characters using 3D FIB-EBSD techniques, which will allow us to validate our minimum energy assumption in Chapter 4.
6. Experimentally measure the PSB dislocation density and extrusion height evolution for U720. The extrusion height can be measured for various types of CSL GBs in a bicrystal using in situ TEM analysis and optical measurement of the extrusion height.

7. Develop methodology for cases where the crack initiation mechanism is not from PSBs. In these cases, the dislocation configuration is the energy formulation needs modification.
8. The fatigue model can be amended to account for mean stresses, i.e. various R-ratios, by incorporating normal forces on the GSFE and APBE curves.
9. In this energy based analysis, we essentially calculate the critical resolved shear stress on the microstructure. Hence, we can extend this methodology to predict multi-axial fatigue.
10. By varying the temperature in the MD analysis and preliminary experiments (to determine the evolution functions for dislocation density, extrusion height, PSB height, and applied stress), we can model the fatigue response at various isothermal conditions.
11. In our MD analysis, we model slip transmission through a GB. If we were to unload the simulation and measure the slip irreversibility at the GB, we could extend this methodology to study fatigue crack growth. The experimental characterization and energy balance approach can be applied to this phenomenon.
12. In certain nickel-based superalloys, cube slip is observed through the γ' at elevated temperature. We can calculate the APB energy for cube slip and add this to our energy balance.
13. A future application of this model is to apply it to a process modeling code such as Deform^{TM}. This code enables one to predict the microstructure during a forging process. Hence, through reverse engineering, this would allow us to optimize the forging process to deliver a microstructure with enhanced fatigue life. In doing so, the geometry of a turbine disk could be designed for longer life.

14. By implementing this energy balance code into a finite element-crystal plasticity framework, we can determine the fatigue life of an entire component based on the spatial stress distribution and local microstructure. Thus, a weakest link could be determined at the component level to predict crack initiation.

References

[1] Hirth JP. The influence of grain boundaries on mechanical properties. Metallurgical Transactions A (Physical Metallurgy and Materials Science) 1972;3:3047.
[2] Hall EO. The deformation and ageing of mild steel III. Discussion of results. Proceedings of the Physical Society. Section B 1951;64:747.
[3] Petch NJ. Cleavage strength of polycrystals. Iron and Steel 1953;26:601.
[4] Ashby MF. The deformation of plastically non-homogeneous materials. Philosophical Magazine 1970;21:399.
[5] Li JCM, Chou YT. Role of dislocations in the flow stress grain size relationships. Metallurgical Transactions 1970;1:1145.
[6] Curry DA, Knott JF. The relationship between fracture toughness and microstructure in the cleavage fracture of mild steel. Metal Science 1976;10:1.
[7] Curry A, Knott JF. Effects of microstructure on cleavage fracture stress in steel. Metal Science 1978;12:511.
[8] Sinclair GM, Craig WJ. Influence of Grain Size on Work Hardening and Fatigue Characteristics of Alpha Brass. Reprint: Influence of Grain Size on Work Hardening and Fatigue Characteristics of Alpha Brass. United States, 1952. p.18.
[9] Thompson AW. The comparison of yield and fatigue strength dependence on grain size. Scripta Metallurgica 1971;5:859.
[10] Thompson AW, Backofen WA. The effect of grain size of fatigue. Acta Metallurgica 1971;19:597.
[11] Thompson AW, Backofen WA. Production and mechanical behavior of very fine-grained copper. Metallurgical and Materials Transactions A (Physical Metallurgy and Materials Science) 1971;2:2004.
[12] Lukas P, Kunz L. Effect of grain size on the high cycle fatigue behavior of polycrystalline copper. Materials Science and Engineering 1987;85:67.
[13] Morrison DJ, Moosbrugger JC. Effects of grain size on cyclic plasticity and fatigue crack initiation in nickel. International Journal of Fatigue 1997;19:S51.
[14] Liu HW. Dislocation barrier model for fatigue limit - as determined by crack non-initiation and crack non-propagation. International Journal of Fracture 1999;96:331.
[15] Berbenni S, Favier V, Berveiller M. Impact of the grain size distribution on the yield stress of heterogeneous materials. International Journal of Plasticity 2007;23:114.
[16] Kronberg ML, Wilson FH. Secondary recrystallization in copper. American Institute of Mining and Metallurgical Engineers - Journal of Metals 1949;1:501.
[17] Lim LC. Surface intergranular cracking in large strain fatigue. Acta Metallurgica 1987;35:1653.
[18] Pan Y, Adams BL, Olson T, Panayotou N. Grain-boundary structure effects on intergranular stress corrosion cracking of Alloy X-750. Acta Materialia 1996;44:4685.
[19] Field DP, Adams BL. Interface cavitation damage in polycrystalline copper. Acta Metallurgica et Materialia 1992;40:1145.
[20] Yang SL, Krupp U, Christ HJ, Trindade VB. The relationship between grain boundary character and the intergranular oxide distribution in IN718 superalloy. Advanced Engineering Materials 2005;7:723.

[21] Zhang ZF, Wang ZG. Comparison of fatigue cracking possibility along large- and low-angle grain boundaries. Materials Science and Engineering A (Structural Materials: Properties, Microstructure and Processing) 2000;A284:285.
[22] Read WT, Shockley W. Dislocation models of crystal grain boundaries. Physical Review 1950;78:275.
[23] Li JCM. Some elastic properties of an edge dislocation wall. Acta Metallurgica 1960;8:563.
[24] Li JCM, Chalmers B. Energy of a wall of extended dislocations. Acta Metallurgica 1963;11:243.
[25] Li JCM. High-angle tilt boundary-A dislocation core model. Journal of Applied Physics 1961;32:525.
[26] Brandon DG. The structure of high-angle grain boundaries. Acta Metallurgica 1966;14:1479.
[27] Kaneko Y, Kitagawa K, Hashimoto S. Fatigue crack propagation in copper bicrystals having the grain boundaries of Σ3 vicinal domain. Interface Science 1999;7:147.
[28] Palumbo G, Aust KT. Structure-dependence of intergranular corrosion in high purity nickel. Acta Metallurgica et Materialia 1990;38:2343.
[29] Frary M, Schuh CA. Combination rule for deviant CSL grain boundaries at triple junctions. Acta Materialia 2003;51:3731.
[30] Watanabe T. Approach to grain boundary design for strong and ductile polycrystals. Res Mechanica: International Journal of Structural Mechanics and Materials Science 1984;11:47.
[31] Watanabe T. Grain Boundary Design for the Control of Intergranular Fracture. Material Science Forum 1989;46:25.
[32] Aust KT, Erb U, Palumbo G. Interface control for resistance to intergranular cracking. Materials Science and Engineering A 1994;A176:329.
[33] Shvindlerman LS, Gottstein G. Unexplored topics and potentials of grain boundary engineering. Scripta Materialia 2006;54:1041.
[34] Brandon DG, Ralph B, Ranganathan S, Wald MS. Field ion microscope study of atomic configuration at grain boundaries. Acta Metallurgica 1964;12:813.
[35] Ranganathan S. On the geometry of coincidence-site lattices. Acta Crystallographica 1966;21:197.
[36] Acton AF, Bevis M. The geometry of coincidence-site lattices. Acta Crystallographica, Section A (Crystal Physics, Diffraction, Theoretical and General Crystallography) 1971;A27:175.
[37] Santoro A, Mighell AD. Coincidence-site lattices. Acta Crystallographica, Section A (Crystal Physics, Diffraction, Theoretical and General Crystallography) 1973;A29:169.
[38] Grimmer H, Bollmann W, Warrington DH. Coincidence-site lattices and complete pattern-shift lattices in cubic crystals. Acta Crystallographica, Section A (Crystal Physics, Diffraction, Theoretical and General Crystallography) 1974;A30:197.
[39] Grimmer H. Disorientations and coincidence rotations for cubic lattices. Acta Crystallographica, Section A (Crystal Physics, Diffraction, Theoretical and General Crystallography) 1974;A30:685.
[40] Grimmer H. Coincidence-site lattices. Acta Crystallographica, Section A (Crystal Physics, Diffraction, Theoretical and General Crystallography) 1976;A32:783.

[41] Grimmer H. The generating function for coincidence site lattices in the cubic system. Acta Crystallographica, Section A (Foundations of Crystallography) 1984;A40:108.
[42] Sutton AP, Vitek V. On the structure of tilt grain boundaries in cubic metals. I. Symmetrical tilt boundaries. Philosophical Transactions of the Royal Society of London A (Mathematical and Physical Sciences) 1983;309:1.
[43] Sutton AP, Vitek V. On the structure of tilt grain boundaries in cubic metals. II. Asymmetrical tilt boundaries. Philosophical Transactions of the Royal Society of London A (Mathematical and Physical Sciences) 1983;309:37.
[44] Sutton AP, Vitek V. On the structure of tilt grain boundaries in cubic metals. III. Generalizations of the structural study and implications for the properties of grain boundaries. Philosophical Transactions of the Royal Society of London A (Mathematical and Physical Sciences) 1983;309:55.
[45] Wang GJ, Sutton AP, Vitek V. Computer simulation study of <001> direction and <111> direction tilt boundaries: the multiplicity of structures. Acta Metallurgica 1984;32:1093.
[46] Wang G, Vitek V. Relationships between grain boundary structure and energy. Acta Metallurgica 1986;34:951.
[47] Balluffi RW, Bristowe PD. On the structural unit/grain boundary dislocation model for grain boundary structure. Surface Science 1984;144:28.
[48] Randle V. The coincidence site lattice and the 'sigma enigma'. Materials Characterization 2001;47:411.
[49] Randle V. Application of electron backscatter diffraction to grain boundary characterisation. International Materials Reviews 2004;49:1.
[50] Randle V. Overview No. 127: The role of the grain boundary plane in cubic polycrystals. Acta Materialia 1998;46:1459.
[51] Randle V, Davies P. Deviation from reference planes and reference misorientation for Σ3 boundaries. Interface Science 1999;7:5.
[52] Randle V. Asymmetric tilt boundaries in polycrystalline nickel. Acta Crystallographica, Section A (Foundations of Crystallography) 1994;A50:588.
[53] Randle V. Sigma-boundary statistics by length and number. Interface Science 2002;10:271.
[54] Randle V, Davies P, Hulm B. Grain-boundary plane reorientation in copper. Philosophical Magazine A (Physics of Condensed Matter: Structure, Defects and Mechanical Properties) 1999;79:305.
[55] Saylor DM, Morawiec A, Rohrer GS. Distribution of grain boundaries in magnesia as a function of five macroscopic parameters. Acta Materialia 2003;51:3663.
[56] Saylor DM, El-Dasher BS, Adams BL, Rohrer GS. Measuring the five-parameter grain-boundary distribution from observations of planar sections. Metallurgical and Materials Transactions A (Physical Metallurgy and Materials Science) 2004;35A:1981.
[57] Rohrer GS, El Dasher BS, Miller HM, Rollett AD, Saylor DM. Distribution of grain boundary planes at coincident site lattice misorientations. vol. 819. San Francisco, CA, United states: Proc. of Materials Research Society, 2004. p.265.
[58] Li J, Dillon SJ, Rohrer GS. Relative grain boundary area and energy distributions in nickel. Acta Materialia 2009;57:4304.
[59] Bhandari Y, Sarkar S, Groeber M, Uchic MD, Dimiduk DM, Ghosh S. 3D polycrystalline microstructure reconstruction from FIB generated serial sections for FE analysis. Computational Materials Science 2007;41:222.

[60] Ghosh S, Bhandari Y, Groeber M. CAD-based reconstruction of 3D polycrystalline alloy microstructures from FIB generated serial sections. CAD Computer Aided Design 2008;40:293.
[61] Wolf D. Structure-energy correlation for grain boundaries in FCC metals. I. Boundaries on the (111) and (100) planes. Acta Metallurgica 1989;37:1983.
[62] Wolf D. Structure-energy correlation for grain boundaries in FCC metals. II. Boundaries on the (110) and (113) planes. Acta Metallurgica 1989;37:2823.
[63] Wolf D. Structure-energy correlation for grain boundaries in f.c.c. metals. III. Symmetrical tilt boundaries. Acta Metallurgica et Materialia 1990;38:781.
[64] Wolf D. Structure-energy correlation for grain boundaries in FCC metals. IV. Asymmetrical twist (general) boundaries. Acta Metallurgica et Materialia 1990;38:791.
[65] Rittner JD, Seidman DN. <110> symmetric tilt grain-boundary structures in fcc metals with low stacking-fault energies. Physical Review B (Condensed Matter) 1996;54:6999.
[66] Olmsted DL, Foiles SM, Holm EA. Survey of computed grain boundary properties in face-centered cubic metals: I. Grain boundary energy. Acta Materialia 2009;57:3694.
[67] Olmsted DL, Holm EA, Foiles SM. Survey of computed grain boundary properties in face-centered cubic metals-II: Grain boundary mobility. Acta Materialia 2009;57:3704.
[68] Kashihara K, Inoko F. Effect of piled-up dislocations on strain induced boundary migration (SIBM) in deformed aluminum bicrystals with originally Σ3 twin boundary. Acta Materialia 2001;49:3051.
[69] Livingston JD, Chalmers B. Multiple slip in bicrystal deformation. Acta Metallurgica 1957;5:322.
[70] Shen Z, Wagoner RH, Clark WAT. Dislocation pile-up and grain boundary interactions in 304 stainless steel. Scripta Metallurgica 1986;20:921.
[71] Lee TC, Robertson IM, Birnbaum HK. Prediction of slip transfer mechanisms across grain boundaries. Scripta Metallurgica 1989;23:799.
[72] El-Dasher BS, Adams BL, Rollett AD. Viewpoint: Experimental recovery of geometrically necessary dislocation density in polycrystals. Scripta Materialia 2003;48:141.
[73] Hirth JP, Lothe J. Theory of Dislocations: Wiley Interscience, New York, 1992.
[74] Sutton AP, Balluffi RW. Interfaces in Crystalline Materials: Oxford Classical Texts, 2006.
[75] Seeger A. Stacking Faults in Close-Packed Lattices. Defects in Crystalline Solids. Bristol, UK: The Physical Society, 1954. p.328.
[76] Seeger A, Schoeck G. Activation Energy Problems associated with Extended Dislocations. Defects in Crystalline Solids. Bristol, UK: The Physical Society, 1954. p.328.
[77] Conrad H. The athermal component of the flow stress in crystalline solids. Material Science and Engineering 1970;6:265.
[78] Kocks UF, Argon AS, Ashby MF. Thermodynamics and Kinetics of Slip: Pergamon Press, Oxford, 1975.
[79] Kocks UF, Tome CN, Wenk H-R. Texture and Anisotropy: Cambridge University Press, 2000.
[80] Kocks UF, Mecking H. Physics and phenomenology of strain hardening: The FCC case. Progress in Materials Science 2003;48.

[81] Fang H, Horstemeyer MF, Baskes MI, Solanki K. Atomistic simulations of Bauschinger effects of metals with high angle and low angle grain boundaries. Computer Methods in Applied Mechanics and Engineering 2004;193:1789.
[82] Spearot DE, Tschopp MA, Jacob KI, McDowell DL. Tensile strength of <100> and <110> tilt bicrystal copper interfaces. Acta Materialia 2007;55:705.
[83] Yamakov V, Wolf D, Salazar M, Phillpot SR, Gleiter H. Length-scale effects in the nucleation of extended dislocations in nanocrystalline Al by molecular-dynamics simulation. Acta Materialia 2001;49:2713.
[84] Yamakov V, Wolf D, Phillpot SR, Mukherjee AK, Gleiter H. Deformation-mechanism map for nanocrystalline metals by molecular-dynamics simulation. Nature Materials 2004;3:43.
[85] Van Swygenhoven H. Grain boundaries and dislocations. Science 2002;296:66.
[86] Van Swygenhoven H, Caro A, Farkas D. A molecular dynamics study of polycrystalline fcc metals at the nanoscale: Grain boundary structure and its influence on plastic deformation. Materials Science and Engineering A 2001;309-310:440.
[87] Froseth AG, Derlet PM, Van Swygenhoven H. Dislocations emitted from nanocrystalline grain boundaries: nucleation and splitting distance. Acta Materialia 2004;52:5863.
[88] Van Swygenhoven H, Weertman JR. Deformation in nanocrystalline metals. Materials Today 2006;9:24.
[89] Spearot DE, Jacob KI, McDowell DL. Nucleation of dislocations from [001] bicrystal interfaces in aluminum. Acta Materialia 2005;53:3579.
[90] Tschopp MA, McDowell DL. Dislocation nucleation in Σ3 asymmetric tilt grain boundaries. International Journal of Plasticity 2008;24:191.
[91] Spearot DE, Jacob KI, McDowell DL. Dislocation nucleation from bicrystal interfaces with dissociated structure. International Journal of Plasticity 2007;23:143.
[92] Capolungo L, Spearot DE, Cherkaoui M, McDowell DL, Qu J, Jacob KI. Dislocation nucleation from bicrystal interfaces and grain boundary ledges: relationship to nanocrystalline deformation. Journal of the Mechanics and Physics of Solids 2007;55:2300.
[93] De Koning M, Miller R, Bulatov VV, Abraham F. Modeling the effects of dislocation-grain boundary interactions in polycrystal plasticity: Identification and characterization of unit mechanisms. vol. 677. San Francisco, CA, United states: Materials Research Society, 2001. p.AA1.5.1.
[94] De Koning M, Miller R, Bulatov VV, Abraham FF. Modelling grain-boundary resistance in intergranular dislocation slip transmission. Philosophical Magazine A (Physics of Condensed Matter: Structure, Defects and Mechanical Properties) 2002;82:2511.
[95] De Koning M, Kurtz RJ, Bulatov VV, Henager CH, Hoagland RG, Cai W, Nomura M. Modeling of dislocation-grain boundary interactions in FCC metals. vol. 323. Les Diableret, Switzerland: Elsevier, 2003. p.281.
[96] Dewald MP, Curtin WA. Multiscale modelling of dislocation/grain-boundary interactions: I. Edge dislocations impinging on Σ11 (1 1 3) tilt boundary in Al. Modelling and Simulation in Materials Science and Engineering 2007;15:193.
[97] Dewald MP, Curtin WA. Multiscale modelling of dislocation/grain boundary interactions. II. Screw dislocations impinging on tilt boundaries in Al. Philosophical Magazine 2007;87:4615.

[98] Jin ZH, Gumbsch P, Ma E, Albe K, Lu K, Hahn H, Gleiter H. The interaction mechanism of screw dislocations with coherent twin boundaries in different face-centred cubic metals. Scripta Materialia 2006;54:1163.
[99] Jin ZH, Gumbsch P, Albe K, Ma E, Lu K, Gleiter H, Hahn H. Interactions between non-screw lattice dislocations and coherent twin boundaries in face-centered cubic metals. Acta Materialia 2008;56:1126.
[100] Cheng Y, Mrovec M, Gumbsch P. Crack nucleation at the Σ9(22-1) symmetrical tilt grain boundary in tungsten. Materials Science & Engineering: A, Structural Materials: Properties, Microstructure and Processing 2008;483-484:329.
[101] Cheng Y, Mrovec M, Gumbsch P. Atomistic simulations of interactions between the 1/2(111) edge dislocation and symmetric tilt grain boundaries in tungsten. Philosophical Magazine 2008;88:547.
[102] Rao SI, Hazzledine PM. Atomistic simulations of dislocation-interface interactions in the Cu-Ni multilayer system. Philosophical Magazine A (Physics of Condensed Matter: Structure, Defects and Mechanical Properties) 2000;80:2011.
[103] Hoagland RG, Mitchell TE, Hirth JP, Kung H. On the strengthening effects of interfaces in multilayer fcc metallic composites. Philosophical Magazine A (Physics of Condensed Matter: Structure, Defects and Mechanical Properties) 2002;82:643.
[104] Hoagland RG, Kurtz RJ, Henager CH, Jr. Slip resistance of interfaces and the strength of metallic multilayer composites. Scripta Materialia 2004;50:775.
[105] Wang J, Hoagland RG, Hirth JP, Misra A. Atomistic simulations of the shear strength and sliding mechanisms of copper-niobium interfaces. Acta Materialia 2008;56:3109.
[106] Wang J, Hoagland RG, Hirth JP, Misra A. Atomistic modeling of the interaction of glide dislocations with "weak" interfaces. Acta Materialia 2008;56:5685.
[107] Deng C, Sansoz F. Uniaxial compression behavior of bulk nano-twinned gold from molecular dynamics simulation. vol. 1049. Boston, MA, United states: Materials Research Society, 2008. p.141.
[108] Afanasyev KA, Sansoz F. Strengthening in gold nanopillars with nanoscale twins. Nano Letters 2007;7:2056.
[109] Van Swygenhoven H, Spaczer M, Caro A. Role of low and high angle grain boundaries in the deformation mechanism of nanophase Ni: a molecular dynamics simulation study. Acta Materialia 1998;10:819.
[110] Rice JR, Thomson R. Ductile versus brittle behaviour of crystals. Philosophical Magazine 1974;29:73.
[111] Cheung KS, Argon AS, Yip S. Activation analysis of dislocation nucleation from crack tip in α-Fe. Journal of Applied Physics 1991;69:2088.
[112] Rice JR, Beltz GE. The activation energy for dislocation nucleation at a crack. Journal of the Mechanics and Physics of Solids 1994;42:333.
[113] Warner DH, Curtin WA. Origins and implications of temperature-dependent activation energy barriers for dislocation nucleation in face-centered cubic metals. Acta Materialia 2009;57:4267.
[114] Zhu T, Li J, Yip S. Atomistic study of dislocation loop emission from a crack tip. Physical Review Letters 2004;93:025503.
[115] Zhang S, Zhu T, Belytschko T. Atomistic and multiscale analyses of brittle fracture in crystal lattices. Physical Review B (Condensed Matter and Materials Physics) 2007;76:1.

[116] Zhu T, Li J, Samanta A, Kim HG, Suresh S. Interfacial plasticity governs strain rate sensitivity and ductility in nanostructured metals. Proceedings of the National Academy of Sciences 2007;104:3031.
[117] Zhu T, Li J, Samanta A, Leach A, Gall K. Temperature and strain-rate dependence of surface dislocation nucleation. Physical Review Letters 2008;100:025502.
[118] Chen Z, Jin Z, Gao H. Repulsive force between screw dislocation and coherent twin boundary in aluminum and copper. Physical Review B (Condensed Matter and Materials Physics) 2007;75:212104.
[119] Weidner A, Beyer R, Blochwitz C, Holste C, Schwab A, Tirschler W. Slip activity of persistent slip bands in polycrystalline nickel. Materials Science & Engineering A (Structural Materials: Properties, Microstructure and Processing) 2006;435-436:540.
[120] Buque C, Bretschneider J, Schwab A, Holste C. Effect of grain size and deformation temperature on the dislocation structure in cyclically deformed polycrystalline nickel. Materials Science & Engineering A (Structural Materials: Properties, Microstructure and Processing) 2001;A319-321:631.
[121] Keller R, Zielinski W, Gerberich WW. On the onset of low-energy dislocation substructures in fatigue: grain size effects. Materials Science and Engineering A: Structural Materials: Properties, Microstructure and Processing 1989;A113:267.
[122] Polak J. The effect of intermediate annealing on the electrical resistivity and shear stress of fatigued copper. Scripta Metallurgica 1970;4:761.
[123] Polak J. On the role of point defects in fatigue crack initiation. Materials Science and Engineering 1987;92:71.
[124] Polak J. Resistivity of fatigued copper single crystals. Material Science and Engineering 1987;89:35.
[125] Basinski ZS, Basinski SJ. Fundamental aspects of low amplitude cyclic deformation in face-centred cubic crystals. Progress in Materials Science 1992;36:89.
[126] Ewing JA, Humfrey JCW. The Fracture of Metals under Repeated Alternations of Stress. Philosophical Transactions of the Royal Society of London. Series A, Containing Papers of a Mathematical or Physical Character 1903;200:241.
[127] Seeger A, Diehl J, Mader S, Rebstock H. Work-hardening and Work-softening of face-centred cubic metal crystals. Philosophical Magazine 1957;2:323.
[128] Friedel J. A discussion on work-hardening and fatigue in metals. Proceedings of the Royal Society of London, Series A (Mathematical and Physical Sciences) 1957;242:145.
[129] Basinski ZS, Korbel AS, Basinski SJ. The temperature dependence of the saturation stress and dislocation substructure in fatigued copper single crystals. Acta Metallurgica 1980;28:191.
[130] Coffin LF, Jr. Fatigue. Annual review of materials science. Vol. 2. Palo Alto, CA, USA: Annual Review Inc, 1972. p.313.
[131] Christ HJ. Cyclic stress-strain response and microstructure. ASM handbook: fatigue and fracture, vol. 19. 1996. p.73.
[132] Grosskreutz JC. The mechanism of metal fatigue. I. Physica Status Solidi B 1971;47:11.
[133] Grosskreutz JC. The mechanisms of metal fatigue. II. Physica Status Solidi B 1971;47:359.
[134] Basinski ZS, Basinski SJ. Formation and growth of subcritical fatigue cracks. Scripta Metallurgica 1984;18:851.

[135] Ma B-T, Laird C. Overview of fatigue behavior in copper single crystals. I. Surface morphology and stage I crack initiation sites for tests at constant strain amplitude. Acta Metallurgica 1989;37:325.
[136] Ma B-T, Laird C. Overview of fatigue behavior in copper single crystals. II. Population, size distribution and growth kinetics of stage I cracks for tests at constant strain amplitude. Acta Metallurgica 1989;37:337.
[137] Ma B-T, Laird C. Overview of fatigue behavior in copper single crystals. III Interpretation of crack growth kinetics and a new approach to predict fatigue life based on crack population density in specimens cycled at constant strain amplitude. Acta Metallurgica 1989;37:349.
[138] Ma B-T, Laird C. Overview of fatigue behavior in copper single crystals. IV. Strain and load interaction effects for tests under variable amplitude. Acta Metallurgica 1989;37:357.
[139] Ma B-T, Laird C. Overview of fatigue behavior in copper single crystals. V. Short crack growth behavior and a new approach to summing cumulative damage and predicting fatigue life under variable amplitudes. Acta Metallurgica 1989;37:369.
[140] Brown L. Dislocation and the fatigue strength of metals. In: Ashby M, Bullough R, Hartley C, Hirth J, editors. Dislocation Modelling of Physcial Systems: Proceedings of the Acta-Scripta Metallurgica Conference: Pergamon Press, 1980. p.51.
[141] Essmann U, Mughrabi H. Annihilation of dislocations during tensile and cyclic deformation and limits of dislocation densities. Philosophical Magazine A (Physics of Condensed Matter, Defects and Mechanical Properties) 1979;40:731.
[142] Mughrabi H. The cyclic hardening and saturation behaviour of copper single crystals. Material Science and Engineering 1978;33:207.
[143] Mughrabi H. Dislocation wall and cell structures and long-range internal stresses in deformed metal crystals. Acta Metallurgica 1983;31:1367.
[144] Laird C, Charsley P, Mughrabi H. Low energy dislocation structures produced by cyclic deformation. Material Science and Engineering 1986;81:433.
[145] Mughrabi H. Dislocation clustering and long-range internal stresses in monotonically and cyclically deformed metal crystals. Revue de Physique Appliquee 1988;23:367.
[146] Holzwarth U, Essmann U. The evolution of persistent slip bands in copper single crystals. Applied Physics A (Solids and Surfaces) 1993;A57:131.
[147] Mughrabi H. Cyclic slip irreversibilities and the evolution of fatigue damage. Metallurgical and Materials Transactions A: Physical Metallurgy and Materials Science 2009;40:1257.
[148] Essmann U, Gosele U, Mughrabi H. A model of extrusions and intrusions in fatigued metals. I. Point-defect production and the growth of extrusions. Philosophical Magazine A (Physics of Condensed Matter, Defects and Mechanical Properties) 1981;44:405.
[149] Differt K, Essmann U, Mughrabi H. A model of extrusions and intrusions in fatigued metals. II. Surface roughening by random irreversible slip. Philosophical Magazine A (Physics of Condensed Matter, Defects and Mechanical Properties) 1986;54:237.
[150] Essmann U, Differt K. The nature of the wall structure in persistent slip bands of fatigued metals. Scripta Metallurgica 1988;22:1337.
[151] Mughrabi H, Wang R, Differt K, Essmann U. Fatigue crack initiation by cyclic slip irreversibilities in high-cycle fatigue. Dearborn, MI, USA: ASTM, 1983. p.5.

[152] Schiller C, Walgraef D. Numerical simulation of persistent slip band formation. Acta Metallurgica 1988;36:563.
[153] Gregor V, Kratochvil J, Saxlova M. Model of PSB formation. Materials Science and Engineering A 1997;A234-23:209.
[154] Repetto EA, Ortiz M. Micromechanical model of cyclic deformation and fatigue-crack nucleation in f.c.c. single crystals. Acta Materialia 1997;45:2577.
[155] Kuhlmann-Wilsdorf D, Laird C. Dislocation behavior in fatigue. Materials Science and Engineering 1977;27:137.
[156] Kuhlmann-Wilsdorf D. Theory of plastic deformation: properties of low energy dislocation structures. Materials Science and Engineering A 1989;A113:1.
[157] Neumann P. Low energy dislocation configurations: a possible key to the understanding of fatigue. Material Science and Engineering 1986;81:465.
[158] Neumann P. Dislocation dynamics in fatigue. Physica Scripta Volume T 1987;T19B:537.
[159] Depres C, Robertson CF, Fivel MC. Crack initiation in fatigue: experiments and three-dimensional dislocation simulations. Materials Science and Engineering A (Structural Materials: Properties, Microstructure and Processing) 2004;387-389:288.
[160] Shin CS, Fivel MC, Verdier M, Robertson C. Dislocation dynamics simulations of fatigue of precipitation-hardened materials. Materials Science & Engineering A (Structural Materials: Properties, Microstructure and Processing) 2005;400-401:166.
[161] Depres C, Fivel M, Tabourot L. A dislocation-based model for low-amplitude fatigue behaviour of face-centred cubic single crystals. Scripta Materialia 2008;58:1086.
[162] Brown LM. Dislocation plasticity in persistent slip bands. Materials Science and Engineering A 2000;285:35.
[163] Brown LM. A dipole model for the cross-slip of screw dislocations in fcc metals. Philosophical Magazine A (Physics of Condensed Matter: Structure, Defects and Mechanical Properties) 2002;82:1691.
[164] van der Giessen E, Needleman A. Discrete dislocation plasticity: A simple planar model. Modelling and Simulation in Materials Science and Engineering 1995;3:689.
[165] Brinckmann S. On the role of dislocations on fatigue crack initiation. Zernike Institute for Advanced Materials, vol. PhD Thesis: University of Groningen, Netherlands, 2005.
[166] Winter AT, Pedersen OR, Rasmussen KV. Dislocation microstructures in fatigued copper polycrystals. Acta Metallurgica 1981;29:735.
[167] Buque C. Persistent slip bands in cyclically deformed nickel polycrystals. International Journal of Fatigue 2001;23:459.
[168] Buque C, Bretschneider J, Schwab A, Holste C. Dislocation structures in cyclically deformed nickel polycrystals. Materials Science and Engineering A 2001;300:254.
[169] Dorr G, Blochwitz C. Microcracks in fatigued FCC polycrystals by interaction between persistent slip bands and grain boundaries. Crystal Research and Technology 1987;22:113.
[170] Blochwitz C, Brechbuehl J, Tirschler W. Analysis of activated slip systems in fatigued nickel polycrystals using the EBSD-technique in the scanning electron microscope. Materials Science & Engineering A (Structural Materials: Properties, Microstructure and Processing) 1996;A210:42.
[171] Blochwitz C, Brechbuhl J, Tirschler W. Misorientation measurements near grain boundary cracks after fatigue tests. Strength of Materials 1995;27:3.

[172] Blochwitz C, Tirschler W. Twin boundaries as crack nucleation sites. Crystal Research and Technology 2005;40:32.
[173] Zhang ZF, Wang ZG, Li SX. Fatigue cracking possibility along grain boundaries and persistent slip bands in copper bicrystals. Fatigue & Fracture of Engineering Materials & Structures 1998;21:1307.
[174] Zhang ZF, Wang ZG, Su HH. Observations on persistent slip bands transferring through a grain boundary in a copper bicrystal by the electron channelling contrast in scanning electron microscopy technique. Philosophical Magazine Letters 1999;79:233.
[175] Zhang ZF, Wang ZG. Interactions of persistent slip bands with a grain boundary on the common primary slip plane in a copper bicrystal. Philosophical Magazine Letters 2000;80:149.
[176] Zhang ZF, Wang ZG. Comparison of fatigue cracking possibility along large- and low-angle grain boundaries. Materials Science & Engineering A (Structural Materials: Properties, Microstructure and Processing) 2000;A284:285.
[177] Zhang ZF, Wang ZG, Eckert J. What types of grain boundaries can be passed through by persistent slip bands? Journal of Materials Research 2003;18:1031.
[178] Zhang ZF, Wang ZG. Dependence of intergranular fatigue cracking on the interactions of persistent slip bands with grain boundaries. Acta Materialia 2003;51:347.
[179] Figueroa JC, Laird C. Crack initiation mechanisms in copper polycrystals cycled under constant strain amplitudes and in step tests. Material Science and Engineering 1983;60:45.
[180] Lin TH, Ito YM. Mechanics of a fatigue crack nucleation mechanism. Journal of the Mechanics and Physics of Solids 1969;17:511.
[181] Tanaka K, Mura T. A dislocation model for fatigue crack initiation. Journal of Applied Mechanics 1981;48:97.
[182] Lin MR, Fine ME, Mura T. Fatigue crack initiation on slip bands: theory and experiment. Acta Metallurgica 1986;34:619.
[183] Tanaka K, Mura T. Micromechanical theory of fatigue crack initiation from notches. Mechanics of Materials 1982;1:63.
[184] Mura T, Nakasone Y. A theory of fatigue crack initiation in solids. Transactions of the ASME. Journal of Applied Mechanics 1990;57:1.
[185] Venkataraman G, Chung YW, Nakasone Y, Mura T. Free energy formulation of fatigue crack initiation along persistent slip bands: calculation of S-N curves and crack depths. Acta Metallurgica et Materialia 1990;38:31.
[186] Mura T. Theory of fatigue crack initiation. Materials Science and Engineering A 1994;A176:61.
[187] Kruml T, Polak J, Obrtlik K, Degallaix S. Dislocation structures in the bands of localised cyclic plastic strain in austenitic 316L and austenitic-ferritic duplex stainless steels. Acta Materialia 1997;45:5145.
[188] Petersmeier T, Martin U, Eifler D, Oettel H. Cyclic fatigue loading and characterization of dislocation evolution in the ferritic steel X22CrMoV121. International Journal of Fatigue 1998;20:251.
[189] Chieragatti R, Remy L. The low cycle fatigue behaviour of MAR-M200 single crystals at 650C. Amsterdam, Netherlands: Elsevier, 1988. p.133.
[190] Stoltz RE, Pineau AG. Dislocation-precipitate interaction and cyclic stress-strain behavior of a ' strengthened superalloy. Material Science and Engineering 1978;34:275.

[191] Fritzemeier LG, Tien JK. The cyclic stress-strain behavior of nickel-base superalloys. I. Polycrystals. Acta Metallurgica 1988;36:275.
[192] Clavel M, Pineau A. Intergranular fracture associated with heterogeneous deformation modes during low cycle fatigue in a Ni-base superalloy. Scripta Metallurgica 1982;16:361.
[193] Alexandre F, Deyber S, Pineau A. Modelling the optimum grain size on the low cycle fatigue life of a Ni based superalloy in the presence of two possible crack initiation sites. Scripta Materialia 2004;50:25.
[194] Petrenec M, Obrtlik K, Polak J. Inhomogeneous dislocation structure in fatigued Inconel 713 LC superalloy at room and elevated temperatures. Materials Science and Engineering A 2005;400-401:485.
[195] Petrenec M, Obrtlik K, Polak J, Man J. Effect of temperature on the low cycle fatigue of cast Inconel 792-5A. Key Engineering Materials 2007:383.
[196] Petrenec M, Obrtlik K, Polak J, Man J. Dislocation structures in nickel based superalloy inconel 792-5A fatigued at room temperature and 700C. Materials Science Forum 2008;567-568:429.
[197] Cretegny L, Saxena A. AFM characterization of the evolution of surface deformation during fatigue in polycrystalline copper. Acta Materialia 2001;49:3755.
[198] Polak J, Man J, Obrtlik K. AFM evidence of surface relief formation and models of fatigue crack nucleation. vol. 25. Hyannis, MA, United states: Elsevier Ltd, 2003. p.1027.
[199] Polak J. Mechanisms and kinetics of the early fatigue damage in crystalline materials. Materials Science and Engineering A 2007;468-470:33.
[200] Shyam A, Milligan WW. Effects of deformation behavior on fatigue fracture surface morphology in a nickel-base superalloy. Acta Materialia 2004;52:1503.
[201] Shyam A, Milligan WW. A model for slip irreversibility, and its effect on the fatigue crack propagation threshold in a nickel-base superalloy. Acta Materialia 2005;53:835.
[202] Risbet M, Feaugas X, Guillemer-Neel C, Clavel M. Use of atomic force microscopy to quantify slip irreversibility in a nickel-base superalloy. Scripta Materialia 2003;49:533.
[203] Risbet M, Feaugas X. Some comments about fatigue crack initiation in relation to cyclic slip irreversibility. Engineering Fracture Mechanics 2008;75:3511.
[204] Risbet M, Feaugas X, Guillemer-Neel C, Clavel M. Damage in nickel base superalloy: Influence of local parameters measured by electron backscattered diffraction and atomic force microscopy. Scripta Materialia 2009;60:269.
[205] Huang EW, Barabash RI, Yandong W, Bj C, Li L, Liaw PK, Ice GE, Yang R, Hahn C, Pike LM, Klarstrom DL. Plastic behavior of a nickel-based alloy under monotonic-tension and low-cycle-fatigue loading. International Journal of Plasticity 2008;24:1440.
[206] Li P, Zhang ZF, Li SX, Wang ZG. Comparison of dislocation patterns in cyclically deformed fcc metals. Scripta Materialia 2008;59:730.
[207] Miao J, Pollock TM, Wayne Jones J. Crystallographic fatigue crack initiation in nickel-based superalloy Rene 88DT at elevated temperature. Acta Materialia 2009;57:5964.
[208] Kobayashi S, Kamata A, Watanabe T. Roles of grain boundary microstructure in high-cycle fatigue of electrodeposited nanocrystalline Ni-P alloy. Scripta Materialia 2009;61:1032.
[209] Zhang ZF, Wang ZG. Relationship between the fatigue cracking probability and the grain-boundary category. Philosophical Magazine Letters 2000;80:483.

[210] Wang ZG, Zhang ZF, Li XW, Jia WP, Li SX. Orientation dependence of the cyclic deformation behavior and the role of grain boundaries in fatigue damage in copper crystals. Materials Science and Engineering A 2001;319-321:63.
[211] Kobayashi S, Inomata T, Kobayashi H, Tsurekawa S, Watanabe T. Effects of grain boundary- and triple junction-character on intergranular fatigue crack nucleation in polycrystalline aluminum. Journal of Materials Science 2008;43:3792.
[212] Christ HJ. On the orientation of cyclic-slip-induced intergranular fatigue cracks in face-centred cubic metals. Materials Science and Engineering A 1989;A117:L25.
[213] Liu W, Bayerlein M, Mughrabi H, Day A, Quested PN. Crystallographic features of intergranular crack initiation in fatigued copper polycrystals. Acta Metallurgica et Materialia 1992;40:1763.
[214] Eshelby JD, Frank FC, Nabarro FRN. The equilibrium of linear arrays of dislocations. Philosophical Magazine 1951;42:351.
[215] Stroh AN. A theory of the fracture of metals. Advances in Physics 1957;6:418.
[216] Burmeister HJ, Richter R. Investigations on the origin of grain boundary cracks in fatigued f.c.c. metals. Acta Materialia 1997;45:709.
[217] Lin TH, Wong KKF, Teng NJ, Lin SR. Micromechanic analysis of fatigue band crossing grain boundary. Materials Science and Engineering A 1998;A246:169.
[218] Hashimoto S, Ikehata H, Kato A, Kato H, Kaneko Y. Fatigue crack nucleation at Σ3(112) boundary in a ferritic stainless steel. Interface Science 1999;7:159.
[219] Llanes L, Laird C. The role of annealing twin boundaries in the cyclic deformation of f.c.c. materials. Materials Science & Engineering A (Structural Materials: Properties, Microstructure and Processing) 1992;A157:21.
[220] Boettner RC, McEvily JAJ, Liu YC. On formation of fatigue cracks at twin boundaries. Philosophical Magazine 1964;10:95.
[221] Thompson AW. The influence of grain and twin boundaries in fatigue cracking. Acta Metallurgica 1972;20:1085.
[222] Qu S, Zhang P, Wu SD, Zang QS, Zhang ZF. Twin boundaries: strong or weak. Scripta Materialia 2008;59:1131.
[223] Guo XL, Lu L, Li SX. Dislocation evolution in twins of cyclically deformed copper. Philosophical Magazine Letters 2005;85:613.
[224] Kim WH, Laird C. Crack nucleation and stage I propagation in high strain fatigue. II. Mechanism. Acta Metallurgica 1978;26:789.
[225] Lim LC, Raj R. Continuity as slip screw and mixed crystal dislocations across bicrystals of nickel at 573K. Acta Metallurgica 1985;33:1577.
[226] Heinz A, Neumann P. Crack initiation during high cycle fatigue of an austenitic steel. Acta metallurgica et materialia 1990;38:1933.
[227] Peralta P, Llanes L, Bassani J, Laird C. Deformation from twin-boundary stresses and the role of texture: application to fatigue. Philosophical Magazine A (Physics of Condensed Matter, Defects and Mechanical Properties) 1994;70:219.
[228] Sumigawa T, Kitamura T. Nucleation of slip bands near twin boundary in high-cycle fatigue. JSME International Journal, Series A (Solid Mechanics and Material Engineering) 2004;47:98.
[229] Lewis AC, Jordan KA, Geltmacher AB. Determination of critical microstructural features in an austenitic stainless steel using image-based finite element modeling. Metallurgical

and Materials Transactions A: Physical Metallurgy and Materials Science 2008;39 A:1109.
[230] Blochwitz C, Tirschler W. Influence of texture on twin boundary cracks in fatigued austenitic stainless steel. Materials Science and Engineering A 2003;339:318.
[231] Pineau A. The randomness of fatigue and fracture behavior in metallic materials and mechanical structures. In: Ostoja-Starzewski M, editor. Mechanics of Random and Multiscale Microstructures, vol. 430. CISM, 2001. p.163.
[232] Suresh S. Fatigue of Materials: Cambridge Press, 1998.
[233] Socie DF. Probablistic Aspects of Fatigue - Variability. Fracture Control Program. Urbana, IL, 2005.
[234] Ghonem H, Provan JW. Micromechanis theory of fatigue crack initiation and propagation. Engineering Fracture Mechanics 1980;13:963.
[235] Grison J, Remy L. Fatigue failure probability in a powder metallurgy Ni-base superalloy. Engineering Fracture Mechanics 1997;57:41.
[236] Todinov MT. Probabilistic method for predicting fatigue life controlled by defects. Materials Science and Engineering A 1998;A255:117.
[237] Wirsching PH, Torng TY, Martin WS. Advanced fatigue reliability analysis. International Journal of Fatigue 1991;13:389.
[238] Jeulin D. Random structure models for homogenization and fracture statistics. In: Ostoja-Starzewski M, editor. Mechanics of Random and Multiscale Microstructures, vol. 430. CISM, 2001. p.33.
[239] Ellyin F. Stochastic modelling of crack growth based on damage accumulation. Theoretical and Applied Fracture Mechanics 1986;6:95.
[240] Kulkarni SS, Sun L, Moran B, Krishnaswamy S, Achenbach JD. A probabilistic method to predict fatigue crack initiation. International Journal of Fracture 2006;137:9.
[241] Kitamura T, Ghosn LJ, Ohtani R. Stochastic Modeling of Crack Initiation and Short-Crack Growth under Creep and Creep-Fatigue Conditions. United States, 1989. p.20p.
[242] Qiao Y, Chakravarthula SS. Effects of randomness of grain boundary resistance on fatigue initiation life. International Journal of Fatigue 2005;27:1251.
[243] Kato M, Mori T. Statistical consideration of fatigue damage accumulation. Mechanics of Materials 1992;13:155.
[244] Przybyla CP, McDowell DL. Microstructure-sensitive extreme value probabilities for high cycle fatigue of Ni-base superalloy IN100. International Journal of Plasticity 2010;26:372.
[245] Otwinowski Z, Minor W. Processing of X-ray Diffraction Data Collected in Oscillation Mode. In: Carter CW, Sweet RM, editors. Macromolecular Crystallography, vol. 276: Academic Press (New York), 1997. p.307.
[246] Hosford WF. Mechanical behavior of materials: Cambridge University Press, 2005.
[247] Mulders JJL, Gholinia A. Three-dimensional crystallographic analysis beyond EBSD mapping: the next dimension. http://www.fei.com/uploadedFiles/Documents/Content/2006_06, 2006.
[248] Ren W, Nicholas T. Effects and mechanisms of low cycle fatigue and plastic deformation on subsequent high cycle fatigue limit in nickel-base superalloy Udimet 720. Materials Science and Engineering A 2002;332:236.

[249] Joyce MR, Reed PAS. Fatigue crack growth behaviour under mixed mode loading in Udimet 720 SX. Champion, PA, United states: Minerals, Metals and Materials Society, 2004. p.295.
[250] Pang HT, Reed PAS. Effects of microstructure on room temperature fatigue crack initiation and short crack propagation in Udimet 720Li Ni-base superalloy. International Journal of Fatigue 2008;30:2009.
[251] Plimpton S. Fast parallel algorithms for short-range molecular dynamics. Journal of Computational Physics 1995;117:1.
[252] Plimpton S. Large-scale atomic/molecular massively parallel simulator. http://lammps.sandia.gov/: Sandia National Laboratories, 2007.
[253] Foiles SM, Hoyt JJ. Computation of grain boundary stiffness and mobility from boundary fluctuations. Acta Materialia 2006;54:3351.
[254] Siegel DJ. Generalized stacking fault energies, ductilities, and twinnabilities of Ni and selected Ni alloys. Applied Physics Letters 2005;87:121901.
[255] Rice JR. Dislocation nucleation from a crack tip: an analysis based on the Peierls concept. Journal of the Mechanics and Physics of Solids 1992;40:239.
[256] Kelchner CL, Plimpton SJ, Hamilton JC. Dislocation nucleation and defect structure during surface indentation. Physical Review B (Condensed Matter) 1998;58:11085.
[257] Humphrey W, Dalke A, Schulten K. VMD: Visual Molecular Dynamics. Journal of Molecular Graphics 1996;14:33.
[258] Karthaler HP. The study of glide on {001} planes in f.c.c. metals deformed at room temperature. Philosophical Magazine A 1978;38:141.
[259] Korner A, Karthaler HP. Glide dislocations on cube planes in a low stacking-fault energy alloy. Physica Status Solidi 1983;75:525.
[260] Ezaz T, Sangid MD, Sehitoglu H. Energy Barriers Associated with Slip-Twin Interactions. Submitted to Philosophical Magazine A 2010.
[261] Griffith AA. The phenomena of rupture and flow in solids. Royal Society of London -- Philosophical Transactions 1920;221:163.
[262] Cooper RE. The equilibrium shape of deformation twins. Acta Metallurgica 1965;13:46.
[263] Cooper RE. The equilibrium shape of deformation twins. II. Acta Metallurgica 1966;14:78.
[264] Argon AS. Strengthening mechanisms in crystal plasticity: Oxford University Press, 2008.
[265] Sun Y, Rice JR, Truskinovsky L. Dislocation nucleation versus cleavage in Ni_3Al and Ni. Pittsburgh, PA, USA: Mater. Res. Soc, 1991. p.243.
[266] Mishin Y. Atomistic modeling of the and '-phases of the Ni-Al system. Acta Materialia 2004;52:1451.
[267] H. Mughrabi, Wang R. Cyclic deformation of face-centered cubic polycrystals: a comparison with observations on single crystals. In: N. Hansen, A. Horsewell, T. Leffers, Lilholt H, editors. Deformation of Polycrystals: Mechanisms and Microstructure, Proceedings, Second Riso International Symposium on Metallurgy and Materials Science. Riso National Laboratory, Roskilde, Denmark, Sept, 1981. p.87.
[268] Tschopp MA, McDowell DL. Influence of single crystal orientation on homogeneous dislocation nucleation under uniaxial loading. Journal of the Mechanics and Physics of Solids 2008;56:1806.

[269] Barbe F, Forest S, Cailletaud G. Intergranular and intragranular behavior of polycrystalline aggregates. 2. Results. International Journal of Plasticity 2001;17:537.
[270] Schroeter BM, McDowell DL. Measurement of deformation fields in polycrystalline OFHC copper. International Journal of Plasticity 2003;19:1355.
[271] Zhang N, Tong W. An experimental study on grain deformation and interactions in an Al-0.5%Mg multicrystal. International Journal of Plasticity 2004;20:523.
[272] Crepin J, Heripre E, Dexet M, Gelebart L, Roos A, Bornert M, Caldemaison D. Coupling between experimental measurements and polycrystal finite element calculations for micromechanical study of metallic materials. International Journal of Plasticity 2007;23:1512.
[273] Efstathiou C, Sehitoglu H, Lambros J. Multiscale strain measurements of plastically deforming polycrystalline titanium: Role of deformation heterogeneities. International Journal of Plasticity 2010;26:93.
[274] Zhao Z, Ramesh M, Raabe D, Cuitino AM, Radovitzky R. Investigation of three-dimensional aspects of grain-scale plastic surface deformation of an aluminum oligocrystal. International Journal of Plasticity 2008;24:2278.